Fermilab

FERMILAB-THESIS-2003-07

Determination of the Top Quark Mass using Neural Networks

THESIS

Submitted to the Panjab University, Chandigarh for the Degree of

Doctor of Philosophy

in the Faculty of Science

By

Rajwant Kaur

Centre of Advanced Study in Physics

Panjab University

Chandigarh

August, 2002

Dedicated to my father

Late S. Jagdish Singh Ji

Acknowledgements

With all my love, respect and affections, I thank my thesis supervisors Prof. Suman Beri and Prof. J. M. Kohli for their support, encouragement and efforts which led my research work to presentable form. Prof. Suman's time to time guidance has been of great importance for my work. Apart from the professional guidance, her attitude towards me has been very comforting and beneficial. Working with a soft spoken person like Prof. Kohli has been a pleasant and learning experience. I thank Chairman, Department of Physics, for providing adequate facilities to work in the department.

My very next sincere thanks go to our collaborator Prof. Harrison B. Prosper from whom I learned many fundamental techniques regarding physics analyses. Despite being very busy, he was always ready to offer me help and give useful suggestions.

I thank Dr. Vipin Bhatnagar for the useful discussions regarding the basic concepts of $e\mu$ channel. I thank engineers of our section Mr. V. K. Bhandari and Mr. Baljinder Singh for helping me in understanding the hardware related to my research. Mr. Bhandari's guidance and helping hand brought the hardware section (Chapter 5) of this thesis in the presentable form. Many thanks are due to Mr. Sanjeev Gautam for always helping me in both computer hardware and software aspects. I would also like to thank Dr. J. B. Singh and Dr. Keya Dharamvir for their timely help. I thank Mr. Harpreet Singh for providing me with DØ Run I data.

I thank all the members of DØ Collaboration with special thanks to Dr. Pushpa Bhat. My thanks to Prof. Shuichi Kunori for the useful discussions.

Friends are those whom you long for not only when you are in need but also when everything is perfect. When I think about my friends during this journey, the very first name that strikes in my mind is of Monica Randhawa. I also thank Jagdeep Kaur and Harleen Dahiya for being wonderful friends. Thanks are due to Gopika Sood for being helping and considerate.

I thank all the members in DØ/CMS section of our department. I thank all the research scholars in various labs and all the members in teaching and non-teaching staff of our department for helping me directly or indirectly.

Today while writing this thesis, I am missing my father a lot who left us on 15.1.2001. This work would not have been possible without his support in always letting me choose my own paths. He would have been the happiest person to see me completing my work. I wish he was here.

God cannot be everywhere therefore HE made mothers. I am very fortunate to have a loving and friendly mother. I thank her for all the support and encouragement she has been giving me all through my life. Millions of thanks are due to my only brother Gurpal Singh for always being there to direct me in right direction and always wishing "the best" for me. It is the result of his blessings that I am able to

complete my work. I thank my sister, jija ji and nephew Sohail for their concern and encouragement. I would also like to thank Late Mrs. Morni Devi for always showering her blessings on me.

Lastly, I thank my fiance Harinder Kalsi for his emotional support. I enjoyed the last phase of my PhD work with him by my side. We both thank our families who made us know each other.

I would like to again thank everyone above and apologize to those I have inadvertently omitted.

The financial support by DST and CSIR, Govt. of India is duly acknowledged.

(Rajwant Kaur)

Abstract

We present the results of top quark mass study based on three "non-conventional" methods : Neural Networks method, method of four vectors and the method of invariant mass using $t\bar{t} \to W^+bW^-\bar{b} \to (e/\mu)\nu\,(e/\mu)\nu$ decay in $p\bar{p}$ collisions at $\sqrt{s} =$ 1.8 TeV. The analysis assumes Standard Model coupling and branching ratios and is based on an integrated luminosuty of 108.3 ± 5.7 pb^{-1} accumulated by DØ detector during the Fermilab Tevatron Collider Run I (1992-96). These methods would be quite useful in the determination of the top quark mass for DØ Run II where high statistics would be available. Using neural network analysis, the top quark mass obtained is $m_t = 177.9$ GeV. The systematical uncertainty in m_t comes out to be 2.17 GeV and statistical uncertainty in the measurement of m_t is about 56 - 59 GeV. In DØ Run II because of the introduction of a central magnetic field, a significant improvement in the muon momentum measurement is anticipated. Taking this fact into an account, the uncertainty reduces to $\sim$ 40 - 42 GeV. Number of top events from $e\mu$ channel are expected to be about ten times more than the number in Run I which will further reduce the present uncertainty approximately to 6.3 - 6.5 GeV. By using the method of four vectors, systematic uncertainty is 1.52 GeV and statistical uncertainty is $\sim$ 45 - 49 GeV for three $e\mu$ events which would reduce to $\sim$ 7.5 - 8.9 GeV in DØ Run II and will lead to the precision in the top quark mass. Using the method of $e\mu$ invariant mass, the expected systematic error will translate by a factor of 5.

In addition to the study of the top quark mass, we participated in the R and D work for the fabrication of the Pixel Scintillation Counters which was undertaken by our group at Chandigarh. Five prototype pixel counters were fabricated which were to be used in the forward muon detector in the muon system of DØ upgrade for Run II. The counters have been checked, tested and their performance was found to be extremely satisfactory.

Contents

List of Tables

List of Figures

Chapter 1

Introduction

1.1 What is the World Made of?

Answer to this will be very different depending on whom we ask this question. To a biologist, the world is made of living organisms. To a chemist, the world is made of molecules formed from atoms and the answer of the physicist will probably start by talking about atoms, and then proceed to talk about the protons, neutrons and electrons that make up an atom. However, for particle physicists, there is no ambiguity in this question. They want to know what are the fundamental, indivisible building blocks from which all the matter in this universe is made of? What are the basic interactions that glue these building blocks together to make the matter we see around us? We have a fairly consistent picture or model of the world at this most fundamental level that explains all of our experimental results to date regarding this question.

All the matter we see around us is made of atoms. In fact, atoms are not fundamental building blocks. Rutherford's famous experiment of scattering alpha particles from atomic targets was the first dramatic demonstration of scattering techniques in nuclear physics. He was able to show from the angular distribution of the scattered particles that atoms have small massive nuclei at their centers. Further studies established that these nuclei are made of protons and neutrons. Then electron scattering experiments at much higher energies showed that protons and neutrons themselves contain small hard constituents; *the quarks*. Higher energies opened the way to deeper understanding.

High Energy Physics (HEP), more commonly referred to as *Particle Physics*, is the study of what everything is made of. Its aim is to understand the workings of the universe at the most fundamental level *i.e.* one desires to identify those constituents of matter which may not be subdivided any further and to describe completely all of the interactions between them. The apparatus needed to reach, the time needed to design, construct and execute an experiment has also grown with time. So, too, has the number of people that must collaborate in order for such an effort to succeed. That is the reason why big collaborations are involved in the research at high energies.

Now, the question is why do we need High Energy? The very first reason is due to the wave characteristics of light. In order to see something, we shine light on it. The space resolution that can be achieved in studying the scattering of one particle from another is limited by the wavelength λ of their relative motion; $\lambda = 2\pi/k$ where k is their relative momentum. However, when we want to see something that is smaller than the wavelength of light, we will have a very tough time seeing it. Because to probe small distances requires large k which implies high energy in the center-of-mass frame of reference. Luckily, we can use other particles to see with, such as electrons. They too have wave properties, but their wavelengths decrease as their momenta increase. So, the faster a probing particle is going, the less its wavelength is, and with better resolution we can see. A second reason, we need high energy particles is because we are interested in creating new particles *i.e.* new particle production. A heavy particle of mass m can be materialized only if there is enough spare energy ($E = mc^2$) available in the center-of-mass frame and using high energy particles one achieves the goal.

1.2 Standard Model

Particle physics is the study of the fundamental constituents of matter and their interactions. However, which particles are regarded as fundamental has changed with time as physicists knowledge has improved. Modern theory - called the *Standard Model* (SM) has been extremely successful so far [1]. It attempts to explain all the phenomena of particle physics in terms of properties and interactions of a small number of particles of three distinct types. The first two are called leptons and quarks and are spin 1/2 fermion, the third is a set of spin 1 bosons called gauge bosons which act as 'force carriers' in the theory. Therefore, one can say that the SM of particle physics is a description of nature at very small distance scales, typically scales smaller than that of an atomic nucleus (10^{-15} m). In the SM, these particles are all assumed to be elementary *i.e.* they are treated as point particles, without internal structure or excited states. Both the quarks and leptons are grouped into three generations of two particles each. The corresponding particles in each generation have similar properties, except for their masses, which increase with each successive generation. All normal matter (protons, neutrons and electrons) is composed of particles from the first generation. Particles in higher generations can be produced in high energy interactions, but they are unstable and ultimately decay into first generation particles or photons.

Each generation of leptons consists of one charged particle and an associated uncharged particle. Experimentally, masses of the neutrinos are constrained to be quite small, the SM assumes that they are zero. The charged leptons interact electromagnetically, but the neutrinos are affected only by the weak interaction.

$$\text{Leptons}: \quad \begin{pmatrix} \nu_e \\ e^- \end{pmatrix} \quad \begin{pmatrix} \nu_\mu \\ \mu^- \end{pmatrix} \quad \begin{pmatrix} \nu_\tau \\ \tau^- \end{pmatrix} \tag{1.1}$$

The quarks are similarly grouped in doublets. Quarks have fractional charge *i.e.* either 1/3 or 2/3 of the charge of an electron. They are affected by the strong force which binds quarks together inside the nuclei.

$$\text{Quarks}: \quad \begin{pmatrix} u \\ d \end{pmatrix} \quad \begin{pmatrix} c \\ s \end{pmatrix} \quad \begin{pmatrix} t \\ b \end{pmatrix} \tag{1.2}$$

The physical world is governed by four fundamental forces : strong force, electromagnetic force, weak force and gravitational force.

Electromagnetic forces provide the attraction between electrons and nuclei that build atoms and molecules; they control chemistry and the physics of materials. Weak forces lie behind processes like β-decay which allows protons to transmute into neutrons and vice-versa; they are vital for the synthesis of heavy elements in the early universe and in stellar cores and for the fusion power cycles in stars. Strong forces or nuclear forces act only at very short distances; they bind quarks together to make nucleons (protons and neutrons) and bind nucleons together to make nuclei. Gravitational forces are by far the weakest and are mediated by 'graviton'; they are important for large bodies but negligible for nuclear and subnuclear particles compared to other forces. HEP is concerned with the first three of these because gravity is too much weaker than the other three and it has no influence on subatomic processes and hence can be excluded.

Force	Gauge Boson	Symbol	Charge	Spin	Mass (GeV)
Strong	gluon	g	0	1	0
Electromagnetic	photon	γ	0	1	0
Weak	W boson	W	± 1	1	80.4
	Z boson	Z	0	1	91.2

Table 1.1: Fundamental forces and gauge bosons.

The forces between matter units (leptons + quarks) are transmitted by specific fields or particles. The electromagnetic force is transmitted by photons, the strong force by massless spin 1 gluons and the weak force by massive W and Z bosons. These forces are all described by gauge theories and the transmitting particles are called gauge bosons. Charged leptons participate in both electromagnetic and weak interactions, whereas neutral leptons only interact weakly. Quarks interact via all three interactions. The weak and electromagnetic interactions of both quarks and leptons are described by the Electroweak Theory, which is the generalization of Quantum Electrodynamics (QED). QED is mediated by photon, which couples to particles which have electric charge. The strong interaction of quarks is described by Quantum Chromodynamics (QCD) and is mediated by gluons.

The weak and electromagnetic interactions are successfully unified in the electroweak theory based on the gauge group $SU(2)_L \times U(1)_Y$. In this theory, local

	Symbol	Name	Mass (MeV)	Charge (e)
Quarks	u	up	≈ 5	2/3
(spin = 1/2)	d	down	≈ 10	-1/3
	s	strange	≈ 200	-1/3
	c	charm	≈ 1500	2/3
	b	bottom	≈ 4500	-1/3
	t	top	$\approx 175 - 200$ GeV	2/3
Leptons	e	electron	0.511	-1
(spin = 1/2)	ν_e	electron neutrino	< 3 eV	0
	μ	muon	105.7	-1
	ν_μ	muon neutrino	< 0.19	0
	τ	tau	1776.9	-1
	ν_τ	tau neutrino	< 18.2	0
Gauge bosons	γ	photon	0	0
(spin = 1)	W	W	80.4 GeV	1
	Z	Z	91.2 GeV	0
	g	gluon	0	0
Higgs	H	Higgs	?	?

Table 1.2: Fundamental particles of the Standard Model.

gauge invariance is spontaneously broken by the Higgs mechanism. This causes the intermediate bosons ($W^\pm$ and Z^0) of the weak interaction to acquire masses, while leaving the photon massless. The theory of the strong interaction, QCD, is based on the exact local gauge symmetry $SU(3)$ which results in the conservation of color (the strong charge). A distinctive property of QCD is the tendency of the coupling strength to decrease at short distances, this is known as asymptotic freedom. This behavior explains why quarks behave as free particles within hadrons but can not be liberated.

The remaining ingredient of the SM is the Higgs boson. The standard method of introducing a new interaction into models like the SM requires that the associated gauge bosons be massless. This is a problem for the case of the weak force, since the $W^\pm$ and Z^0 bosons must be quite massive in order to explain the observed low energy behavior. The Higgs mechanism is a way around this problem. It introduces a new scalar particle which interacts with the W and Z in exactly the right way so that they acquire masses. The quarks and leptons can also acquire masses through this mechanism. If this description is correct, the Higgs should appear. But it has not been discovered yet.

Within the SM, the top mass, the Higgs mass and the ratio of the W and Z masses are interrelated as shown in Figure 1.1. Although the dependence on the Higgs mass is weak (logarithmic), it is apparent that a sufficiently accurate measurement of the top mass can constrain the allowable range of Higgs masses.

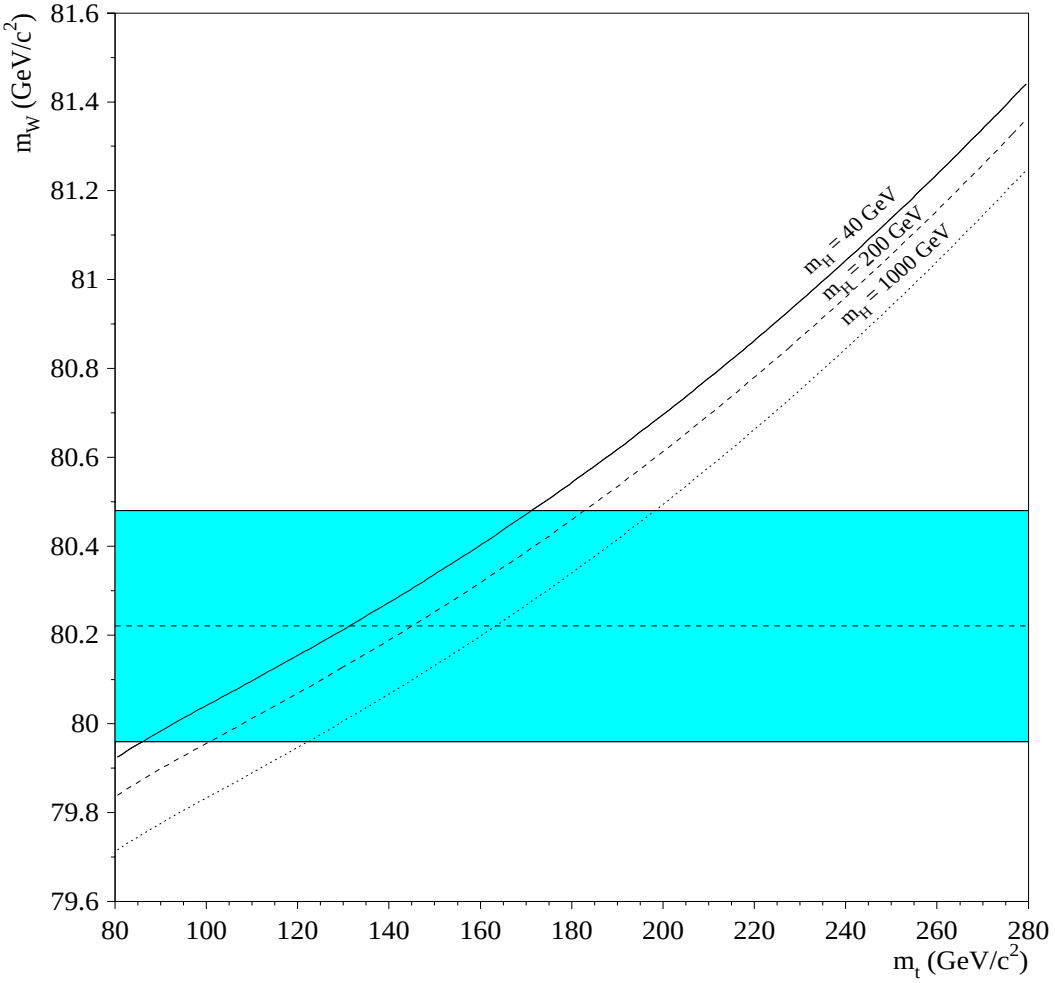

Figure 1.1: The SM relation between top mass and W mass for different values of the Higgs mass. The LEP Z mass of 91.187 GeV/c^2 is used. The shaded band indicates a W mass of $m_W = 80.22 \pm 0.26$GeV/c^2

1.2.1 Color and Color Confinement

The quark model is very successful, but without assigning a new degree of freedom to quarks this model would contradict the Pauli principle. The Pauli principle states that the wavefunctions of any quantum state must be antisymmetric under the interchange of any two identical spin 1/2 fermions. The spectrum of light baryons requires that the combined space and spin wavefunction be symmetric under the interchange of any two quarks with the same flavor, which is in conflict with the Pauli principle. This contradiction between quark model and Pauli principle can be resolved by assuming an additional degree of freedom for quarks. The wavefunction for this new attribute, which is called color, is antisymmetric, which is consistent with the Pauli principle and the space and spin wavefunction remains symmetric, which explains the spectrum of light baryons.

According to the color idea, each quark is supposed to have one of these possible colors : red, blue or green. Antiquarks are antired (cyan), antigreen (magenta) or antiblue (yellow). The cross-section for producing a quark pair of any flavor is proportional to the number of colors. Color is an additive quantum number like electric charge, whose values are opposite in sign for particles and antiparticles.

Because of color, the strong forces transmitted by gluons differ significantly from the electromagnetic forces transmitted by photons. According to the color confinement hypothesis, the allowed combinations of quarks and antiquarks are $q\bar{q}$ and qqq. Since the electric charge of the quarks is a multiple of 1/3, free hadrons can not have fractional electric charges. Color confinement is analogous to allowing only neutral atoms to exist yet forbidding ionization. The interaction between quarks is weaker at short distances so quarks can be treated as free particles and perturbative methods apply. On the other hand, at large distances the interaction strength grows making the ionization energy infinite concluding isolated quarks and gluons can not exist.

1.3 Aim of the Thesis

One of the main goals of any experiment which probes previously unexplored regimes of energy is to search for the particles too massive to have been produced at any previous experiment. Such a particle was in fact discovered at Tevatron in 1995 by the DØ and CDF collaborations and is the most massive fundamental particle yet known : *the top quark*. The aim of this thesis is to determine the mass of this particle using different "non-conventional" methods especially using Neural Networks. We have also tried to determine the top quark mass using method of four vectors and the method of $e\mu$ invariant mass.

The top quark mass is one of the most important parameter of the SM, as together with the mass of W boson (m_W) it constraints on the mass of the SM Higgs boson. Therefore, it is very important to get any improvement in the precision of the top quark mass measurements. The Higgs boson, the W boson and the top

quark contribute via radiative corrections to observables already measured at LEP and SLC so that the measured observables together with the measured values of the W and the top mass restrict the allowed mass range of the Higgs boson. Recent experimental constraints on the Higgs boson mass are consistent with the SM [2]. In the future, when the W boson mass should be measured to an accuracy of 40 MeV, a precision of about 1 GeV in the top quark mass would yield a prediction in the Higgs boson mass of $\delta m_H/m_H \leq 40\%$. We have been motivated to use different methods to determine the top quark mass which are relatively simple.

For the analysis, HEP data collected at FNAL (Fermi National Accelerator Laboratory) with DØ detector at center-of-mass energy ($\sqrt{s}$) 1.8 TeV for Run I (1992-96) has been used. In the collision, beams of protons and antiprotons are counter-rotating in a four-mile ring of magnets located at the FNAL in Batavia, Illinois. The accelerator is designed such that these collisions occur at two points, each of which is surrounded by a massive apparatus designed to measure the results of the collisions. One of these, the DØ detector, provided the data used in this analysis.

The DØ detector is upgraded to center-of-mass energy of 2.0 TeV in Run II. As a result, the Run II data would be quite large; about 100 times the Run I data. To exploit the full use of high statistics, the main task is to reduce systematic errors so that we can benefit from the reduced statistical errors. We need to explore different methods to cross-check the results and also use different methods which may yield smaller systematic errors by using as many as decay modes as possible. The present study is a step towards this goal by studying one of the channel via which top quark can decay. The decay $t\bar{t} \to bW^+\ \bar{b}W^- \to l\nu l\nu$, in the special case of $e\mu$ channel, where one of the leptons is electron (e) and the other muon (μ), has been explored for the determination of the top quark mass in our analysis. We have made a study of top quark mass using/developing three different methods namely neural networks method, method of four vectors and the method of $e\mu$ invariant mass. These methods will be useful for analyses of DØ Run II data as well as for LHC ($\sqrt{s} = 14$ TeV) where high statistics will be available.

1.4 Outline of the Thesis

The broad structure of the thesis is as follows. The current Chapter 1 gives the brief description of high energy physics and a short overview of the SM. Chapter 2 gives the brief account of top quark physics including its decay and production and how the existence of the top quark is essential for the integrity and simplicity of the SM. Chapters 3 and 4 briefly explain the accelerator and the detector respectively, used in the experiment. The Panjab University HEP group was involved in the fabrication of pixel scintillation counters for DØ upgrade. Chapter 5 deals with the fabrication of pixel scintillation counters. This chapter provides the complete description of the steps involved in the scintillators fabrication, the cosmic ray setup used to measure the efficiency of the counters and the fiber testing for the muon scintillator for the collection of light, at Panjab University and the brief account on

DØ upgrade. Chapter 6 explains DØ trigger system and the Monte Carlo simulations to model the signal and backgrounds. Chapter 7 describes how the data are processed to provide information about the particles that were produced in the collision. In Chapter 8 we discuss the efficiencies, acceptances for Monte Carlo (both signal and backgrounds). In this chapter, details of the techniques : neural networks method and method of four vectors, used in our analyses for the top quark mass determination are given. The results based on these methods and the third method (using $e\mu$ invariant mass) are presented in Chapter 9. Chapter 10 gives the conclusions of the study.

Chapter 2

Top Quark

The top quark was discovered at the Tevatron in 1995 by the DØ and CDF collaborations [3, 4]. Top quark mass is one of the most important parameter of the SM. It is the heaviest elementary particle with a mass close to the electroweak scale which suggests that the top quark may play a role in the breaking of electroweak symmetry and therefore in the origin of fermion masses [5]. Prior to the discovery of the top quark, there were good theoretical reasons for its existence. This chapter provides the outline of the top quark physics including the theoretical evidences for the top quark existence, production and decay modes.

2.1 Why the Top Quark should Exist?

2.1.1 Anomalies

The leptons in the electroweak theory were shown to possess "anomalies" (the triangle anomalies) which threatened renormalizability. An anomaly is the failure of a classical symmetry to survive the process of quantization and renormalization and this problem arises from the interaction of three gauge bosons via a closed loop of fermions. An example of the fermion loop which gives rise to chiral anomalies in the SM is shown in Figure 2.1. The contribution of the diagram for each fermion is $n_c g_a^f Q_f^2$, where f is a fermion, Q_f is the fermion charge and g_a^f is the fermion axial coupling of the weak neutral current to Z^0 and $n_c = 3$ for quarks. The renormalizability of the SM requires the cancellation of the triangle anomalies. It turns out that the fermion contributions within each generation cancel if the electric charges of all left-handed fermions sum to zero *i.e.*

$$\sum Q_f = -1 + 3 \times [(2/3) + (-1/3)] = 0 \tag{2.1}$$

The factor 3 is the number of color charges for each quark flavor. For this to work for the third generation, the top quark with $Q = 2/3$ must exist. Therefore, without the top quark the minimal SM would have anomalies.

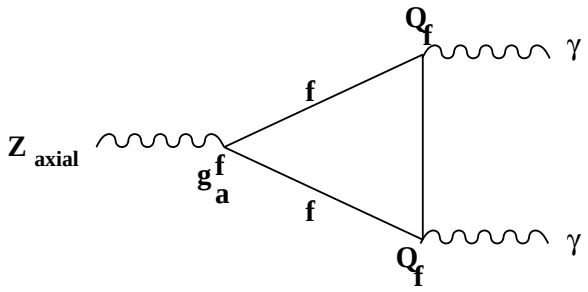

Figure 2.1: An example of the fermion diagram.

2.1.2 $B_0 - \bar{B}_0$ mixing

Weak interactions do not conserve quark flavors and therefore B_0 and $\bar{B}_0$ mesons can mix. The observed rate of this mixing is proportional to $|V_{td}|^2$ (CKM[1] matrix element for the t and d quark coupling). This implies that a massive top quark is needed in the loops so that the b quark can decay indirectly via an intermediate state containing a virtual t quark and the d quark. This indicates that the b quark has a weak isospin partner *i.e.* top quark with weak isospin $I_3 = +\frac{1}{2}$.

2.1.3 b decays ($b \to l^+l^-$)

In the SM, the b quark decays occur through quark mixing [5] and the allowed vertices are $b \to cW^+$ and $b \to uW^-$. These are proportional to the CKM matrix elements V_{cb} and V_{ub}. This means that the b has to be in a doublet, allowing the top to exist. If the b quark is assumed to be an $SU(2)$ singlet, then it will have no charged current interaction and can not decay via W emission. Since, experimentally it is known to decay then it must do so by mixing with the lighter quarks (s and d). This leads to the quantitative predictions $\mathrm{BR}(b \to l^+l^-X) > 0.013$. However, experiments have shown that $\mathrm{BR}(b \to l^+l^-X) < 0.0012$. This establishes that b is not an $SU(2)$ singlet and another particle must accompany the b quark which is the top quark (t).

2.1.4 A_{FB} in $e^+e^- \to b\bar{b}$

The production of $b\bar{b}$ pairs in e^+e^- collisions can be either mediated by a photon (γ) or a Z boson as shown in Figure 2.2. The contributions of the photon (γ) exchange to the angular distribution to the b about the plane perpendicular to the beam in the center-of-mass frame is symmetric and the contribution of the Z should be asymmetric if the b is in an $SU(2)_L$ doublet.

[1] Cabibbo-Kobayashi-Maskawa

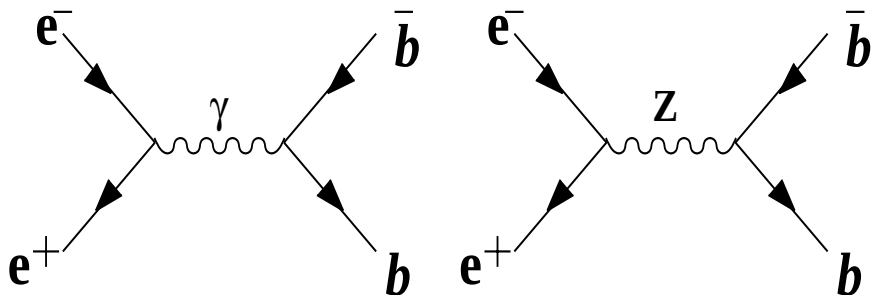

Figure 2.2: Feynman diagrams for $e^+e^- \to b\bar{b}$ via γ and Z exchange.

It can be shown that forward-backward asymmetry for this process is :

$$A_{FB} \sim (T_{3L} - T_{3R})(T_{3L} + T_{3R} + 2/3\ \cos^2\theta_W) \tag{2.2}$$

where asymmetry, $A_{FB} = \frac{\sigma_F - \sigma_B}{\sigma_F + \sigma_B}$, T is the generator of $SU(2)$ symmetry and σ_F and σ_B are the forward and backward cross-sections. The amount of this asymmetry in the production is dependent on the third component of the weak isospin of the left-handed b quark (I^b_{3L}) as the coupling of b to the Z is proportional to $I^b_{3L} + \frac{1}{3}\sin^2\theta_W$, where $I^b_{3L} = 0$ if the b quark is singlet and $-1/2$ if the b has its doublet partner *i.e.* top (t) quark. Therefore, the left handed b quark is in a doublet and there has to exist a heavier quark to be its partner which is a t quark.

2.2 Top Quark Mass

The top quark acquires its mass via the Yukawa coupling $g_t = 2^{3/4}G_F^{1/2}m_t$ to a Higgs boson after spontaneous symmetry breaking. However, its value can not be predicted by the SM since particle masses are free parameters which have to be determined experimentally. In order to obtain finite predictions from higher order terms in perturbation theory, a renormalization scheme must be applied. It is often convenient in these procedures to treat the masses of quarks and leptons as *running parameters*, whose values depend on the momentum scale of the calculation. The quantity relevant to experiments, is the physical mass given by the pole in the quark propagator, and it is this mass which is measured in our analysis. The relation between the two definitions of the top quark mass in the commonly used modified minimal substraction ($\overline{\rm MS}$) scheme is given in below [6, 7],

$$\frac{m_t^{\rm Pole}}{m_t^{\overline{\rm MS}}(m_t^{\rm Pole})} = 1 + \frac{4}{3}\left(\frac{\alpha_s(m_t^{\rm Pole})}{\pi}\right) + 10.91\left(\frac{\alpha_s(m_t^{\rm Pole})}{\pi}\right)^2 \tag{2.3}$$

This ratio is ≈ 1.06 if $m_t^{\rm Pole} = 170$ GeV.

2.3 Top Quark Production

The top quark is the heaviest elementary particle yet discovered. Its mass, of the same order as the electroweak scale ($\sim v/\sqrt{2}$), is about twice that of the W and Z bosons and about 40 times larger than its isospin partner, the b quark. Because of its large mass, it can only be produced in the collisions of the particles where a sufficiently high center-of-mass energy ($\sqrt{s}$) can be achieved. The $p\bar{p}$ accelerator, Tevatron, at Fermilab ($\sqrt{s} = 1.8$ TeV) has been the only facility in the world where the top quarks have been produced. At the energies involved, the composite nature of these particles is evident, and one speaks of the actual collisions as being between their constituents (either quarks or gluons). Hence, the energy available in any given collision will only be some fraction of the $p\bar{p}$ system center-of-mass energy, since the interacting constituents (or partons) carry only a fraction of the proton or antiproton energy.

In $p\bar{p}$ collisions, there are two mechanisms for the top quark production : the pair-production of the top quarks via strong interaction ($t\bar{t}$ production) and single top production via electroweak interaction.

2.3.1 $t\bar{t}$ Production

The most likely means of producing top quarks is through the color interaction and since this interaction conserves quark flavor quantum numbers, the top quarks must be produced in $t\bar{t}$ pairs. At Tevatron, the dominant mechanisms for top production are expected to be the pair production processes $q\bar{q} \to t\bar{t}$ and $g\bar{g} \to t\bar{t}$ [8]. The leading order diagrams for top quark production are shown in the Figure 2.3. There are two major production channels, the $q\bar{q}$ annihilation ($q\bar{q} \to t\bar{t}$) and gluon fusion channels ($gg \to t\bar{t}$). Since, it is more likely for a significant fraction of the proton and antiproton momenta to be carried by one of its constituent quarks than by gluons, the $q\bar{q}$ annihilation channel dominates the production rate, and the degree of this dominance increases as a function of the top quark mass. The ($q\bar{q} \to t\bar{t}$) diagram dominates, contributing 90% of the total rate because top mass is almost 20% of the Tevatron beam energy and it is mostly quark which can be found with such a high fraction of the p or $\bar{p}$ momenta. There are also $q\bar{q}$ diagrams with γ^* or Z^* propagators which could result in $t\bar{t}$ final states. However, these are electroweak processes and the cross-sections are much smaller.

2.3.2 Single Top Quark Production

Single top quark production can occur through s, t or u-channel electroweak processes. Figures 2.4 and 2.5 correspond to the single top production [9, 10]. The dominant processes at $\sqrt{s}$=1.8 TeV are s-channel production of tb final state via off mass-shell W^* exchange and production of tqb final state via W-gluon fusion. Although the single top production cross-section is one-third that of the $t\bar{t}$ production

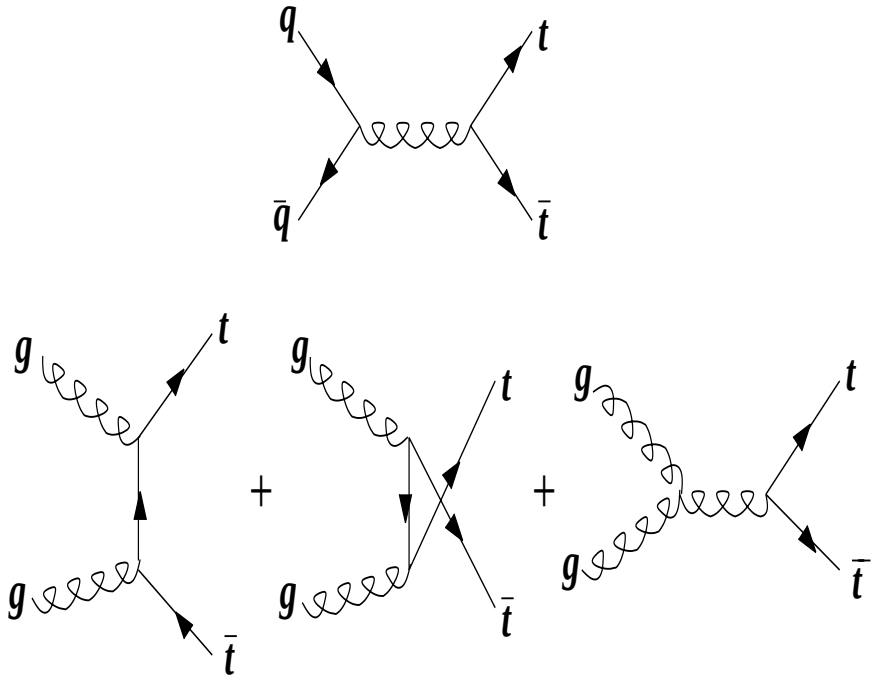

Figure 2.3: Feynman diagrams for lowest order $t\bar{t}$ production.

cross-section, the detection efficiencies for single top quark events are lower and the signal is much more difficult to separate from the background. At this time there is no direct measurement of single top production cross-section.

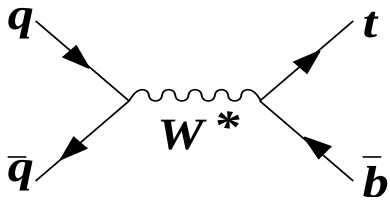

Figure 2.4: Feynman diagram for s-channel single top quark production.

2.4 Top Quark Decay

Weak interaction is the only interaction which does not conserve quark type or flavor and hence this is the only route open for top quark decay in the SM. Under $SU(2)$, the fermion transforms as doublets. The upper and lower members of any doublet can couple to a W boson, while a Z boson may only couple a particle to

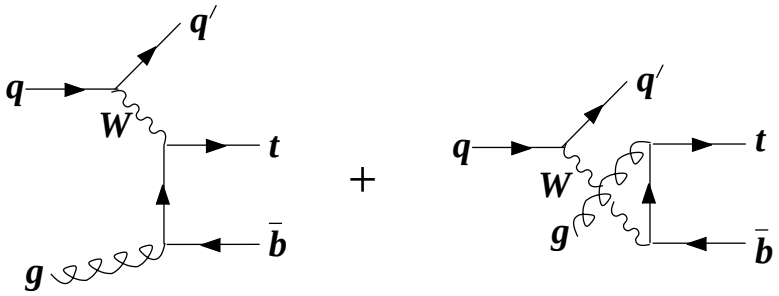

Figure 2.5: Feynman diagrams for single top quark production via W-gluon fusion.

itself. The decay width of top Γ_t will be difficult to measure but its theoretical accuracy lies within 1%. Within the SM, the top with $m_t > M_W + m_b$ will always decay into a W and a b [11]. The fraction of top quarks decaying into b quarks

$$B_b = \frac{\Gamma(t \to bW)}{\Gamma(t \to qW)} \tag{2.4}$$

has been measured by CDF to $B_b = 0.99 \pm 0.29$ [12].

Within the three generation SM, this ratio can be expressed by the CKM matrix elements as

$$B_b \equiv \frac{|V_{tb}|^2}{|V_{tb}|^2 + |V_{ts}|^2 + |V_{td}|^2} \tag{2.5}$$

where the denominator equals exactly 1.0 due to unitarity of the CKM matrix. Measurements in combination with the CKM unitarity yield $0.9990 < |V_{tb}| < 0.9993$ [**?**] *i.e.* the top quark decays almost exclusively (about 99.83%) into a b quark and a W boson. In an extended SM with a fourth generation of quarks the three generation unitarity does no longer hold and the denominator of Eqn. 2.5 can be smaller than 1.0. Measurements from DØ constrain a fourth generation b' quark to have a mass greater than $(m_t - m_W)$. Thus the top quark decay into b' would be suppressed and the original expression of Eqn. 2.5 is still valid. Measurements in combination with a four generation CKM matrix yield the weak constraint $0.05 < |V_{tb}| < 0.9993$. Therefore, the direct measurement of $|V_{tb}|$ is useful to search for physics beyond the SM.

2.5 $t\bar{t}$ Event Topology

Taking the two incoming partons from protons as longitudinal axis the produced $t\bar{t}$ pair is balanced in $p_\perp$ *i.e.* their momentum vectors are back to back in the plane transverse to the longitudinal axis. Since the partons can have a primordial transverse momentum and initial state radiation can provide additional $p_\perp$, the lon-

gitudinal axis does not necessarily coincide with the z-axis of the lab system. As already explained the top quark decays almost exclusively into a b quark and a W boson. While the W boson decays into a fermion antifermion pair of a weak isospin doublet, the relatively long living b quark builds a hadronic bound state before it decays. Taking into account the three different lepton generations, about 33% of all W bosons decay leptonically. The remaining 67% of W bosons decay into a quark antiquark pair, predominantly of the first two quark generations. Here about 11% of all $t\bar{t}$ events decay dileptonically. The remaining fraction of $t\bar{t}$ events decay to about 44% fully hadronically and semileptonically respectively. The fractions of all $t\bar{t}$ decay modes are summarized in Table 2.1.

$t\bar{t} \to (W^+b)(W^-b)$	$W \to e\nu_e$ (1/9)	$W \to \mu\nu_\mu$ (1/9)	$W \to \tau\nu_\tau$ (1/9)	$W \to q\bar{q}$ (2/3)
$W \to e\nu_e(1/9)$	1/81	1/81	1/81	2/27
$W \to \mu\nu_\mu$ (1/9)	1/81	1/81	1/81	2/27
$W \to \tau\nu_\tau$ (1/9)	1/81	1/81	1/81	2/27
$W \to q\bar{q}$ (2/3)	2/27	2/27	2/27	4/9

Table 2.1: Possible decay modes and their branching fractions from Ws for a $t\bar{t}$ pair.

The W boson can further decay either leptonically or hadronically. Depending upon both of the Ws decay, the $t\bar{t}$ event can be of three types. When both the Ws decay hadronically, the channel is called *all-jets channel*. In this channel, the final state consists of six or more jets (2 from the b decay and 4 from the W decays). There may also be additional jets from the initial or final state radiation. The branching ratio (BR) of this channel is about 44%, the largest amongst all the channels. But the disadvantage of this channel is, it suffers from the large background from QCD multijet events. In the second case, one W boson decays leptonically into $e\nu_e$, $\mu\nu_\mu$ or $\tau\nu_\tau$ and the other hadronically (into a quark-antiquark pair). This channel is called *semileptonic* or *lepton + jets channel*. The BR for this channel is about 3 times the BR for ee, $e\mu$, $\mu\mu$ *i.e.* 14.8%. The large BR implies a larger cross-section, but the W + jets process is a large enough background to make this channel a more challenging topology. In the third case, both the Ws decay leptonically giving ee, $\mu\mu$, $\tau\tau$, $e\mu$, $e\tau$ or $\mu\tau$. This channel is called *dilepton channel*. Events in which the leptons are of the same type have a branching fraction of 1.25% and the events in which the leptons are of different type have a branching fraction of about 2.5%. These are the cleanest channels *i.e.* they have very small backgrounds. Since in the present work we have made study in $t\bar{t} \to W^+bW^-b \to e\nu_e\mu\nu_\mu$+jets or simply $t\bar{t} \to e\mu$ channel ($e\mu$ channel), therefore this channel is described in the following section.

2.6 $e\mu$ Channel

When both the Ws decay leptonically, one going into an electron (e) and neutrino (ν_e) and the other to a muon (μ) and neutrino (ν_μ). In this thesis, we will call it to be an $e\mu$ channel. The Figure 2.6 shows the schematic diagram for the $t\bar{t} \rightarrow W^+bW^-b \rightarrow e\mu$+jets channel.

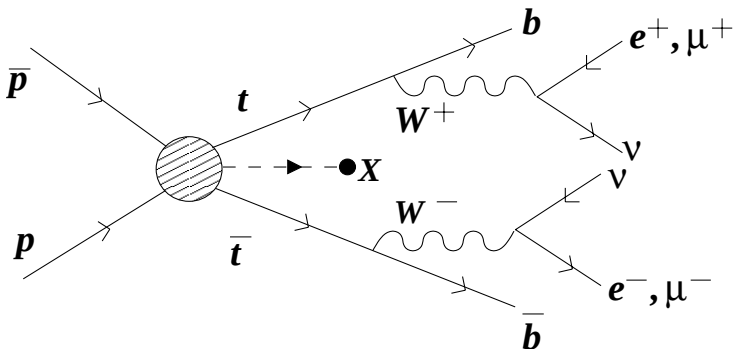

Figure 2.6: Schematic diagram of the $t\bar{t} \rightarrow e\mu X$ decay.

2.6.1 Signal

An $e\mu$ dilepton candidate consists of an event in which one of the W bosons decays to $e\nu_e$ and the other to $\mu\nu_\mu$. The $e\mu$ channel is having twice the BR of the ee and $\mu\mu$ channels while being free from much of the background from Z decay. The main features which characterize an $e\mu$ event are :

- One large transverse energy electron (E_T^e) from $W \rightarrow e\nu_e$ decay.
- One large transverse momentum muon (p_T^μ) from $W \rightarrow \mu\nu_\mu$ decay.
- Substantial missing transverse energy $\not\!\!E_T$ from two neutrinos.
- $\geq$ 2 jets from the fragmentation of the two b quarks (and initial/final state radiation).

The direct branching fraction for ($t\bar{t} \rightarrow b\bar{b}W^+W^- \rightarrow e\nu_e\mu\nu_\mu$ + jets) is 2.47%. This is increased by an additional 0.96% when the contributions from $t\bar{t} \rightarrow l\tau \rightarrow e\mu$ decays are included (where l can be e, μ or τ). However, the detection and reconstruction efficiencies for the τ events are somewhat smaller because the transverse energy (momentum) spectrum for the $e(\mu)$ from a τ decays is softer than those from the direct W decay and the presence of additional neutrinos leads to decrease in the total missing transverse energy $\not\!\!E_T^{cal}$.

2.6.2 Backgrounds

The background processes to the $e\mu$ channel can be divided into two main categories : physical and instrumental. These are discussed below.

Physical Backgrounds

These are the results of processes which lead to final state containing an electron and a muon with $\not\!\!E_T^{cal}$ and jets. These can mimic the signatures of top quark decay into $e\mu$ channel. The most significant of these are :

- **Z + jets Production**
  The inclusive production of a Z boson with associated jets can be a source of background $t\bar{t} \to e\mu$ events. Here the Z boson decays into $\tau^+\tau^-$ and taus further decay to give e and μ. The jets in these events are typically produced through radiative processes and have smaller transverse energies than those from the b jets in the top events. The production cross-section of $Z \to \tau\tau \to e\mu$ is ≈ 12 pb [14, 15] which is significantly larger than the $t\bar{t} \to e\mu$ cross-section. While the kinematics and topology can be used to suppress these events, they still provide significant background.

- **Drell-Yan $\tau^+\tau^-$ Pair Production**
  The Drell-Yan production of $\tau^+\tau^-$ pairs is also a source of background. As with the $Z \to \tau^+\tau^-$ decay case, the $\tau^+\tau^- \to e\mu$ decay can mimic the signatures of a top quark event. The jets here are also produced through radiative processes and have smaller transverse energies. Further suppression can be achieved by using the transverse energy spectra of the $e(\mu)$, which is even softer than that from $Z \to \tau^+\tau^- \to e\mu$. The cross-section for this process is ≈ 6 pb [16].

- **WW Pair Production**
  The WW pairs are produced at the Tevatron Drell-Yan process. The final $e\mu$ state comes from the decays of the two W bosons. There is also a small contribution from the $W \to \tau\nu_\tau$ decay with a sequential $\tau \to e(\mu)\nu\bar{\nu}$ decay. The production cross-section for $p\bar{p} \to W^+W^-$ at the Tevatron is ≈ 10 pb. The branching fractions of $WW \to e\mu$ (including τ decays) is 3.43% so that the production cross-section for the $e\mu$ final state is about 0.34 pb. Also, like other Drell-Yan processes, the jets in these events are produced by radiative processes and the E_T spectra are softer. However, in terms of lepton final state, the transverse energy spectra of leptons are identical to those of $t\bar{t}$ events.

Instrumental Backgrounds

There are some backgrounds which come from the instrumental effects in the detector and arise from the misidentification of jets as electrons. These can be conveniently separated into two categories depending on the source of the muon in the events.

- **W + jets Production**
  The production of W + jets events is one of the main sources of instrumental background. The measured production cross-section for $p\bar{p} \to WX \to \mu\nu X$ is ≈ 2.42 nb. If one of the associated jets is misidentified as an electron then the final state can mimic the $t\bar{t} \to e\mu X$ signature.

- **$b\bar{b}$ and $c\bar{c}$ Production (QCD multi-jet processes)**
  This background is related to the production of QCD jets (mainly $b\bar{b}$ and $c\bar{c}$). The heavy quark (b or c) can have a semileptonic decay to a muon and may transfer most of its energy to the muon, leaving little energy to hadronize. Such jets can easily be missed in reconstruction. If one of the other jets in the event is misidentified as an electron, then the final state would be one electron (misidentified jet), one muon (from b or c decay) and sufficient missing transverse energy. Despite heavy suppression from kinematical and topological constraints, this background can still be a source of significant problem because of the large $b\bar{b}$ and $c\bar{c}$ cross-sections.

2.7 Role of the Top Quark Mass

One of the most interesting top measurements will be the precise determination of the top quark mass which allows in particular the improvement of the accuracy of supersymmetric exclusion limits. The measurement of the helicity states of the W boson from the top quark decay within the percent level will allow to search for deviations of the SM. The measurement of the $t\bar{t}$ spin correlation constitutes the direct check of the top quark spin 1/2 and thus a fundamental test of the quark spin and the QCD predictions for its production. For more details refer to [17]. Precise determination of the top quark mass will be the test of QCD predictions for its production. In addition, the top quark mass can provide information about the Higgs sector.

The W mass is also related to the *Fermi Constant* G_F, which is the effective weak coupling strength at low energy

$$m_W = \frac{1}{2} \frac{g_1}{(\sqrt{2} G_F)^{\frac{1}{2}}} \tag{2.6}$$

In the $SU(2) \times U(1)$ model, g_1 is also related to the fine structure constant α, yielding :

$$m_W = \frac{1}{2} \left(\frac{\pi \alpha}{\sqrt{2} G_F} \right)^{\frac{1}{2}} \frac{1}{\sin\theta_W} \tag{2.7}$$

$$m_Z = \frac{A}{\sin\theta_W \, \cos\theta_W} \tag{2.8}$$

All of the above holds exactly at lowest order in the SM. However, higher order

effects (or radiative corrections) cause slight modifications to the above equations. Since, m_W is known less precisely than m_Z, α, G_F and $\sin^2\theta_W$, it is convenient to absorb the contributions of these higher order effects into the equation for m_W :

$$m_W = \frac{A}{\sin\theta_W\sqrt{1-\Delta R}} \tag{2.9}$$

where ΔR is the radiative correction. The radiative corrections to the W mass enter due to fermion and Higgs boson loops in the W propagator. The sizes of the corrections depend on the masses of the particles in the loops. The contributions from the fermion loops are proportional to m_f^2/m_W^2, and hence the top quark provides the dominant term. Therefore, if one measures both m_t and m_W very precisely, above equation provides a constraint on the allowed Higgs boson mass m_H.

Unfortunately, the Higgs Loop contribution to ΔR is proportional to $ln(\frac{m_H}{m_W})$ *i.e.* one needs to measure m_W and m_t very precisely in order to narrow down the allowed range for m_H. Figure 1.1 shows the variation of m_W as a function of m_t for various Higgs masses [18]. The width of the curves is due to uncertainty in the measurement of other SM parameters.

2.8 Top Quark Mass Measurements

The top quark mass measurements in DØ and CDF for each different channel are shown in Figure 2.7. The errors mentioned include both statistical as well as systematical error.

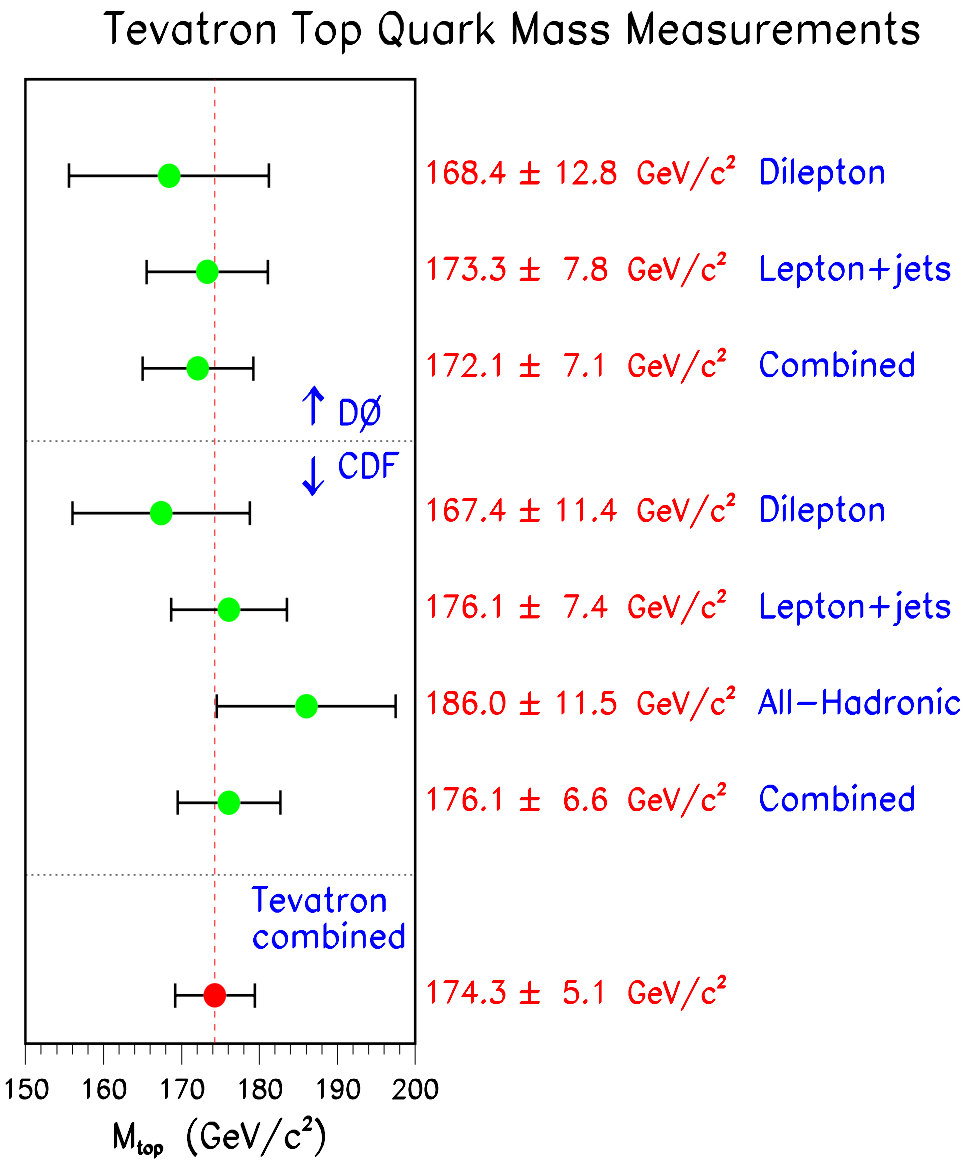

Figure 2.7: Summary graph of DØ and CDF top quark mass results.

Chapter 3

Tevatron

In our study, we have analyzed the data which was collected using the DØ detector at the Tevatron $p\bar{p}$ collider located at Fermi National Accelerator Laboratory during (1992-1996). The Fermilab Tevatron collides protons and antiprotons at a center-of-mass energy ($\sqrt{s}$) of 1.8 TeV. Until the LHC at CERN, where $\sqrt{s} = 14$ TeV is built, this is the largest center-of-mass energy available. The Tevatron is among the more recent machines in a long line of accelerators which have contributed tremendously to the development of particle physics [19, 20].

The production of top quark pairs requires a large center-of-mass energy and therefore a colliding beam experiment is necessary and the detection of top quark pairs requires a detector capable of identifying and measuring the energies of electrons, muons, jets and neutrinos. The preference of proton beams over electron beams for this purpose comes from consideration of the synchrotron radiation emitted by an accelerating charged particle. The energy dissipated by synchrotron radiation decreases as the fourth power of the mass of the accelerated particle and hence it is far easier to accelerate proton beams to the needed energy. The drawback is that protons themselves are complex objects comprised of quarks and gluons, which complicates the analysis of the collisions and results in only some fraction of the total proton energy being delivered to any particular collision.

One way of implementing a colliding beam experiment is to collide beam of a particles with beams of its antiparticles. As the antiparticle shares all the characteristics of the particle but has opposite electric charge, the two beams will circulate in opposite directions in the same ring of magnets. Because of this, there is no need to reconstruct a separate accelerating apparatus for each beam.

3.1 Principles of Operation

The Tevatron is a complex device and actually a total of seven acceleration devices are used to produce the colliding proton and antiproton beams as shown in Figure 3.1. The Tevatron has a long circumference of 3.7 miles which reduces the energy loss due to radiation. The Tevatron consists of the following different parts

as briefly explained below (details can be found in [21, 22]) :

- **Cockroft-Walton Accelerator**
  The beam's birth place, a Cockroft-Walton electrostatic accelerator is the preaccelerator. The process begins with a pressurized bottle of hydrogen gas. Hydrogen gas is used as a source of protons. The proton beam initially starts with 18 keV H^- ions, which are accelerated to 750 keV by a Cockroft-Walton electrostatic generator. The Fermilab preaccelerator operates in a pulsed mode with a frequency of 15 Hz.

- **Linac**
  The H^- ions from Cockroft-Walton generator are injected into the Linac. It is 150 m long. This device induces an oscillating electric field between a series of electrodes thus raising the energy of the ions to 200 MeV. At this stage, the H^- ions are passed through a carbon foil which strips the two electrons from the ion to create a beam of protons H^+.

- **Booster-Synchrotron Ring**
  The protons are then steered into the Booster Synchrotron Ring (151 m diameter). It is a cyclic machine which confines the protons to a closed orbit using bending magnets. On each pass around the ring, the particle's energy is increased by acceleration in a synchronized radio-frequency (RF) cavity. As the momentum increases, the magnetic field in the bending magnets must be increased if the particles are to remain in the ring (since $p = qB\rho$; p is the particle momenta, q is the particle charge, B is the magnetic field and ρ is the radius of curvature). Thus for a given ring the maximum particle energy is limited by the maximum strength of the magnets and on exiting the booster the protons have an energy of 8 GeV. As the energy of the protons increases in this ring, the magnetic field is increased accordingly to keep the protons in the ring.

- **Main Ring (MR)**
  MR is a 400 GeV proton synchrotron with a radius of 1000 m. This ring is composed of about 1000 conventional (Cu - coiled) magnets. MR is employed to further accelerate protons upto 120 GeV and proton beam strikes a nickel target to produce antiprotons. The protons circulate around the 3.7 miles long MR in bunches containing 2×10^{12} protons each. Six bunches circulate around the MR simultaneously. The bunch crossing time τ for any part on the ring is

$$\tau \sim \frac{\text{Circumference}}{c\text{N}_{\text{bunch}}} = 3.5\ \mu\text{s} \tag{3.1}$$

- The Target Hall in which 2×10^7 antiprotons are produced by extracting proton bunches onto a nickle/copper target. Then a magnetic lens is used to form and inject the antiprotons into the debuncher in which a coherent

beam is formed. This process is known as "stochastic cooling" process and it reduces the transverse movement of the antiprotons. This process continues until about 4×10^{11} antiprotons are stored. The antiprotons are then injected into the MR where they are accelerated to 150 GeV and then transferred to the Tevatron ring. In the Tevatron, antiprotons circulate in the opposite direction to the protons. Both protons and antiprotons are accelerated to acquire an energy of 900 GeV before they collide at DØ *i.e.* the center-of-mass energy of $p\bar{p}$ collisions is 1.8 TeV. At present, the center-of-mass energy of $p\bar{p}$ collisions in DØ upgrade for Run II is 2.0 TeV .

The instantaneous luminosity is given by

$$L_{ins} = \frac{N_p N_{\bar{p}}}{\tau S} \sim 5 \times 10^{30} \text{ sec}^{-1}\text{cm}^{-2} = 0.5 \text{ nb}^{-1}/\text{sec} \tag{3.2}$$

where N_p and $N_{\bar{p}}$ are the number of protons and antiprotons per bunch respectively and S is the geometrical area of the interaction. The integrated luminosity, $\mathcal{L}$ is defined as

$$\mathcal{L} = \int L_{inst} dt \tag{3.3}$$

The cross-section σ for a process is given by

$$\sigma = \frac{N}{\mathcal{L}} \tag{3.4}$$

where N is the number of events produced by the process.

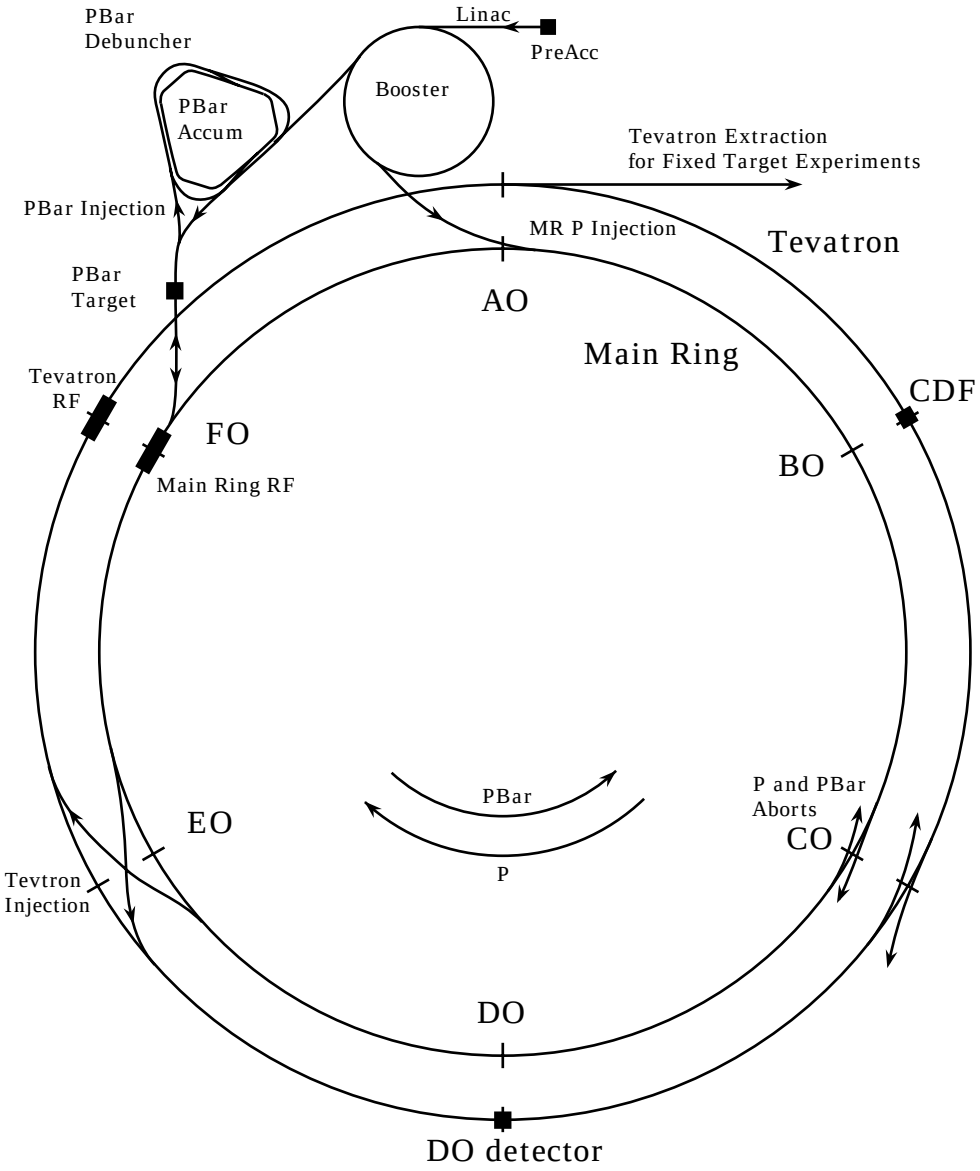

Figure 3.1: Schematic diagram of Tevatron collider at Fermilab.

Chapter 4

DØ Detector

The final state from $p\bar{p}$ interaction may contain electrons, muons, jets and neutrinos. The DØ detector is designed to identify and measure the energy of all these particles. The DØ detector is a multipurpose detector with almost 4π coverage at one of the collision point of the Fermilab Tevatron $p\bar{p}$ collider. With an emphasis on precision measurements of leptons, photons and jets, DØ is designed principally to study high p_T physics and high mass states. This includes the topics like : the search for the top quark (primarily in the leptonic and semileptonic decay modes), precision mass (and width) studies in the electroweak sector with the stress on a precise determination of the W/Z mass ratio, measurements of the $WW\gamma$ coupling, searches for non-standard top and Higgs particle with W width studies, high p_T QCD physics as well as searches for new phenomena beyond the Standard Model.

4.1 Overview of DØ

The physics which is to be emphasized determines the ideal detector. An ideal detector consists of three main different parts. Tracking system, which records the hits encountered because of the passing particles in 3-dimensions. The calorimeter records the energy of the particles which are coming out of the tracking detector. A calorimeter would be so thick that it will absorb all the incident particles energies, basically stopping all the known particles coming out except muons and neutrinos. A muon system to detect muons. Neutrinos are chargeless weakly interacting particles and not detected directly, but are accounted for the imbalance left in the total detected momentum transverse to the beam.

The DØ detector as stated above is a multipurpose detector specially designed to provide good electron and muon resolution, superior electromagnetic and hadronic energy resolution through highly segmented calorimetry and full solid angle coverage. The basic components of the DØ detector are :

- Central Detector
- Calorimetry

- Muon Detector

A cutaway isometric view of the detector is shown below in Figure 4.1.

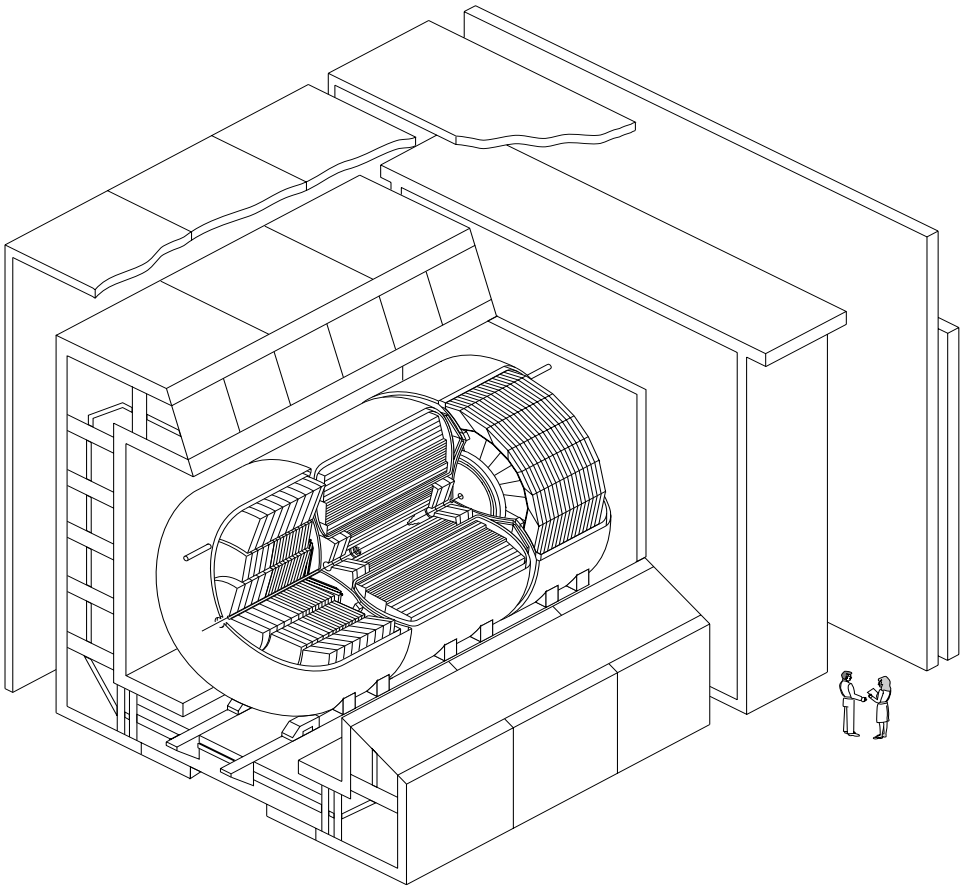

Figure 4.1: Cutaway view of the DØ detector.

The central detector is designed to trace the trajectory of charged particles (tracking). This tracking system is designed to be the closest to the point of interaction to thereby minimize multiple scattering and identify secondary vertices. The central detector is surrounded by the calorimeter. The calorimeter is designed to measure the energy of particles and should be thick enough to stop particles, except neutrinos and muons which escape, and measure the deposited energy. Since the energy deposited by a lepton in matter is inversely proportional to the mass of the particle, muons escape the calorimeter with little energy deposition. A tracking system should contain as little material as possible to minimize the probability of inelastic interaction before particles reach the calorimeter. Muons are detected by a 3-layer proportional drift chamber surrounding the calorimeter. Neutrinos interact only weakly and can not be stopped by the calorimeter. Neutrinos are identified by balancing the energy flow transverse to the beam.

The DØ detector weighs 5500 tons and the absence of a central magnetic field makes it possible for the detector to fit in a compact volume of (13m high, 11m wide, 17m long) [23]. The DØ detector is not designed for tracking and identification of individual particles within jets. A better jet energy measurement is achieved by the calorimeter because of the absence of a central magnetic field. A magnetic field would deflect the charged particle out of the jets.

4.1.1 DØ Coordinate System

DØ uses a right-handed coordinate system with the +ve z-axis along the beam in the direction of the protons and the y-axis points up as shown in Figure 4.2. The angular variables are defined so that $\phi = \pi/2$ is parallel to the +ve y-axis and $\theta = 0$ is coincident with the +ve z-axis. The azimuthal angle (ϕ) is measured w.r.t. the +x direction, and the polar angle (θ) is measured w.r.t. the +z direction. The transverse momentum (momentum vector projected on the xy plane) $\vec{p}_T$, for these particles is small, so momentum conservation can be applied in the transverse plane. p_T is defined as :

$$p_T \equiv |\vec{p}_T| = p\sin\theta \tag{4.1}$$

This is particularly used due to the fact that in a $p\bar{p}$ collisions, the total secondary momentum along the beam of the colliding partons are not known since the secondary particles may escape down the beam pipe. However, their transverse momenta are very small compared to their momenta along the beam *i.e.* plane perpendicular to the beam axis. So, one can apply momentum conservation in the transverse plane. The *transverse energy* is defined as a vector whose direction is the direction of $\vec{p}_T$ in the transverse plane. If treated as a vector, the direction of E_T should be taken to be the same as the $\vec{p}_T$. The magnitude of E_T is given as :

$$E_T = E\sin\theta \tag{4.2}$$

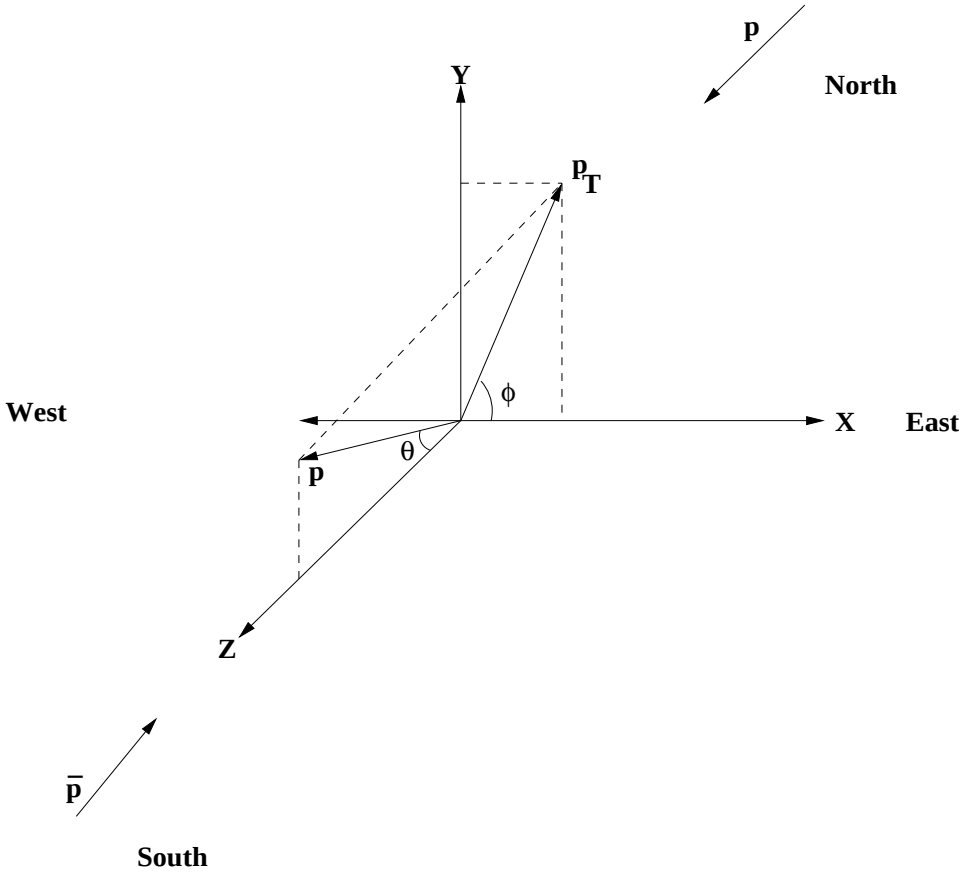

Figure 4.2: DØ coordinate system.

Pseudorapidity (η) is frequently used instead of θ. It is defined as

$$\eta = -ln(\tan\frac{\theta}{2}) \tag{4.3}$$

which is an approximation of the rapidity (y) defined as

$$y = \frac{1}{2}ln(\frac{E+p_z}{E-p_z}) \tag{4.4}$$

in the high energy limit that $m/E \ll 1$, where $m(=\sqrt{E^2-p^2})$ is the invariant mass, the variable η approaches the true rapidity (y) of the particle *i.e.* $y \approx \eta$.

Rapidity is useful quantity because it is invariant under longitudinal Lorentz boosts. Also, in many processes the differential cross-sections are constant in rapidity. For example, in minimum bias events the quantity $dN/d\eta \approx$ constant.

It is often convenient to express polar angles in the detector rest frame denoted η_{det} which is computed w.r.t. $x = y = z = 0$. In practice, the interaction point is

characterized by a Gaussian distribution centered at $z = 0$ with $\sigma_z \approx 30$ cm, so that η and η_{det} may differ slightly for a given particle.

4.2 Central Detector

The purpose of the central detector (CD) is to reconstruct the 3-dimensional trajectory of each charged particle passing through. The length of the CD is 270 cm and its radius is 78 cm. It provides charged particle tracking in the region $|\eta| < 3.2$ with good spatial resolution of individual particles and a good determination of the ionization (dE/dx). Tracking in the CD is important because,

- Using the tracking information, we can determine whether an electromagnetic shower in the calorimeter is produced by an electron, a photon or π^0.
- The precise measurement of the location of the interaction vertex (collision point) is done using the CD tracking information. The precise vertex measurements can be used for the calorimeter, position measurements. The CD system of the DØ detector has no magnetic field so momentum information is not available at this stage.
- By measuring dE/dx for a track, one can decide if a track is caused by photon conversion, $\gamma \rightarrow e^+e^-$.

The CD consists of four sub-detectors as shown in Figure 4.3. These four sub-detectors, ordered from inside to outside, are :

- The vertex drift chamber (VTX) surrounding the beryllium beam pipe.
- The transition radiation detector (TRD) surrounding the VTX.
- The central drift chamber (CDC) surrounding the TRD.
- The forward drift chambers (FDC) at each end of the central detectors.

4.2.1 Basics of Drift Chamber Operation

A charged particle can interact in several different ways with a medium through which it is passing. At present, tracking detectors only utilize the Coulomb interaction with atoms and nuclei in a medium. Coulomb interactions can be further subdivided into three principle classes : interaction with electrons in individual atoms (ionization), interaction with the nucleus and collective effects such as Cerenkov radiation. The working principle of the drift chambers is based on the fact that energetic charged particles cause ionization along their path as they pass through a gas. When a charged particle passes through a gas, it will interact with nearby

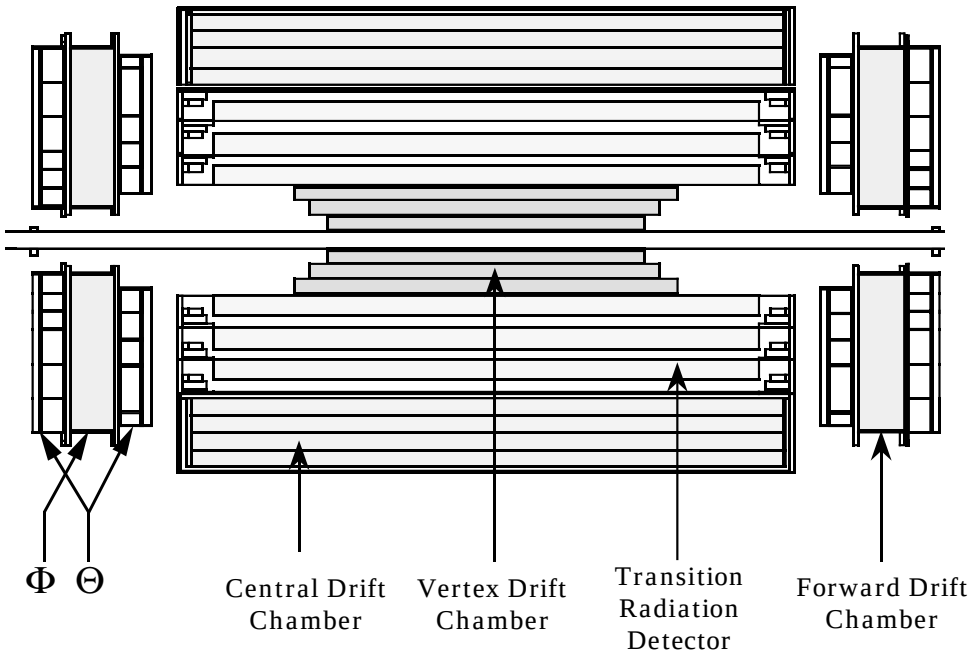

Figure 4.3: Side view of the DØ tracking system.

atomic electrons, creating electron/ion pairs along its path. The number of electron/ion pairs created depends on the energy of the particle and the type of the gas. An electric field is used to collect the liberated electrons and cause them to drift through the gas towards the positive electrode (sense wire). The drifting electron causes further ionization along the way to the positive electrode. As the accelerated electron gets closer to the anode it experiences a stronger electric field causing electron to accelerate faster and gain enough energy to cause further ionization. This phenomenon in which the number of the electrons increases exponentially is called the *avalanche effect*. This effect gives rise to a measurable current which is proportional to the original number of ions created. The ratio of the final number of electrons collected by the anode to the initial number deposited is called the *gas gain*. The gas gain is of the order of $(10^4 - 10^6)$ for a typical drift chamber. The velocity of a drift electron is a known quantity determined by the strength of the field and the density, pressure and temperature of the gas. The fact that the velocity of the electron is known along its path to the anode enables us to measure the position of the source particle knowing the drift time. In order to obtain a linear relationship between the electric field and the velocity of the electron, it is necessary to have an electric field which is constant over a large volume. The large electric field needed to drift electrons far away from the anode is generated by a very thin wire ($20 - 100$ μm in diameter). Additional electrodes, known as field-shaping electrodes are used to make the electric field more uniform.

4.2.2 Vertex Drift Chamber

The vertex drift chamber (VTX) is the innermost drift chamber used for vertex position measurement. It consists of four carbon fiber cylinder surrounding three concentric layers. The innermost layer has a length of 97 cm and the next two layers are still longer by about 10 cm, with the outermost being about 117 cm in length. The VTX extends from $r = 3.7$ cm to $r = 16.2$ cm radially. The length of the innermost layer is 97 cm and each successive layer is about 10 cm longer. The gas used for the operation of the VTX is a CO_2-ethane mixture maintained at 1 atm with a small admixture of H_2O. Figure 4.4 shows an end view of the VTX chamber. The VTX chamber is a jet chamber. In a jet chamber sense wires are strung in

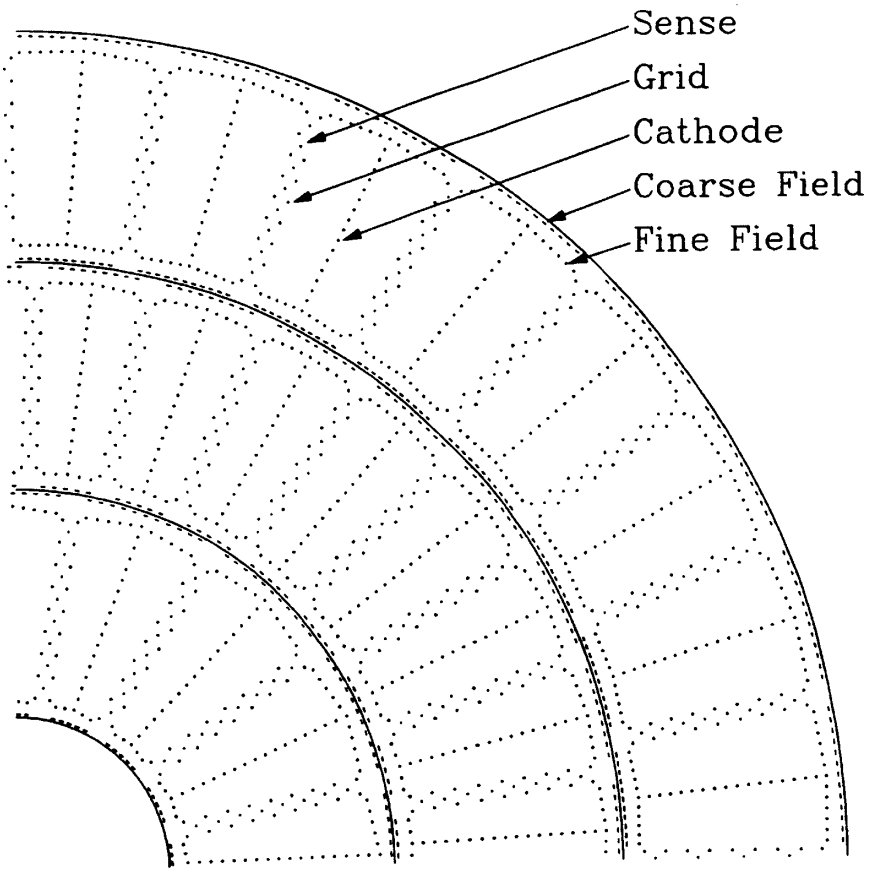

Figure 4.4: End view of one quadrant of the DØ VTX chamber.

planes parallel to the path of the particles from the interaction vertex. The inner layer is divided into 16, while the two outer layers into 32 cells each. Each layer is rotated in ϕ w.r.t. the adjacent layer to eliminate dead regions and left-right ambiguities. The drift time measurements only yield the distance electrons have drifted, since the drift can be from either left or right, the position of any single

hit is ambiguous. Each cell contains 8 sense wires, which are staggered out of the $(r-\phi)$ plane by 100 μm to lessen left-right ambiguities. The (r,ϕ) position of the track is determined from the drift time. The z-position is determined using charge division in which the sense wire is read out at both ends.

4.2.3 Transition Radiation Detector

The transition radiation detector (TRD) is located in the space between the VTX and the CDC. It is used to provide additional electron identification availability (independent of the calorimeter). The working principle of the TRD is based on the fact that the charged particles radiate photons in the forward direction as they traverse the boundary between the two media with different dielectric constants. The radiation intensity is proportional to $\gamma \equiv \frac{1}{\sqrt{1-v^2/c^2}} = E/mc^2$ and concentrated in a cone with a half angle proportional to $1/\gamma$. For highly relativistic charged particles ($\gamma > 10^3$), the radiation is in the X-ray frequency range. Using these characteristics, TRD discriminates particles with different masses which have similar energies. In order to obtain a reasonable signal, the charged particle has to traverse a large number of boundaries. The DØ transition radiation detector is utilized to discriminate electrons from heavier particles. Electrons are the only particles at the Tevatron likely to cause detectable transition radiation. The TRD has three layers, each layer containing 393 sublayers of 18 μm polypropylene foils with a mean spacing of 150 μm. The gaps between the foils are filled with dry nitrogen. Each radiation is surrounded by a xenon filled drift chamber to detect the transition X-ray radiation. The TRD provides a factor of 10 rejection against pions with a high efficiency of 90% for isolated electrons. For further information on TRD refer to [23, 24].

4.2.4 Central Drift Chamber

The central drift chamber (CDC) is the outermost sub-detector of the CD. It is in between the TRD and the central calorimeter and it is used to detect tracks at large angles. The pseudorapidity range of $|\mu| \leq 1.2$ is covered by CDC. The CDC consists of four layers which extend radially from $r = 49.5$ cm to $r = 74.5$ cm and 184 cm long. Figure 4.5 shows the end-view of a position of the CDC. Each layer of the CDC is divided into 32 identical sectors which are arranged in a cylindrical ring. Within each module, there are 7 equally spaced tungsten sense wires of diameter 30 μm, staggered 200 μm relative to each other to resolve left-right ambiguities. The CDC has a jet geometry similar to the vertex chamber. The (r,ϕ) position of a hit is determined using the drift time and the z-position is measured by comparing the arrival times of the avalanche induced pulse at both ends of the inductive delay lines placed in the module walls in the sense wire plane.

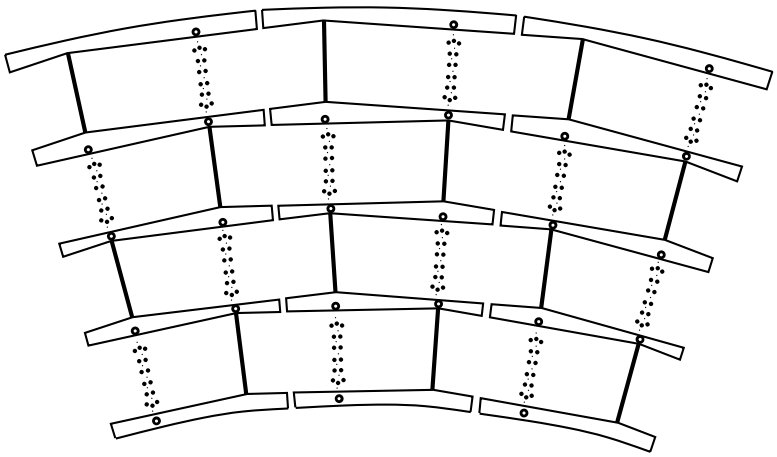

Figure 4.5: End view of three CDC modules.

4.2.5 Forward Drift Chambers

The forward drift chambers (FDCs), covering $1.2 \leq |\mu| \leq 3.1$, are located at both ends of the CDC. This translates to a θ range of $\sim 5^{o} - 34^{o}$. There are two sets of chambers, one located at each end of the CDC. Each set of FDC consists of three layers of chambers, two Θ layers sandwiching Φ layer (Figure 4.6). The Φ layer is divided into 36 azimuthal drift cells, each containing 16 sense wires strung radially. The two Θ layers consist of 4 separate quadrants, each containing 6 rectangular drift cells. The sense wires in each cell are oriented parallel to the z-axis. In each rectangular drift cell there is a delay line similar to that of CDC to measure the position along the length of the cell. However, there is no delay line in the Φ layer. The outer Θ chambers are rotated by 45^{o} w.r.t. each other.

4.3 Calorimeter

The calorimeter is the centerpiece of DØ detector. Because of the absence of a central magnetic field at the DØ experiment, the calorimeter is the only source of precise energy measurements for most of the particles. Furthermore, it provides much of the information necessary for the identification of electrons, photons, jets and muons and plays an essential role in the determination of the missing energy ($\not\!\!E_T$). A more detailed discussion can be found elsewhere [20, 25].

4.3.1 Basics of the Calorimeter Operation

Analogous to the well known laboratory device for measuring heat, a calorimeter is a device that measures the total energy deposited by a particle or cluster of

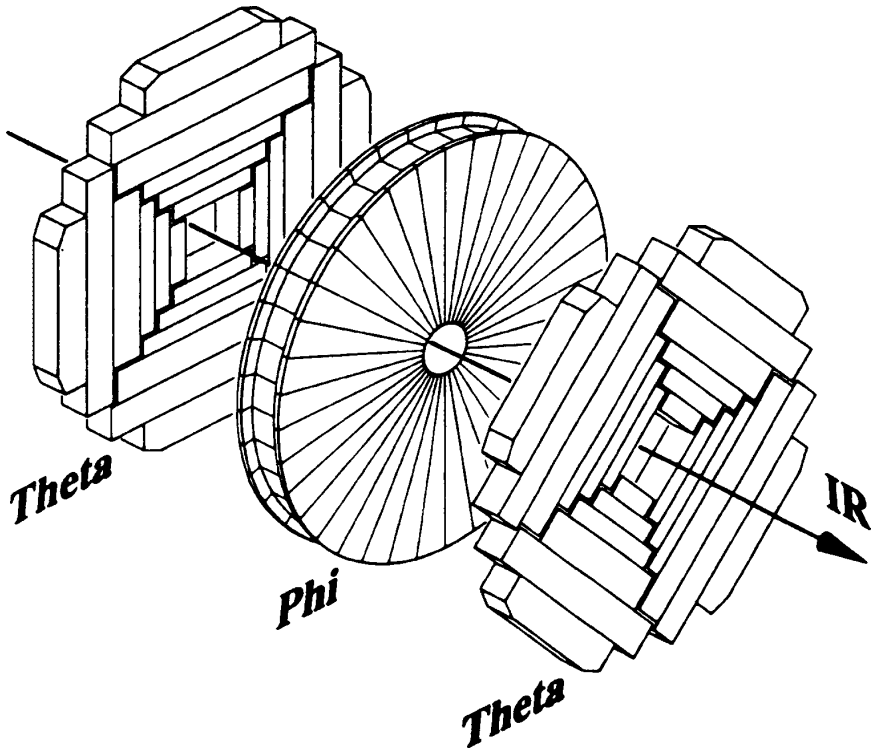

Figure 4.6: One of the two sets of the FDCs.

particles. A calorimeter is a block of matter of sufficient thickness which intercepts the primary particle and causes it to interact and deposit all of its energy in the subsequent cascade or shower of increasingly lower energy particles. In calorimetery, one measures the energy deposited by a particle, by stopping it in an absorber. As a high energy electron ($E^e \gg 10$ MeV) passes through a dense material, it interacts electromagnetically with atomic nuclei in the material and emits energetic photon (Bremsstrahlung). A high energy photon, in turn, produces electron-positron pairs. The photons and electron-positron pairs created through Bremsstrahlung or pair production produce more electrons, positrons and photons undergoing the same processes. Therefore, an energetic photon or electron passing through dense media can produce a shower of electrons, positrons and photons known as an *electromagnetic shower*. As the shower develops, it loses energy mostly due to ionization until it does not have enough energy to go through showering processes. The rate of energy loss in a material is constant and depends only on the type of the material. The rate is expressed is

$$\frac{(dE/dx)}{E} = -\frac{1}{X_0} \qquad or \qquad E = E_0 e^{-x/X_0} \tag{4.5}$$

where X_0 is called the *radiation length*.

Hadrons, on the other hand, lose energy by colliding inelastically with atomic nuclei. The hadrons produced by these collisions can cause more inelastic collisions to produce a hadronic shower. The hadronic shower continues to develop until it loses its energy due to ionization and inelastic collisions. The rate of energy loss for hadronic shower is the same as in Eqn. 4.5 with X_0 replaced by the *nuclear absorption length* λ. For uranium, $\lambda \sim 10.5$ cm, whereas $X_0 \sim 3.2$ mm. So, hadronic showers are generally both longitudinally and transversely larger than electromagnetic showers.

In order to measure the energy of the low energy particles produced through showering, layers of an ionization sensitive material can be inserted in the dense particle absorber. Since, this active medium only sees a fraction of the energy lost by the incident particle, this type of calorimeter is called a sampling calorimeter. The fraction of the energy detected is known as the sampling fraction.

The response of the calorimeter to electromagnetic and hadronic showers is different. Since neutrinos and muons produced by K and π decays escape the calorimeter and the nuclei break-up energy is not measured, the calorimeter response to hadronic showers is smaller. This difference in calorimeter response to electromagnetic and hadronic showers is quantified by measuring the ratio of the response to electron and pions, known as the e/π ratio. Hadronic showers can have electromagnetic components through η and π decays to photons. The fraction of hadrons which cause electromagnetic showers may change from shower to shower. In order to have an energy resolution independent of this, it is desirable to have $e/\pi = 1$. A calorimeter with $e/\pi \sim 1$ is called a *compensating calorimeter*.

4.3.2 Calorimeter Configuration

The DØ calorimeter is a sampling calorimeter. In the DØ calorimeter, uranium is used as the absorber material and liquid argon (LAr) as the sampling medium. Some of the important parameters for uranium are :

Density	18.95 g/cm^3
Radiation Length (X_0)	6.00 g/cm^2
Nuclear Interaction Length (λ)	1.99 g/cm^2
Moliére Radius (ρ_M)	$\approx$ 1.1 cm

where $(\rho_M) \approx X_0/\epsilon_c$ and $\epsilon_c \approx \frac{580}{Z}$(MeV) is the critical energy. LAr is chosen as the sampling medium since it allows uniform gain over the entire calorimeter, is relatively simple to calibrate, allows flexibility in the segmentation of the calorimeter into readout cells and is not susceptible to radiation damage. The calorimeter is divided into a central calorimeter (CC), covering $|\mu| < 1.2$ and two end calorimeters (EC) with an approximation coverage of $1.1 < |\mu| < 4.5$. Since the sampling material used in the calorimeter is LAr, the calorimeter has to be kept cold. Therefore, both

CC and EC are placed inside cryostats. Figure 4.7 shows the isometric view of the DØ calorimeter.

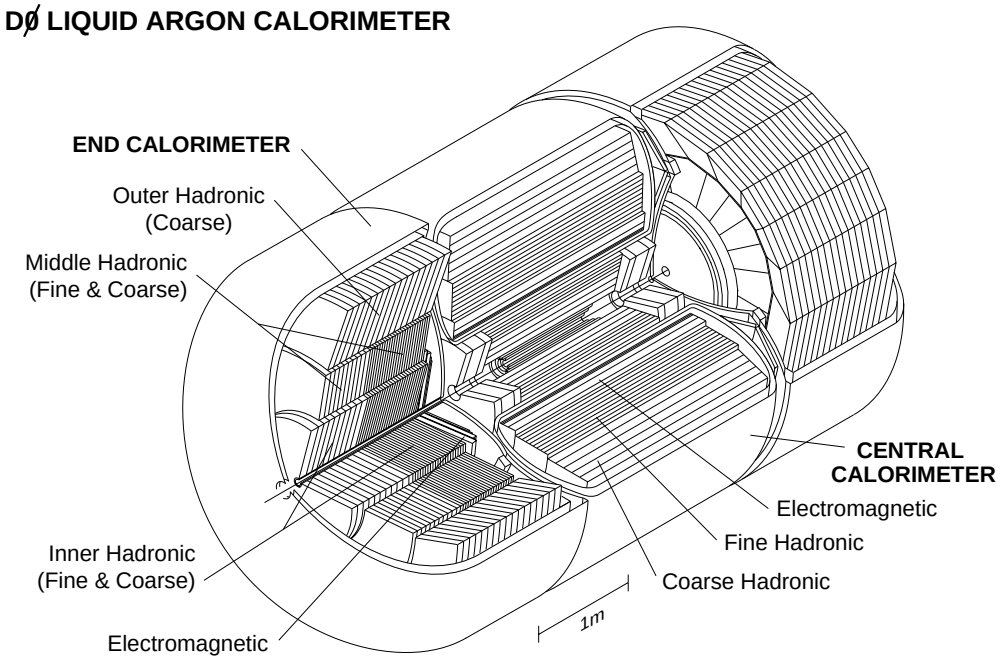

Figure 4.7: Isometric view of the DØ calorimeter.

Central Calorimeter

The central calorimeter (CC) consists of three concentric cylindrical shells 226 cm in length with a radial coverage of 75 cm$< r <$222 cm. The inner layer contains 32 electromagnetic (EM) modules for electromagnetic shower measurement. The middle layer contains 16 fine hadronic (FH) modules, measuring hadronic showers. The outer layer consists of 16 coarse hadronic (CH) modules, to reduce the leakage out of the calorimeter to the muon system. In order to reduce the energy loss in cracks, the EM, FH and CH module boundaries are arranged so that there are no cracks, pointing at the interaction point. The typical coverage of a readout cell is 0.1×0.1 in $(\eta - \phi)$ space. The cells in the third layer of the electromagnetic modules are smaller (0.05×0.05) and the cells in pseudorapidity beyond 3.2 are larger.

End Calorimeter

There are two end calorimeters (ECs), one located at the north : the North End Calorimeter (ECN) and the other at the south : the South End Calorimeter (ECS), ends of the central tracking system.

4.3.3 Calorimeter Performance

The calorimeter energy resolution is given by

$$\left(\frac{\sigma}{E}\right)^2 = C^2 + \frac{S^2}{E} + \frac{N^2}{E^2}, \tag{4.6}$$

where C, S and N are constants reflecting the error due to calibration gain, statistical fluctuation and noise respectively. The measured values for these constants are : For electrons

$$\mathrm{C} = 0.003 \pm 0.002, \quad \mathrm{S} = 0.157 \pm 0.005 \ (\mathrm{GeV})^{1/2}, \quad \mathrm{N} \approx 0.140 \ \mathrm{GeV}, \tag{4.7}$$

For pions

$$\mathrm{C} = 0.032 \pm 0.004, \quad \mathrm{S} = 0.41 \pm 0.04 \ (\mathrm{GeV})^{1/2}, \quad \mathrm{N} \approx 1.28 \ \mathrm{GeV}, \tag{4.8}$$

The e/π ratio ranges from 1.04 at 150 GeV to 1.11 at 10 GeV and the resolution for position measurements is about 0.8-1.2 min.

4.4 Muon System

In order for a particle to pass through the material in the calorimeter, it must (i) have lifetime sufficient to travel several meters before decaying, (ii) not participate in the strong interaction (and thereby cause a hadronic shower), and (iii) be unlikely to lose substantial energy due to bremsstrahlung (thereby initiating an electromagnetic shower). The only charged particle known to have these properties is the muon, and therefore, detectors are constructed outside of the calorimeter expressly for muon detection. Since, muons deposit little of their energy in the calorimeter, a spectrometer must be used to measure their momenta. This is formed by layers of proportional drift tubes (PDTs) surrounding a magnetized iron toroid. Measurement of the particle direction before and after traversing the toroid allows determination of its momentum and the presence of the additional material outside the calorimeter makes it extremely unlikely that any particles other than muons will reach the outer layers of drift tubes.

The muon system consists of 5 separate solid iron toroidal magnets, with three layers of proportional drift tube chambers (PDTs) surrounding these toroids for measuring the track coordinates. The purpose of this system is the determination of the muon trajectories and the momenta, which is done by measuring the muon's trajectory before and after it passes through the magnetized iron toroid. The 5 magnets are : a magnet in the central region called CF (Central Fe) covering $|\eta| \leq 1.0$, two magnets in the end regions called EF (End Fe) covering $1.0 < |\eta| \leq 2.5$ and the two magnets in the Small Angle Muon System (SAMUS) covering $2.5 < |\eta| \leq 3.5$. The CF and the two EFs together are known as the Wide Angle Muon System (WAMUS). Both the WAMUS and SAMUS chambers are deployed in three

layers. The inner and the two outer layers are referred to as A, B and C layers respectively. Layer A is before the iron toroids and the B and C layers are after the magnets. The air gap between the B and C layers varies from 1 to 3 m. Associated with these magnets are several layers of proportional drift tube chambers (see Figure 4.8). There are some gaps (missing PDT layers) underneath the detector to provide support elements for the calorimeter and give access to the detector.

The muon system is quite thick as shown in Figure 4.9. The variation of the detector thickness, in terms of nuclear interaction lengths, as a function of polar angle clearly indicates the amount of material present before a muon enters the muon toroids. This helps in reducing the hadronic punchthrough background and provides us with a clean muon identification environment. This allows muons to be identified in the middle of hadron jets with much greater purity than electron can be. The muons should have at least a minimum energy of 3.5 GeV to reach the muon system in the central region *i.e.* at $\eta = 0$. This minimum energy becomes about 5 GeV at larger η as the muon has to go through more material in the calorimeter. For detailed discussion of the muon system refer to [26, 27, 28]. For the parameters details of all the basic components of DØ detector refer to [29].

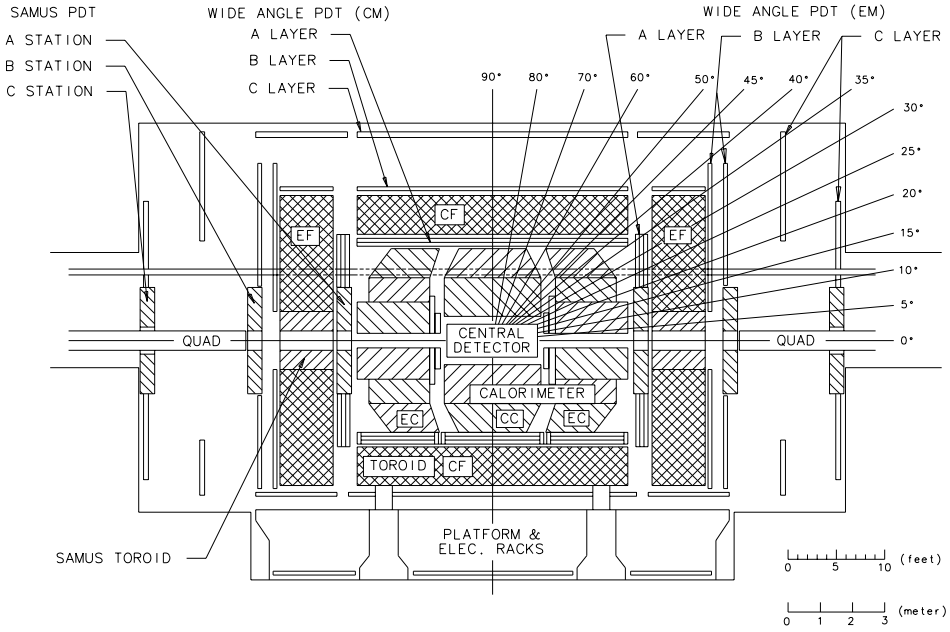

Figure 4.8: Elevation view of the DØ detector showing the muon system.

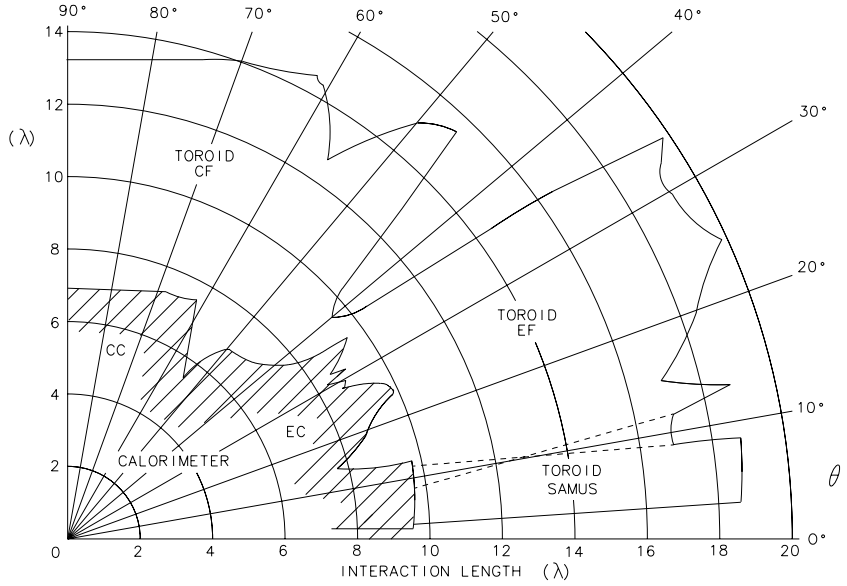

Figure 4.9: Detector thickness (in interaction length) as a function of polar angle.

4.5 Detector Operation

Proton and antiproton beams are typically kept circulating the Tevatron for about 20 hrs, during which the detector is active and recording data. As the beams circulate, they gradually dissipate, resulting in lower luminosity at the collision point. This change in running conditions means that a set of prescale factors which is optimized for the beginning of a store will be unable to fill the available bandwidth near the end of the store. In order to maintain optimal throughout, data taking is periodically paused to allow the downloading of a set of prescale factors optimized for the current luminosity.

The time in which a given prescale set is in place and the detector is running continuously is referred to as a *run*. For events which pass Level 2 trigger (Sec. 6.1) are numbered sequentially within each run meaning that an event is labeled uniquely by its run and event number.

Chapter 5

Fabrication of Pixel Scintillation Counters

During my research work, besides studying the different "non-conventional" methods to determine the top quark mass, I have contributed in the fabrication of pixel scintillation counters along with the group at Panjab University (PU). Our group and Delhi University group were assigned to build about 120 Pixel Scintillation Counters. These counters were supposed to be used in forward muon detectors in the muon system. This chapter provides a brief description of DØ upgrade, the steps involved in the fabrication of pixel scintillation counters and their testing at PU.

5.1 DØ Upgrade

The DØ detector has proved to be an excellent instrument to check the consistency of the Standard Model. Its finely segmented calorimeter and large angular coverage for electron and muon identification and measurement have enabled a wide range of physics studies.

The goal of DØ upgrade is to exploit fully the physics potential of the Tevatron Collider in the high luminosity Main Injector environment. An integrated luminosity of 2 fb^{-1} accumulated at upto 2×10^{32} $cm^{-2}s^{-1}$ is accompanied by a reduction in a bunch spacing. This factor of 10 increase in integrated luminosity over previous run will provide an opportunity for significant improvement sweeping the wide range of physics studied at the DØ experiment. The upgrade will significantly enhance the capabilities of the detector :

- b-quark decays will be tagged using displaced vertices in the silicon tracker.
- Muon identification and triggering will be enhanced, especially at low p_T.
- Electron identification and triggering will be improved using preshower detectors and magnetic central tracking and electron charge will be determined.

With an integrated luminosity of 2 fb^{-1}, the detector will be capable of :

- Precise studies of large statistics samples of the top quark including single-top production.
- Precision electroweak measurements including the mass of the W and $\sin^2\theta$ for light quarks and studies of multi-boson production.
- Measurements of QCD processes with large statistics in new regions of phase space and with new probes ($W/Z/\gamma + jets$) as pioneered by DØ in Run I.
- A well-focused B-physics program including CP violation in the $B \to J/\psi K_s^0$ system, B_s mixing, heavy quark spectroscopy and rare decays.
- Powerful searches for physics beyond the Standard Model.

Capability to identify and trigger on muons is one of the key features necessary to exploit these possibilities. The upgraded DØ muon system features full coverage for $|\eta| < 2$. The physics motivation for going to the higher luminosities are the studies of low cross-sections, high p_T processes, such as top and W/Z, and search for new phenomena. In order to maximize the acceptances for muons from these processes, sufficient detector coverage is required.

The three layers of the muon system are designated as A, B and C. Layer A is closest to the interaction region, and the toroid magnet is located between the layers A and B. For $|\eta| \leq 1$, the WAMUS PDTs have been retained but the electronics, from the front-ends of the Movable Counting House (MCH), have been replaced. The primary reason for this change is the aging of the WAMUS PDTs. The chambers suffer from a radiation induced buildup of material on the anode wires derived from the cathode pad polyresin material. Studies of the aging of the forward WAMUS chambers have already revealed that those chambers are not going to survive in Run II. A new design for the forward muon system has been developed which is called forward angle muon system (FAMUS).

The layout of the forward muon system ($1.0 < |\eta| < 2.0$) as shown in Figure 5.1 includes three layers of scintillation counters for triggering on events with muons on both sides of the detector. Forward muon system consists of the following major parts :

- 3 layers of mini drift tubes (MDTs) for muon track reconstruction.
- 3 layers of scintillation counters for triggering on events with muons.
- Shielding around the beam pipe from calorimeter to the acceleration tunnel to reduce trigger rates, fake tracks reconstruction and aging of detectors.

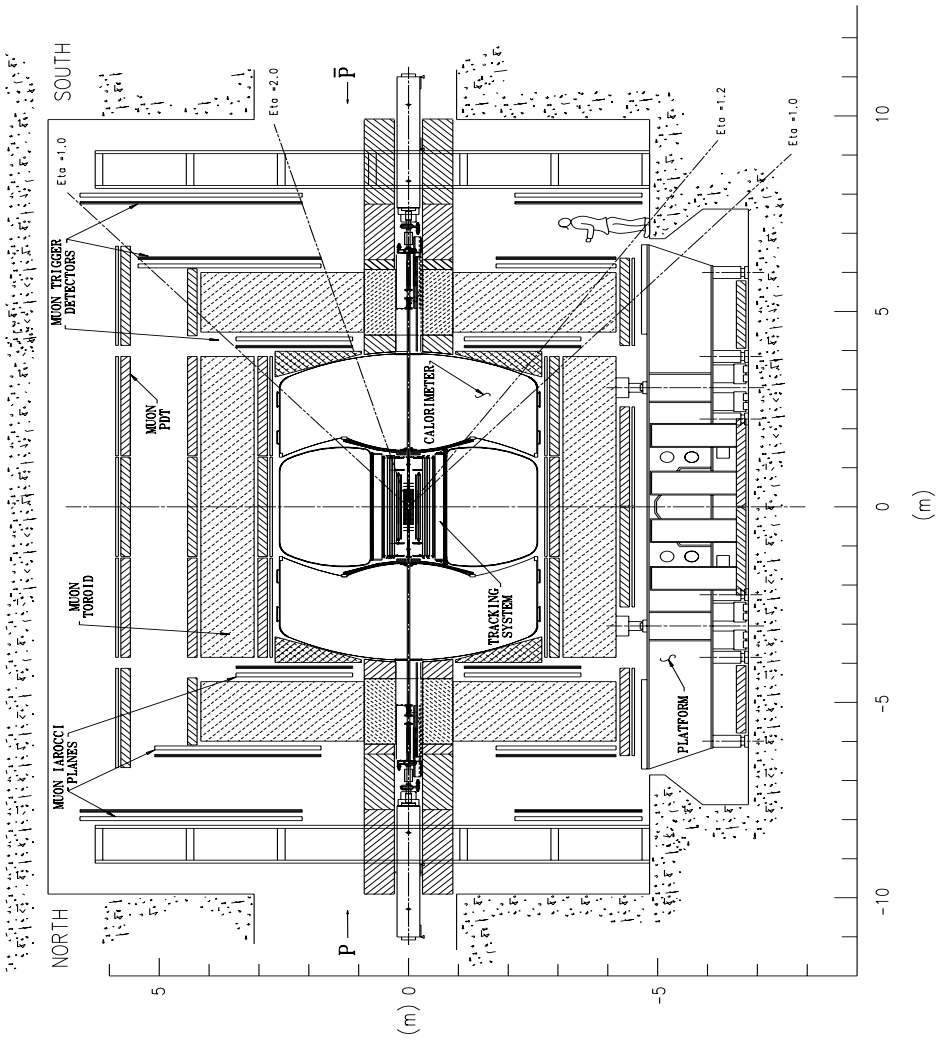

Figure 5.1: Side view of the DØ upgrade detector with major upgrade detector system indicated.

As already mentioned, there will be 3 layers (A, B and C) of scintillation counters on each side of the detector, A - closest to interaction region, then B, and C is the most distant from the detector center. Three layers of forward muon scintillation counters (FMSC A, B, C layers) are arranged in a projective $(r-\phi)$ geometry for uniform coverage in η and ϕ with $\triangle\eta = 0.1$ and $\triangle\phi = 4.5^{o}$ segmentation. The ϕ segmentation of 4.5^{o} matches track candidates from fiber tracker trigger (CFT) sectors. The η segmentation of the first nine rows of counters is 0.12 and for the last three it is 0.07. The selected segmentation was optimized to keep total number of counters per octant (1/8 plane) at 96, cover the FAMUS η region, match with the MDT sensitive area and minimize counters sizes at small η. Each plane of counters is divided into 8 octants with 96 counters per octant in order to reduce the size of the mechanical units during production and testing; the C plane size is 12×12 m^2. Each octant is assembled and tested separately. Each plane of counters is mounted in the DØ detector with the support at the top of the frame and is movable along beam line in order to get access to MDT planes.

The segmentation ($\triangle\eta = 0.1$, $\triangle\phi = 4.5^{o}$) has been optimized w.r.t. multiple scattering, the fiber tracker trigger azimuthal segmentation, the minimum muon momentum, background trigger rates, and the number of channels. Such a design leads to substantially different sizes of trapezoidal counters, varying from 10×15 cm^2 to 60×106 cm^2. Advantage of scintillation trigger counters is their ability to count substantially less background hits than other types of detectors. Reduction in the gate width from 10 ns to 20 ns reduces the number of the background hits per plane by 10 times, keeping 100% efficiency of muon detection. The minimum ionizing particle (*mip*) energy deposition in 12.7 mm scintillator is 2.5 MeV. Setting a detection threshold at 0.5 MeV will reduce the counting rate due to neutrons by a factor of 3. The minimum pixel size is dictated by the requirement of triggering efficiently on muons down to $p_T = 3$ GeV, where the typical multiple scattering angle is about 3^{o}. On the other hand, fine granularity is needed in order to keep the combinatoric backgrounds under control. Since the combinatoric rejection varies as n^3 for 3 layers of n scintillator pixels in coincidence with the CFT trigger, a factor of two coarser granularity would give almost an order of magnitude increase in accidental triggers. Each plane consists of two overlapped sub-planes in order to remove any dead zones between the counters.

The total number of FMSC counters in the system is 4608. These are grouped into octants matching the MDT arrays. There are about 96 counters per octant. The forward angle muon trigger design (Figure 5.2) is optimized to provide good time resolution and uniformity of response for better background rejection and high efficiency of muon detection. The selected design of a typical counter is as shown in Figure 5.3 for counters with size 216×338 mm^2 [30]. It consists of 12.7 mm thick Bicron 404 A scintillator plate cut to trapezoidal shape with two Kumarin 30 WLS bars for light collection. The bars are 4.2 mm thick and 12.7 mm wide. These were installed along two sides of the counters and bent at 45^{o} to collect light on the phototube.

Our PU group and Delhi University group were assigned to build about 120 special counters with fibers around the scintillator. The design is as shown in Figure 5.4 (a). The main idea of this design is that the $\sim 1/6^{\text{th}}$ of total light in scintillator plate goes to each of the six side inside internal reflecting ones : the smaller is the side, the higher is the brightness of light to this side. Fibers are oriented to collect light to the small sides of the plate. Therefore, 4 out of 6 sides are covered using only 12 fibers for 12 mm thick scintillator ($\sim 4/6^{\text{th}}$ of total light goes to these fibers). Both ends of the fibers are glued to a lucid tube. This assembly is diamond cut and placed at the PMT photocathode. The length of the fiber is equal to the perimeter of the scintillator. This design is good for counters that are not very large. The advantages of this design are :

- Higher efficiency of light collection using smaller number of fibers.
- It is not necessary to cut, polish and mirror the ends of fibers opposite to the PMT.
- A smaller diameter PMT may be used.
- It is easy to place PMT on the top scintillator, the small number of fibers makes fiber assembly more flexible.

Results show that a scintillator of size $465 \times 325 \times 12.7$ mm^3 gives 54 photoelectrons on the center of with a non uniformity of $\pm 3.5\%$ with $\sigma_t = 1.0$ ns as shown in Figure 5.4 (b). The Figure 5.4 (b) shows the light yield on the center of the counter versus the number of fibers for two different size counters. There is a saturation effect for this dependence. It is clear from the figure that a counter of size $465 \times 325 \times 12.7$ mm^3 gives 54 photoelectrons and good enough timing with $\sigma_t = 1.48$ ns. The uniformity of light yield for counters with size $200 \times 200 \times 3.3$ mm^3 is shown in the Figure 5.5. Measurements using a scintillator plate with unpolished but machined sides were performed for some light collection methods. The less expensive unpolished variant is not worse (even better) than the polished one in the yield of photoelectrons and uniformity for the studied methods. For DØ upgrade please refer to [31]

Figure 5.2: The forward angle muon trigger design.

Figure 5.3: Design of the scintillation counter.

Figure 5.4: (a) Design with fibers around the counter perimeter. (b) Number of photoelectrons vs. number of fibers for design with fibers around the counters perimeter.

Figure 5.5: Uniformity of light response for counters using WLS fibers. Measurements used the radioactive source Ru^{106}.

5.2 Pixel Scintillation Counters

We fabricated 5 prototype pixel scintillation counters at PU Chandigarh. The final drawing for the scintillator is similar to as shown in Figure 5.4 (a) except that the PMT is placed width wise. The final drawings of the fabricated scintillators are given in Appendix A (A Drawings). The steps involved in the fabrication are as :

1. The scintillation counters have been fabricated using Bicron 404A scintillator[1]. The Bicron 404A scintillator was chosen because of its low cost and good performance. It is approximately a factor of two less expensive than comparable scintillators. This scintillation has a relatively short attenuation length, but this is not a problem because the light collected within a short distance by wavelength shifting fibers (WLS fibers), Bicron BCF91A WLS fibers[2].

2. The scintillator is cut into the given size. For holding of 12 WLS fibers around the scintillator, special grooves on the four corners of the scintillator have been made to avoid breaking of fibers at the corners. These grooves are made on both sides of the scintillator so that in each groove 6 fibers could be inserted. The scintillator was machined with 1 mm wide and 6 mm deep wide round grooves on one side. The grooves are rounded to a radius of 39.5 mm and 44.5 mm respectively. There are total of 8 grooves. The machining was done using computer controlled CNC machine at Central Tool Room Ludhiana (CTRL).

3. Since 12 WLS fibers are used for the collection of light, a special plastic cookie is designed to make a bunch of 24 fibers (12×2) fibers. 24 fibers are inserted into this cookie and these fibers are held in place with Bicron 600 optical epoxy[3]. The fibers are rough cut with a saw and then the ends of cookies and the fibers are diamond polished. A special type of coupling was designed to couple cookie to the tube for passing on the collected light to the PMT. This coupling is fixed on the top cover with the help of a clamp of diameter 42.0 mm. A special cookie cover is designed to cover the cookie and make it light tight.

4. The counters are then wrapped with a tyvek sheet (a plastic insulating material) with a hole cut for the fibers and cookies. It is used because it improves the counter response by about 10% which results in the better collection of light. This is further covered with a black tydler paper to avoid any interference of external light.

5. In order to provide the support for the counter, a special aluminium channel frame has been designed, fabricated and placed over the aluminium sheets

[1]Type BC404A scintillator, Bicron Corporation 12345 Kinsman Rd, Newbury, OH 44065-967.
[2]Type BCF91A wavelengthshifter fiber, Bicron Corporation, 12345 Kinsman Rd, Newbury, OH 44065-9677.
[3]BC-600 Optical Epoxy, Bicron Corporation, 12345 Kinsman Rd, Newbury, OH 44065-9677.

around the edges and bolted together. Special notches (total 8 notches) have been made on each cover which are ultimately used for holding of the aluminium channel around the counter.

6. The counters have metal clamps attached at the center for additional support.

7. To fix this cookie cover on to the top cover, rectangular spacer was designed. For the compensation of clamp used for holding of cookie, cylindrical spacers of diameter 10.0 mm and height 11.5 mm are used.

8. For the collection of light, Green extended phototube 115M from MELZ have been used. These tubes were procured along with the voltage divider (RC network) and a metallic light tight housing, which is coupled to the cookie with the help of coupling already described. The clamp of diameter 48.0 mm and cylindrical spacer arrangement was used to hold the PMT housing on the top cover.

9. Two thick aluminium sheets were made to cover the top and bottom surface of the scintillator.

The dimensions of the final counter as well as the material to be used were finalized at Fermilab and passed on to us for the final fabrication of these counters. The total set of drawings were designed and developed in the department during the tenure of my work and got approved from Fermilab, USA before final fabrication was carried out in the department. The drawings Figures A.1 - A.14 having the complete design of the scintillator counters are given in Appendix A. The pixel counter assembly was designed and developed at the PU, Chandigarh. A total of 5 pixel counters were fabricated. Mechanical fabrication work was done at the department as well as in the Central Tool Room Ludhiana (CTRL). For scintillation counters refer to [32].

5.3 Cosmic Ray Setup

To measure the efficiency of the counters, the counters were put to Cosmic Ray muons for testing on data acquisition setup (DAQ). The block diagram of Cosmic Ray setup at Panjab University, is shown in Figure 5.6.

Cosmic rays are produced in the collision of extra terrestrial particles with nuclei in the earth's upper atmosphere. These are very high energy particles, mainly protons, from outer space. When they enter earth's atmosphere they interact with the nuclei of the atmospheric gas molecules. One of the products of these reactions is a particle called muon. Muons are formed from the decay of pions, which are created in the upper atmosphere. The muons being more penetrating, manage to reach the surface of the earth without being absorbed. A muon is roughly 200 times heavier than an electron. Since muon is so heavy it is unstable and decays into an electron and two neutrinos : precisely, a muon type neutrino and an electron type antineutrino.

$$\mu^- \rightarrow e^- + \nu_e + \nu_\mu^-. \tag{5.1}$$

In DAQ, we have two master/standard paddles in which we have used EMI tubes numbered 66263 and 66268. These standard paddles are made up of plastic scintillator material which have been cut in rectangular shapes. The paddle is wrapped in a special tyvek paper to reflect back the light and further these are wrapped with black paper to avoid any interference from external light. In these, instead of fibers, the scintillator light is conducted to the PM via a light guide (or a light pipe). The light guide is made up of optical quality perspex and works on the principle of internal reflection *i.e.* light entering from one end is "guided" along the pipe by internally reflecting it back and forth between the interior walls. A round cookie of the size of the PMT has been used to pass the collected light signal on to the tube. This cookie is joined to perspex material with the help of glue.

The EMI Photomultiplier tubes (PMTs) in standard paddles have been fed with HV +1600 V. From these standard paddles, the pulse signals are fed to *discriminator*. Pulse signals are brief surges of current or voltage in which information is contained in one or more of its characteristics *e.g.* its polarity, amplitude, shape etc. This mode of coding is natural in nuclear and particle physics as most of the modern particle detectors are pulse devices. The amplitude or the pulse height is the height of the pulse as measured from its maximum value to the instantaneous baseline below the peak whereas the voltage or current level to which the pulse decays is called the baseline of the signal.

The discriminator is a device which responds only to input signals with a pulse height greater than a certain threshold value. The value of the threshold has been adjusted with the help of a screw on the front panel. An adjustment of the width of the logic signal is done via similar controls. The discriminator also blocks out low amplitude noise pulses from PMTs or other detectors. Good pulses, which should in principle be large enough to trigger the discriminator, are then transformed into logic pulses for further processing.

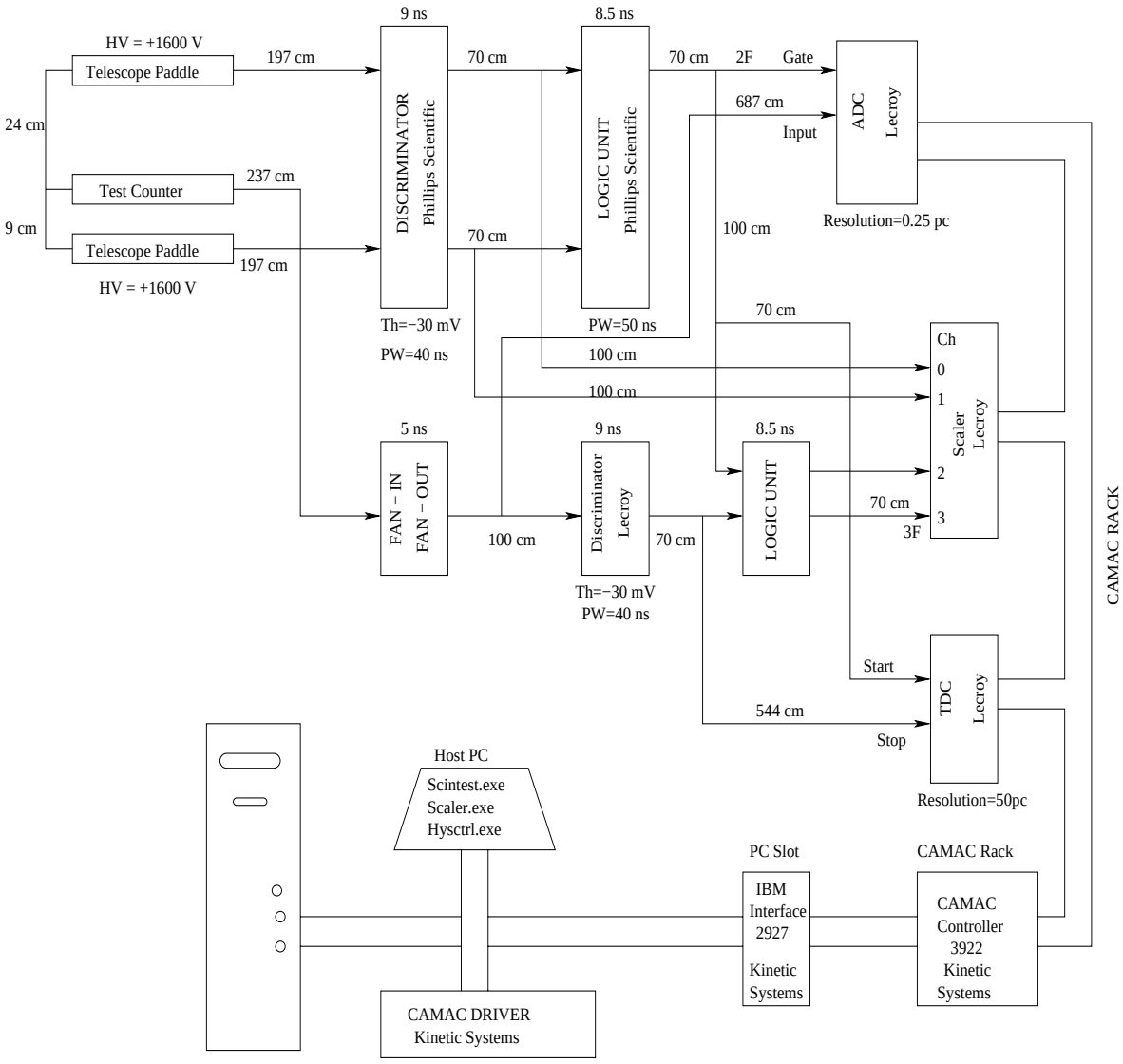

Figure 5.6: Cosmic ray test setup at Panjab University.

The logic or digital signal may only take on discrete number of states *i.e.* the information is of quantized nature. Although the logic signal carries less information than the analog signal, from a technical point of view it is more reliable since the exact amplitude or form of the signal need not be perfectly preserved. Indeed, distortion or noise, which are always present in any circuit will easily alter the information in an analog signal but would have much less effect on the determination of what state a logic signal is in. If the pulse height of the input signal is greater than a given threshold, the discriminator responds by issuing a standard logic signal; if not, no response is made. Figure 5.7 below shows the discrimination operation *i.e.* only signals whose amplitude is greater than the fixed threshold trigger an output signal which is a logic (digital) signal.

Figure 5.7: Discriminator operation : only signals whose amplitude is greater than the fixed threshold trigger an output signal.

The noise is in the range 15-25 mV in the PMTs which we have used. This noise (or distortion) in our circuit setup can result from number of reasons. But the most important sources causing the fluctuation are the presence of

i) dark currents.

ii) statistical noise-in-signal effects.

The dark current is the small current which flows even when a PMT is not illuminated. It arises from several sources :

i) Thermionic emission from the cathode and dynodes : It is the principal component.

ii) Leakage currents : Leakage currents going through the electrode supports and the pins at the base also contribute a large component to the dark current. By lowering the breakdown voltage, leakage current through the pins is reduced.

iii) Radioactive contamination : Radioactive materials in the glass housing or support materials can also cause electron emission from the photocathode or dynodes. The radiation from these contaminants can either directly strike the electrodes or cause fluorescence in the glass housing itself. In each case, a small current results.

iv) Ionization phenomena : Residual gases left or formed in the PM also cause a detectable current. These gas atoms can be ionized by the electrons and since they are of the opposite charge, will accelerate back towards the cathode or dynodes where they can release further electrons. This results in afterpulses occurring in a time equal to the time needed for the ions to transit the tube.

v) Light phenomena : Under high current, the afterpulses may also be caused by electrode glow *i.e.* light emitted by the last few dynodes which travels to the photocathode.

Statistical noise is a direct result of the statistical nature of the photoemission and secondary emission processes. For a constant intensity of light, the number of photoelectrons emitted as well as the number of secondary electrons emitted will fluctuate with time. The current at the anode will thus fluctuate. Statistical fluctuations in a PMT have two origins : photocathode and electron multiplier system. The first source arises from the statistical nature of the photoelectric effect and the second source arises not only from the statistical nature of secondary emission, but from differences in electron transit times, non-uniformities in the secondary emission factor over the dynodes.

We have set the threshold value to be -30 mV (because signal is negative) and pulse width to be 40 ns. The adjustment of threshold at this value rejects the noise and as a result we get a clear output signal in the form of logic signal. These logic

signals are then fed on to the discriminator. Discriminator used by us is capable of handling 8-16 input signals independently. Each input has independent output so that we get independent logic output signal. These signals are then fed to logic unit where signals sum up and give us one signal output *i.e.* 2-Fold (2F) output. This 2F output is formed only when signal *i.e.* muon signal is accepted by both the paddles which become gate to ADC. Each fabricated pixel scintillation counter has been tested by placing it in between the two master paddles. The counters have been tested using phototubes 115M from MELZ (Moscow, Russia) which is fed with a negative voltage. The signal from the test counter goes to *fan-in fan-out*. Fan-outs are active circuits which allow the distributions of one signal to several parts of an electronic system by dividing the input signal into several identical signals of the same height and shape. Whereas, the fan-in accepts several input signals and delivers the algebraic sum at the output. These are particularly useful for summing the outputs of several detectors or the signals from a large detector with many PMTs. These modules may be bipolar *i.e.* accepting signals of both polarities or the single polarity. The counter signal directly goes to the input of the ADC; a device which converts the information contained in an analog signal to an equivalent digital form. ADC is the fundamental link between analog and the digital electronics. ADC gives the data-way to computer automated measurement and control standard (CAMAC) which is further fed onto the computer by CAMAC controller and interface. Along with 2F output, the signal from test counter passing through discriminator is fed to logic unit where it sums up and we get single 3F output. This is formed only if the signal passed through two master paddles is also passed through test counter. In the data acquisition setup, we have a scaler; a unit which counts the number of pulses fed into its input and presents this information on a visual display. Their contents may be read by a computer or fed into a separate display unit. We have used four inputs of the scaler for the whole setup.

Channel 0 : Counts of Paddle 1
Channel 1 : Counts of Paddle 2
Channel 2 : Counts of 2-Fold (2F)
Channel 3 : Counts of 3-Fold (3F)

This scaler is helpful in knowing about the efficiency (ratio of counts taken by 3F to counts taken by 2F) for the counters. We have used a software program (PUDAQ) which gives the direct display of counts counted by scaler. Using this DAQ setup the pixel counters have been tested for their efficiencies. These counters were found to be extremely satisfactory. For the description of various components of DAQ refer to [33].

Results

- The optimum voltage for about 10 PMTs have been determined. PMTs numbered 18971 (2200 V), 3427 (2200 V), 17118 (2150 V) and 6200 (2250 V) are efficient ones. The values in the parentheses indicate the optimum voltage

for the respective PMT. Table 5.1 shows the efficiency for PMT no. 18971 at different voltages for time duration of 5 mins. Optimum voltage for PMT 18971 is 2200 V. At 2300 V efficiency is more but at this value noise in the pulse is too high. At each voltage counts have been counted for all the four channels *i.e.* Channel 0, 1, 2 and 3.

- The efficiencies of the pixel scintillation counters fabricated at PU are as shown in Table 5.2.

5.4 Fiber Testing for the Muon Scintillator

For the collection of light in scintillators, wavelength shifting fibers (WLS fibers) have been used. Using WLS fibers, one can concentrate the light from the scintillator to the smaller cross-section of fibers and to smaller photocathode area. We were involved in the job to test the light output from these fibers with one end fixed near a photodiode and the other end being treated with various reflecting materials. The fibers have been tested with the far ends being sputtered with A1, diamond cut, diamond cut with A1 mylar type or fine razor cut and checked for light output. Each fiber before being used was tested with Computer Controlled Fiber Scanner Machine here at PU. Each and every batch of fiber used in the scintillation counter has been tested by our group and the best ones were used for the counter.

The block diagram of Computer Controlled Fiber Scanner machine which has been used to check the attenuation in the WLS fiber and clear fiber is shown in Figure 5.8. It shows the basic components of this machine. The Stepper Motor (SM) drives the pulley. In fiber scanning machine, two pulleys of 124 mm diameter and having 28 teeth were chosen to drive a timing belt of the width 20 mm and 14 mm pitch. The teeth of the pulley match with the teeth of belt. One pulley is used as driver and the other is driven. The driver pulley is driven by SM. The pulleys are mounted vertically on metal brackets and fine ball bearings are used for smooth movement. These two pulleys have belt around them and on the belt UV source holder is clamped. The movement of pulley drives the belt and the lamp moves as the belt moves. Motor wires are connected to driver and control circuit (motor driver card) and also to 12V/5Amp Power Supply unit. A UV lamp is used as input light source (pencil shape) to fiber to study the fiber's attenuation length and light emission across the spliced region of WLS fiber and clear fiber. UV lamp procured from M/S Oriel Instruments is mounted on the lamp holder. The lamp is further linked to the special power supply provided by the same firm. Two tube rods of length 2.2 m and 3/4″ diameter are being used as guide to help the light source to slide. Two L-shaped brackets are used to hold the tubes at a height of 170 cm and the distance between the two is kept 60 mm. The source holder is made in such a way that it slides on the tubes. So the UV source mounted on the source holder moves along the length of the belt. The light source moves continuously across the length of the fiber by the SM driven mechanical system.

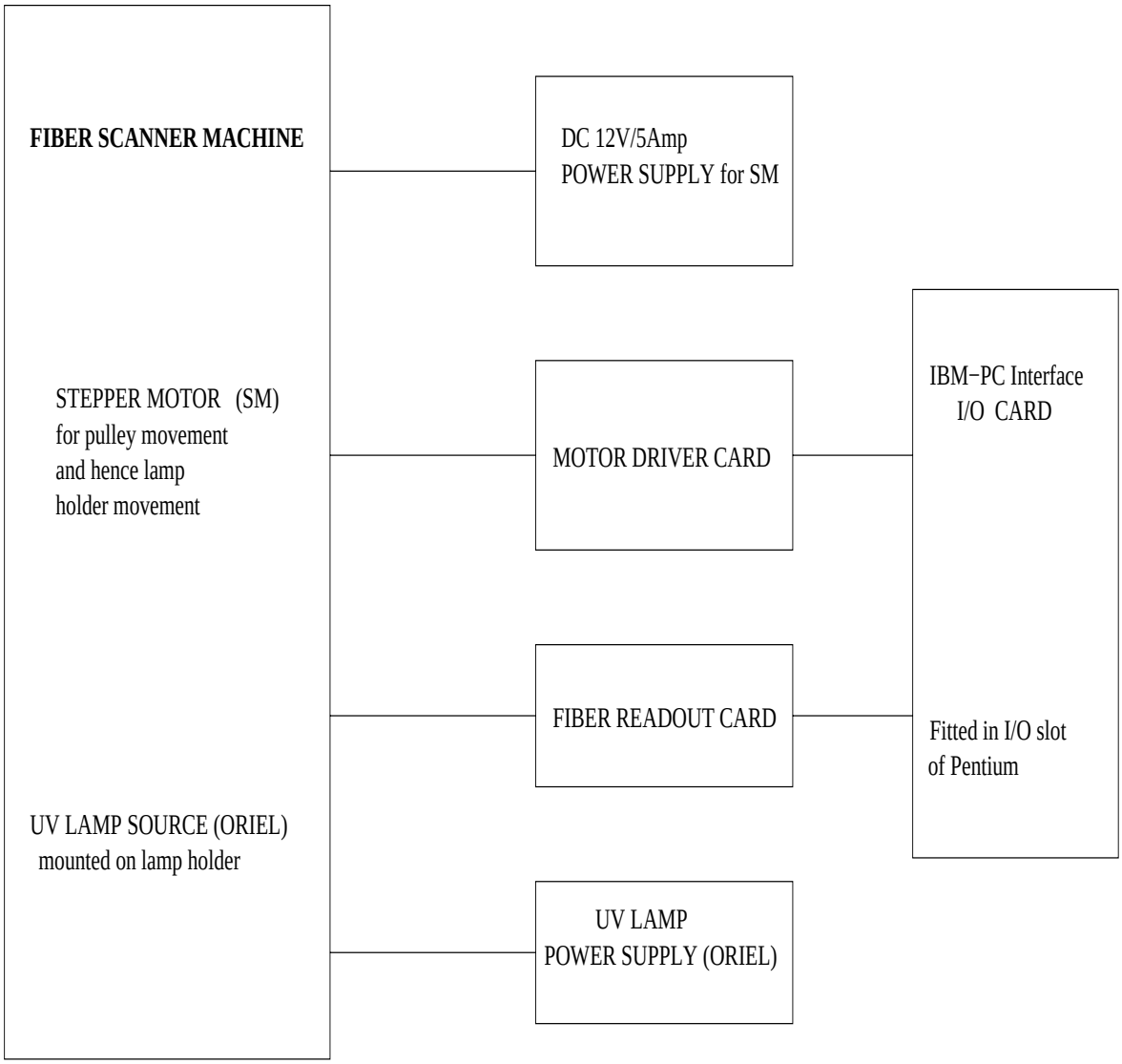

Figure 5.8: Block diagram of fiber scanner machine at Panjab University.

The output light from the fiber falls directly on the photodiodes and further the output is registered on the computer. The whole assembly is in a light tight black box so that there is no interference of external light. Finally, we get the output signal voltage as a function of distance of the source from fiber end from which the attenuation has been checked. Each end of the fiber was epoxied with one inch long ferrule whose face was machined accurately to obtain smooth face perpendicular to the fiber axis. One ferrule was coupled to the photodiode with the optical grease. The intensity pattern is represented by the sum of two exponentials of the form

$$I(x) = A1 \times exp(-x/\alpha_1) + A2 \times exp(-x/\alpha_2), \tag{5.2}$$

where $A1$, $A2$, α_1 and α_2 are the fitted parameters [34].

The far end of the fiber with the ferrule was coupled to various reflecting materials for analysis. The best results for maximum light output were with sputtered fibers at the far end, having 25% more light output than fine razor cut fibers. The light output of diamond cut fibers with A1 mylar type at the far end was the second best choice. For the final counters, we have used the diamond cut fibers with anodized aluminium strip at the end. One metallic platform was made to hold 16 fibers at time and was mounted on the machine at a height, so that the distance between the UV source and fiber is kept close and constant. A special mechanical arrangement was made to hold the motor which was mounted with gears of ratio 1:4 which drives the pulley. Nylon gears were used which helped in absorbing the vibrations due to SM. These gears do not require any oil. These brackets were mounted on an iron channel and the whole assembly was installed in a light tight box.

Results

- The fitted intensity pattern for one of the fiber is as shown in Figure 5.9. It shows that the intensity pattern is represented by the sum of two exponentials as given in Eqn. 5.2. The fibers tested at PU have also been tested on fiber scanner machine at Tata Institute of Fundamental Research (TIFR) and the comparison is shown in Figure 5.10. It shows that the PU fiber testing results are comparable to TIFR fiber testing results.

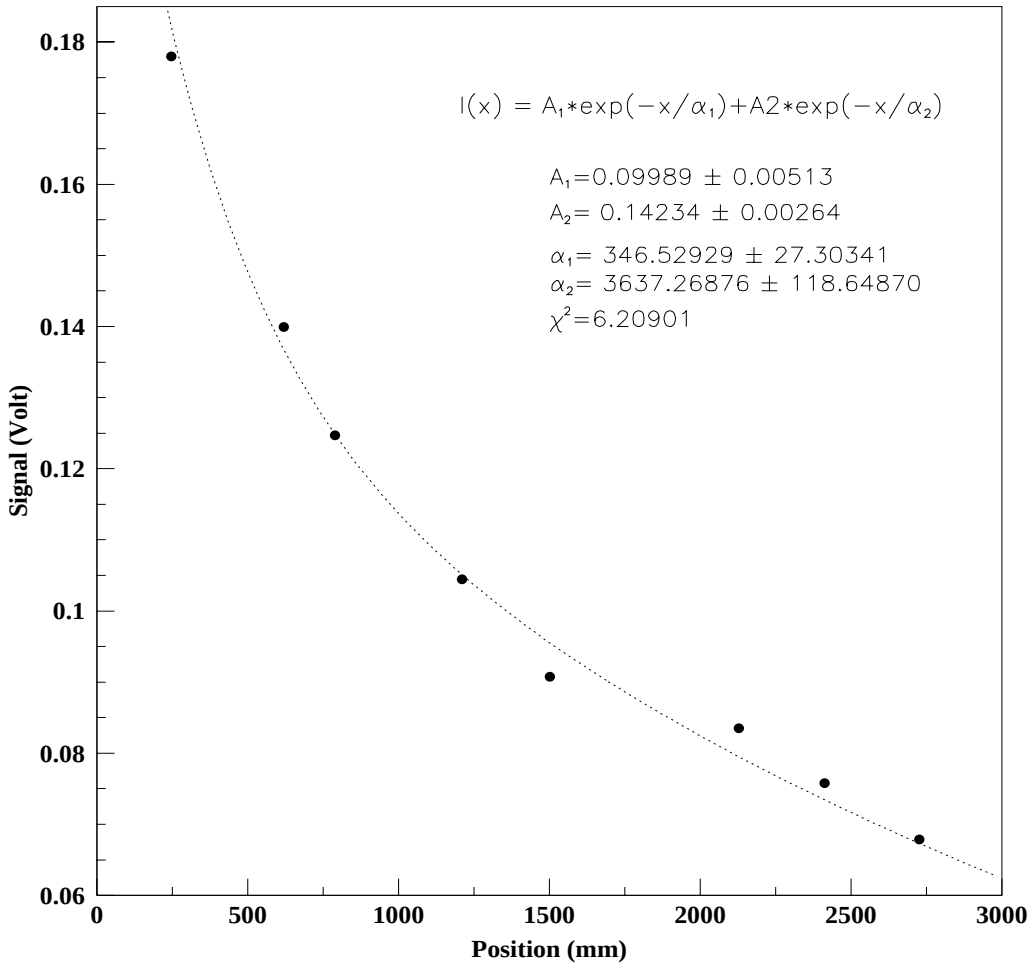

Figure 5.9: Fitted intensity pattern for one of the tested fiber. Fitting has been done by the sum of two exponentials as given in Eqn. 5.2.

Figure 5.10: Comparison of one of the fiber tested at PU, Chandigarh and TIFR, Mumbai.

Chapter 6

Triggering and Monte Carlo Simulations

In our analyses for determining the top quark mass by alternate methods, we have used the data taken by DØ detector in three separate runs (Run Ia, Run Ib and Run Ic), collectively called Run I (1992-1996) of DØ detector. Before we can use this data for our analyses, it undergoes many steps like triggering. In this chapter we briefly explain one of the major system of the DØ detector : trigger system. It reduces the number of unwanted events with the help of another system called data acquisition (DAQ) system. This chapter also explains the Monte Carlo (MC) simulations which are the techniques used to model the signal and backgrounds for optimizing the selection cuts.

6.1 Trigger System

During data taking in Run I, at a luminosity of 5×10^{30} cm^{-2}s^{-1}, the proton and antiproton beams cross each other at the rate of 290 kHz and at the operating luminosity of the Tevatron, nearly all of these crossings produce at least one $p\bar{p}$ collision. Since it is not feasible to record all of the interactions, a filtering system, known as the trigger system has been implemented to select events relevant to the physics analyses at DØ. The DØ trigger system is composed of three hardware stages (Level Ø, Level 1 and Level 1.5) and one software stage (Level 2).

Level Ø

The Level Ø (LØ) is a scintillator based trigger designed for fast vertex position measurement and to indicate the occurrence of inelastic collisions. The LØ trigger consists of two hodoscopes mounted on the front surface of the EC cryostats. The hodoscopes contain two sets of scintillation counters arranged in planes perpendicular to the beam and rotated 90^o w.r.t. each other. Since inelastic collisions cause a significant activity in the forward regions, the coincidence of the signals from two scintillator arrays is attributed to inelastic collisions. Moreover, the interaction

vertex is determined with a resolution of ± 15 cm, by comparing the arrival times of the signals from two scintillator arrays. The hodoscopes give a partial coverage for $1.9 < |\eta| < 4.3$ and $2.2 < |\eta| < 3.9$ for an almost complete coverage.

In addition to its role as primary trigger, the LØ system also serves as the luminosity monitor for the experiment. The instantaneous luminosity is approximately given by measuring the rate $R_{L\emptyset}$ of LØ trigger.

$$\mathcal{L}_{inst} = \frac{R_{L\emptyset}}{\sigma_{L\emptyset}} \tag{6.1}$$

where $\sigma_{L\emptyset}$ is the world average $p\bar{p}$ inelastic cross-section, corrected for the LØ acceptances and efficiencies measured from MC and data. This stage is typically used as an input to L1, but LØ is not required to fire before an event can proceed to the next stage.

Level 1 and Level 1.5

The Level 1 (L1) "Trigger Framework" processes digital signal from LØ, the calorimeter, the muon system, the TRD and timing signals from the accelerator and the host computer. The L1 trigger decides within 3.5 μs (bunch crossing time) whether an event should be kept or not. These pieces of information are stored in a 32-bit logical trigger word. Each of these bits is a logical combination of 256 programmable AND-OR input terms. Events with at least one non-zero trigger bit are accepted (the $e\mu$ analysis requires an OR of three of these trigger bits). When a prescale N is assigned to a trigger, the trigger bit is fired every once in N-times that events satisfy the trigger condition. Others such as the muon trigger require several bunch crossing times to complete and are referred to as Level 1.5 (L1.5) triggers. The rate of successful L1 triggers is about 200 Hz.

The L1.5 improves energy resolution by examining the energy in towers neighboring the L1 calorimeter EM tower. Additionally, energy sums are computed from adjacent hadronic towers, and the ratio $E_{\rm EM}/E$ is used for further background rejection. The rate is further reduced to 100 Hz using L1.5 trigger.

Level 2

Once an event passes L1, it is transferred to Level 2 (L2) system. L2 is a software trigger system which uses the digitized information from an event to perform a fast reconstruction, allowing the application of more sophisticated criteria to the event decision. L2 trigger system consists of a farm of 50 parallel VAX nodes connected to the detector electronics and triggered by a set of 8, 32-bit high speed (40 MB/s) data cables. At this level a set of algorithm is implemented to look electromagnetic jets, hadronic jets, missing transverse energy and muons etc. As a result 128 software filters are built out of these algorithms for the specific physics analyses. Any event passing L2 must satisfy the requirements of at least one of these filters. The output event rate for the full trigger system is about 1-2 Hz.

The definitions of L1 and L2 triggers are given below in Table 6.1 for $e\mu$ events.

Name	Run	Level 1	Level 2	used by
ele-jet	Ia	1 EM tower, $E_T > 10$ GeV, $\|\eta\| < 2.6$ 2 jet towers, $E_T > 5$ GeV MRBS	1 e, $E_T > 15$ GeV $\|\eta\| < 2.5$ 2 jets ($\triangle R = 0.3$), $E_T > 10$ GeV, $\|\eta\| < 2.5$ $\not\!\!E_T{}^{cal} > 10$ GeV	$ee, e\mu, e\nu$ e +jets e+jets/μ
ele-jet-high	Ib,Ic	1 EM tower, $E_T > 12$ GeV, $\|\eta\| < 2.6$ 2 jet towers, $E_T > 5$ GeV, $\|\eta\| < 2.0$ ML	1 e, $E_T > 15$ GeV $\|\eta\| < 2.5$ 2 jets ($\triangle R = 0.3$), $E_T > 10$ GeV, $\|\eta\| < 2.5$ $\not\!\!E_T{}^{cal} > 14$ GeV	$ee, e\mu, e\nu$ e +jets e+jets/μ
ele-jet-higha	Ic	1 EM tower, $E_T > 12$ GeV, $\|\eta\| < 2.6$ 2 jet towers, $E_T > 5$ GeV, $\|\eta\| < 2.0$ 1 EX tower, $E_T > 15$ GeV ML	1 e, $E_T > 17$ GeV $\|\eta\| < 2.5$ 2 jets ($\triangle R = 0.3$), $E_T > 10$ GeV, $\|\eta\| < 2.5$ $\not\!\!E_T{}^{cal} > 14$ GeV	$ee, e\mu, e\nu$ e +jets/μ
mu-ele	Ia	1 EM tower, $E_T > 7$ GeV 1 μ, $\|\eta\| < 2.4$ MRBS	1 e, $E_T > 7$ GeV 1 μ, $p_T > 5$ GeV, $\|\eta\| < 2.4$	$e\mu$
	Ib	1 EM tower, $E_T > 7$ GeV 1 μ, $\|\eta\| < 2.4$ GC	1 e, $E_T > 7$ GeV, $\|\eta\| < 2.5$ 1 μ, $p_T > 8$ GeV, $\|\eta\| < 2.4$	$e\mu$
mu-ele-high	Ic	1 EM tower, $E_T > 10$ GeV, $\|\eta\| < 2.5$ 1 μ, $\|\eta\| < 2.4$ GC	1 e, $E_T > 10$ GeV, $\|\eta\| < 2.5$ 1 μ, $p_T > 8$ GeV, $\|\eta\| < 1.7$	$e\mu$
mu-jet-high	Ia	1 μ, $\|\eta\| < 2.4$ 1 jet tower, $E_T > 5$ GeV GB	1 μ, $p_T > 8$ GeV, $\|\eta\| < 1.7$ 1 jet ($\triangle R = 0.7$), $E_T > 15$ GeV	$e\mu, \mu\mu$ μ+jets μ+jets/μ
	Ib	1 μ, $p_T > 7$ GeV, $\|\eta\| < 1.7$ 1 jet tower, $E_T > 5$ GeV, $\|\eta\| < 2.0$ GC	1 μ, $p_T > 10$ GeV, $\|\eta\| < 1.7$, scint 1 jet ($\triangle R = 0.7$), $E_T > 15$ GeV, $\|\eta\| < 2.5$	$e\mu, \mu\mu$ μ+jets μ+jets/μ
mu-jet-cal	Ib	1 μ, $p_T > 7$ GeV, $\|\eta\| < 1.7$ 1 jet tower, $E_T > 5$ GeV, $\|\eta\| < 2.0$ GC	1 μ, $p_T > 10$ GeV, $\|\eta\| < 1.7$ cal confirm, scint 1 jet ($\triangle R = 0.7$), $E_T > 15$ GeV, $\|\eta\| < 2.5$	$\mu\mu$,μ+jets μ+jets/μ
mu-jet-cent	Ib	1 μ, $\|\eta\| < 1.0$ 1 jet tower, $E_T > 5$ GeV, $\|\eta\| < 2.0$ GC	1 μ, $p_T > 10$ GeV, $\|\eta\| < 1.0$, scint 1 jet ($\triangle R = 0.7$), $E_T > 15$ GeV, $\|\eta\| < 2.5$	$e\mu, \mu\mu$ μ+jets μ+jets/μ
	Ic	1 μ, $\|\eta\| < 1.0$ 1 jet tower, $E_T > 5$ GeV, $\|\eta\| < 2.0$ 2 jet towers, $E_T > 3$ GeV GC	1 μ, $p_T > 12$ GeV, $\|\eta\| < 1.0$, scint 1 jet ($\triangle R = 0.7$), $E_T > 15$ GeV, $\|\eta\| < 2.5$	$e\mu, \mu\mu$
mu-jet-cencal	Ib	1 μ, $\|\eta\| < 1.0$ 1 jet tower, $E_T > 5$ GeV, $\|\eta\| < 2.0$ GC	1 μ, $p_T > 10$ GeV, $\|\eta\| < 1.0$ cal confirm, scint 1 jet ($\triangle R = 0.7$), $E_T > 15$ GeV, $\|\eta\| < 2.5$	$\mu\mu$,μ+jets μ+jets/μ
	Ic	1 μ, $\|\eta\| < 1.0$ 1 jet tower, $E_T > 5$ GeV, $\|\eta\| < 2.0$ 2 jet towers, $E_T > 3$ GeV GC	1 μ, $p_T > 12$ GeV, $\|\eta\| < 1.0$ cal confirm, scint 1 jet ($\triangle R = 0.7$), $E_T > 15$ GeV, $\|\eta\| < 2.5$	$e\mu, \mu\mu$

Table 6.1: L1 and L2 triggers definitions.

Main Ring Veto Trigger

The Main Ring (MR) passes through the coarse hadronic portion of CC and EC calorimeters. It is active during the production of the antiprotons and during new beam injection into the Tevatron. Beam loss from the MR can cause spurious signals in the hadronic calorimeter and muon chambers. Typically this occurs once every 2.4 seconds when the protons are injected into the MR and 300 ms later when the beam passes through transition [28]. A timing circuit linked to the MR control system is used to set a hardware flag known as MRBS-LOSS. This is set every time the protons are injected and remains set for 400 ms until the beam has passed through transition and muon system recovers. In addition, smaller beam losses occur with every passage of the beam. These are significant only if the passage of the MR beam coincides with the $p\bar{p}$ crossing in the Tevatron. This is flagged using another bit known as the MICRO-BLANK veto which is set if a MR beam passes with $\pm$800 ns of a $p\bar{p}$ crossing. The definitions of the MR triggers used for data collection are as :

- mrbs-loss (MRBS) : The trigger is disabled for the 0.4 s after a proton bunch is injected into the MR. This vetoes events during injection and transition and allows a small recovery time for the muon and calorimeter systems. The typical deadtime for mrbs-loss veto is $\sim 17\%$.

- micro-blank (MB) : The trigger is disabled for events where MR bunches are present during the livetime of the muon system which is $\approx \pm 800$ ns centered on the $p\bar{p}$ crossing. The calorimeter livetime is somewhat longer ($\sim 2\ \mu$ s), so this is not completely efficient for vetoing events with MR energy in the calorimeter. The typical deadtime for micro-blank is $\sim 7\%$.

- max-live (ML) : The trigger is disabled during periods of overlap between MRBS and MB. This corresponds to the first few passes of newly injected beam passing through the detector.

- good-cal (GC) : The trigger is disabled during periods of overlap between MRBS and MB and during MB periods of highest intensity beam leakage. This leakage was measured by a set of scintillator arrays surrounding the MR beam-pipe upstream of the DØ detector.

- good-beam (GB) : The trigger is disabled during periods of either MRBS or MB. good-beam is the cleanest possible running condition.

6.2 Data Acquisition System

The DAQ system is interwined with the triggers. The sketch of the data acquisition system is given in the Figure 6.1.

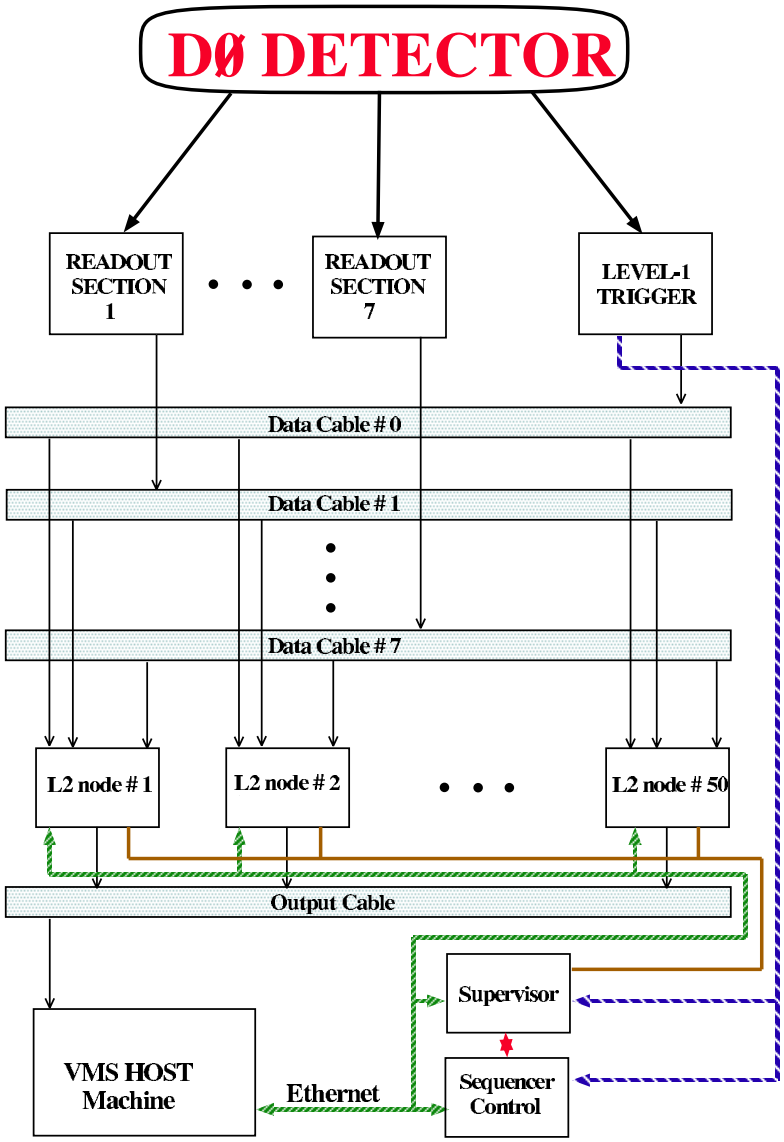

Figure 6.1: Block diagram of the Level 2 trigger and data acquisition system at DØ.

Once a L1 trigger is passed, the supervisor is notified, and it in turn notifies another processor, the sequencer, to begin digitizing the event. The sequencer signals the front-end crates to begin digitizing, which takes about 1 ms to complete. Data is then read out using eight high speed unidirectional data cables. Events passing the L2 trigger are passed on to the host computer for run-time monitoring and recording on tape. Events are buffered in the host until about 500 events have been accumulated and then the file is closed and moved to 8 mm data taking for permanent storage. The average size of an event is about 500 kbytes.

6.3 Monte Carlo Simulations

In any HEP analysis, the most important thing is the ability to distinguish between the signal and the backgrounds to that signal. The better the ability to separate out the two, better are the chances to observe a clean signal for any new process. For signal as well as backgrounds, the only way to study their details is by doing some sort of theoretical modeling process. In the field of HEP, we use Monte Carlo (MC) simulation techniques which are random number based simulation techniques. These MC simulations help us to visualize the physics processes and know the detector responses even before the actual detector is fabricated. Although the instrumental backgrounds to the $t\bar{t} \rightarrow e\mu$ channel can be estimated from data, both the signal and the physics backgrounds have to be determined using MC simulations. MC calculations consist of two steps : modeling the physics process and simulating the detector response.

6.3.1 Event Generation

The most commonly used event generators for $p\bar{p}$ collision simulations are ISAJET [35], PYTHIA [36] and HERWIG [37]. Each of these perform the following processes;

- parton-parton hard scattering
- QCD evolution
- Hadronization

6.3.2 Detector Simulation

A detector simulator is required to know the response of sophisticated detectors like DØ, for both the design and development processes. The DØ detector is based on a customized version of the CERN GEANT [38] program called DØGEANT. This encodes the DØ detector geometry and the materials through which the particles pass. It simulates in great detail the ionization in central tracking, the electromagnetic and hadronic showers in the calorimeter and the hits in the muon chambers.

The Central Processing Unit (CPU) time needed to do the full simulation of the detector is enormous and is prohibitive when trying to obtain the very large event statistics necessary for this analysis. To get around this, a package known as the "shower library" is used to simulate the calorimeter response. This is a library of GEANT shower information binned in 5 quantities which represents the kinematics of the input particle.

Following the DØGEANT simulation there are some additional corrections to be made. The first of these is the efficiency and resolution of the WAMUS chambers which are only approximated in DØGEANT. This includes corrections for effects such as misalignments and the localized inefficiencies in the muon drift tubes due to gas leaks or voltage problems. This is done using a package called MU-SMEAR [39] which smears the hit timing information to match the resolution of collider data.

Another correction is for the effects of multiple $p\bar{p}$ interactions and calorimeter noise. This is done using a package called NOISY. This requires full DØGEANT simulation and is very CPU intensive. Thus only moderate samples of events are processed through NOISY. A correction to the acceptance is then made by making a comparison between single interaction MC events and those processed through NOISY.

The DØGEANT output is in the same form as actual data and consists of the digitized signals from various parts of the detector. These can then be processed through DØ reconstruction software/package (DØRECO - refer Sec. 7.1) to simulate the reconstruction smearing of the events.

6.3.3 Signal and Background Modeling

(A) The simulations of the signal ($e\mu$ channel or $t\bar{t} \to W^+bW^-\bar{b} \to (e/\mu)\,\nu\ (e/\mu)\,\nu$) channel for this analysis was done using HERWIG version 5.7 with CTEQ3M parton distribution functions. Approximately, 100,000 $t\bar{t} \to ll$ (where, l $\to$ e, μ, or τ) events were generated for six different top quark masses (165, 170, 175, 180, 185 and 190 GeV) at center-of-mass energy of 1.8 TeV, which corresponds to Run I Tevatron energy. The events were processed through both DØGEANT and DØRECO and the signal acceptance estimated using only the events which yield a $e\mu$ final state. The values of the $t\bar{t}$ production cross-section values were taken from Laenen *et al.* [8].

The dominant physics backgrounds as explained in Sec. 2.6.2 for $t\bar{t} \to e\mu$ channel are $WW \to e\mu$ and $Z \to \tau\tau \to e\mu$ which mimic the top signal. In our analyses, we have studied these two backgrounds. These backgrounds were modeled using the ISAJET and PYTHIA generators. For $Z \to \tau\tau \to ll$, ISAJET was used and the cross-section was normalized to the DØ measured value [40]. The $WW \to ll$ was modeled using PYTHIA. The WW cross-section was normalized to the predicted NLO QCD value [41]. The feed down effects of secondary $\tau \to \mu/e$ decays have been included in both background and signal modeling.

(B) In our analyses for the determination of the top quark mass, our approach is to study "non-conventional" methods which can also be used in DØ Run II where the available statistics would be quite high and the muons will be having as good resolution as that of electrons *i.e.* because of the introduction of a central magnetic field in Run II, a significant improvement in the muon momentum measurement is anticipated. Therefore, to test this fact, we have done the MC simulations for Run II DØ detector *i.e.* for the $p\bar{p}$ collisions at center-of-mass energy ($\sqrt{s}$) of 2.0 TeV for the $e\mu$ ($p\bar{p} \rightarrow t\bar{t} \rightarrow e\mu X$) channel. As already explained, the major backgrounds for this channel are from $p\bar{p} \rightarrow Z \rightarrow \tau\tau \rightarrow e\mu$ and $p\bar{p} \rightarrow WW \rightarrow e\mu$. For this, we have simulated the $t\bar{t}$, Z and WW events at $\sqrt{s} = 2.0$ TeV using **PYTHIA** [36] program (event generator). The detector was simulated using simple software package for the Tevatron Run II SUSY/Higgs Workshop **SHW**. SHW is a fast (approximate) detector simulation toolkit designed to provide participants in the Tevatron Run II SUSY/Higgs Workshop with a simple simulation of typical DØ/CDF detector response to events generated by ISAJET or PYTHIA. It provides a standard reconstruction program for use by the members of the Fermilab SUSY/Higgs Workshop which helps in exploring the discovery reach for various new supersymmetry and Higgs related phenomena in DØ and CDF. Instead of SHW, another simulation program based on SHW, called PGS, is now available. PGS is a simple simulation package for generic collider detectors. For more details about these simulation packages please refer to [42, 43].

The alternate methods which we intend to study have been applied on both types of MC simulated samples, (A) as well as (B), *i.e.* data corresponding to 1.8 TeV energy for Run I as well as 2.0 TeV energy for Run II.

Chapter 7

Reconstruction and Identification

The signals collected from the different parts of the detector are due to the particles produced by the $p\bar{p}$ collisions. The direct information from the detector is in the raw form and is stored on magnetic tapes in the form of analog and digital signals from the various sub-systems. This raw information can not describe the kinematics of these particles. Hence, one needs to process this information into a form suitable for physics analyses by converting the raw signal into information about the various final state objects in the event. This process of turning the raw data into the kinematic parameters of the particles is known as *reconstruction*. In this chapter, we explain the reconstruction process in DØ which is carried out by a software package called DØRECO.

7.1 DØRECO

The DØRECO package is a set of software algorithms which are used to perform particle and jet reconstruction. It performs three major tasks. The very first step is *hit finding*, which involves the unpacking of the raw data and the conversion of counts into hits of definite energy and spatial location. The signals from each sense wire of the tracking chambers are converted into the spatial location of hits and the signals from each cell in the calorimeter are converted into energy deposits. The second step involves *tracking and clustering* of these hits. The hits which are close spatially are grouped together to form clusters in the calorimeter and the tracks in the tracking chambers. The final step, *particle identification*, is the step during which the tracking and calorimetric information is combined to reconstruct jets and identify electron/photon and muon candidates. The criteria applied by DØRECO in selecting these candidates are quite loose, and substantial rejection of spurious electrons and muons is gained by further offline processing. For more details about the working of DØRECO package refer to [28].

7.2 Event Vertex

The interaction point plays a major role in getting the kinematics correct. After interaction, the transverse energy and momentum of a particle is calculated as, $E_T = E\sin\theta$ and $p_T = p\sin\theta$, where θ is its polar angle in the lab frame. So, we must know θ for an emerging particle. The only information which is available for a particle being detected in the calorimeter is the location where it deposits energy. In order to get an angle from this direction, another point is needed along its trajectory. This point is fixed by finding the location of the hard $p\bar{p}$ collision from which this particle has emerged and is called the *event vertex or interaction vertex*. As the calorimeter determines the energy and the position of the particles where they hit, the position of the interaction vertex from which the particles originate is needed to find the direction of the particle. The vertex position is reconstructed with the following procedure :

- The drift chamber hits are fitted to reconstruct a track in the $(r-\phi)$ plane.
- A reconstructed $(r-z)$ track is associated with the reconstructed $(r-\phi)$ track.
- The intersection of these reconstructed space tracks with the z axis form a distribution in z. The estimated z position of the vertex is the mean of a gaussian fitted to this z intercept distribution. In the case of a z distribution with more than one peak and therefore multiple vertices, the vertex with the maximum number of tracks is considered as the primary vertex. The resolution of the vertex's z component is about 1-2 cm.

7.3 Electrons

Electrons are identified as localized deposits of energy in the electromagnetic calorimeter with a track in the central detector pointing back to the interaction vertex.

7.3.1 Reconstruction

To identify electron, the reconstruction involves following steps :

- A cluster is constructed by starting with the highest E_T electromagnetic tower and adding nearby towers to the cluster with E_T above a certain threshold using a 'nearest neighbor' algorithm [44]. The process repeats until no towers neighboring the cluster satisfy the energy requirement. A new cluster is then begun from the highest E_T tower not previously assigned to cluster.
- A cluster is required to have at least 90% of the energy in the electromagnetic calorimeter and 40% of its energy must be contained in a single tower.

- The centroid of the cluster is calculated using the cells in the third electromagnetic layer.

- If there is a track in the central detector within a solid angle of $\triangle\eta = \pm 0.1$ and $\triangle\phi = \pm 0.1$, pointing from the interaction vertex to the cluster, the cluster will be identified as an electron otherwise it is considered as a photon.

The energy resolution of electrons can be expressed by the relation :

$$\left(\frac{\sigma}{E}\right)^2 = C^2 + \frac{S^2}{E} + \frac{N^2}{E^2} \tag{7.1}$$

where E is the mean energy of the incident electron, C is a constant term due to calibration errors, S is the error due to statistical fluctuations, N corresponds to a noise term due to the contribution of electronic and radioactivity of the absorber (uranium) in the calorimeter. The energy scale of the electromagnetic calorimeter has been calibrated with reference to the mass of the Z in $Z \rightarrow e^+e^-$ events, which has been measured very accurately by the LEP experiments [45]. The measured electron energies are scaled up so that the mass peak in $Z \rightarrow e^+e^-$ matches the LEP measurement [46]. This correction is about 5% in the CC and $(1-2)\%$ in EC.

7.3.2 Identification

The procedure explained above favors efficiency rather than rejection. To discriminate electrons from other objects, we need to apply some selection cuts. One can further apply cuts according to specific analysis being carried out. The variables used are :

1. **Electromagnetic Energy Fraction**
   The electromagnetic energy fraction of a cluster is the fraction of its energy which is contained in electromagnetic calorimetry. For electrons, the electromagnetic calorimeter contains almost all of the energy, while charged hadrons will deposit only small fraction of their energy. Thus the electromagnetic energy fraction of a cluster serves as a powerful discriminant against charged hadrons.

2. **Isolation Fraction (f_{isol})**
   The electron coming from W should not be too close in space to other objects. Therefore the fraction of the energy outside a certain well defined cone should be small. DØ defines an isolation factor as :

   $$f_{isol} = \frac{E_{Total}(0.4) - E_{EM}(0.2)}{E_{EM}(0.2)} \tag{7.2}$$

   where $E_{Total}(0.4)$ is the total energy deposited in all calorimeter cells within a cone of radius $R < 0.4$ ($R = \sqrt{\triangle\eta^2 + \triangle\phi^2}$) around the electron direction.

$E_{EM}(0.2)$ is the energy deposited in the EM calorimeter within a cone of radius $R < 0.2$. The present analysis requires $f_{isol} < 0.1$ which enhances electron identification.

3. **Shower Shape**
Shower shape is one of the primary and powerful tools used for selecting the electrons and rejecting the background. Electromagnetic showers can also be characterized by the fraction of the clusters energy deposited in each layer of the calorimeter. These are correlated and are also dependent on the incident electron energy. If an electron deposits large amount of energy in the first layer then it will deposit relatively small fraction of energy in the subsequent layers and vice-versa. To obtain the discrimination against hadrons and particles jets, we can exploit these correlations. Based on test beam studies and MC simulations of electrons with energies between 10 and 150 GeV, a 41 variable covariance matrix (H-matrix χ^2) has been constructed given as :

$$\chi^2 = \sum_{i,j=1}^{41} (x_i - \bar{x}_i) H_{ij} (x_j - \bar{x}_j) \tag{7.3}$$

where x_i are the variables which define the shape. A total of 41 variables are used. These are

- The fraction of the total energy contained in the first, second and fourth layers of the electromagnetic calorimeter.
- The fraction of the total energy contained in each cell of a 6×6 array in the third electromagnetic layer.
- The logarithm of the total energy of the cluster.
- The z component of the primary vertex

A cut of $\chi^2 < 100$ is usually applied for better background rejection.

4. **Track Match Significance** (S)
A significant source to background for electrons is photons, either produced directly by the decay of π^0 or η mesons. The photons do not leave tracks in the central detector, but a track might appear if a charged particle is nearby. One can enhance the electron identification by reducing the chance of reconstructing a track for photons due to nearby charged particles. In order to quantify the accuracy with which a track points to a calorimeter cluster, S is defined as [47] :

$$S = \sqrt{\left(\frac{\triangle\phi}{\sigma_{\triangle\phi}}\right)^2 + \left(\frac{\triangle z}{\sigma_{\triangle z}}\right)^2} \tag{7.4}$$

where $\triangle\phi$ and $\triangle z$ are the azimuthal and the z axis mismatch, respectively and $\sigma_{\triangle\phi}$ and $\sigma_{\triangle z}$ are the corresponding measurement resolutions. In the case

of EC track matching, the z is replaced by the radial distance r.

5. **TRD Efficiency (ϵ_t)**
   The TRD response ϵ_t is defined as :

$$\epsilon_t(E) = \frac{\int_E^\infty \frac{\partial N}{\partial E'}(E')dE'}{\int_0^\infty \frac{\partial N}{\partial E'}(E')dE'} \tag{7.5}$$

   where E is the total energy recorded in the TRD minus that recorded in the layer with the largest signal and $\frac{\partial N}{\partial E'}$ is the energy spectrum from a sample of $W \to e\nu$ events. Since ϵ decreases as E increases, hadrons will tend to have values near unity while the distribution from electrons is roughly uniform over the allowed range of zero to one.

6. **Likelihood Ratio (L_4, L_5)**
   In order to obtain a better background rejection the DØ electron identification algorithm uses a 4 or 5 variable likelihood function. The 4 variable likelihood, L_4 uses the combinations of f_{EM}, χ^2, σ_{trk} and dE/dx and the 5 variable likelihood, L_5, uses the 4 variable from L_4 and ϵ_t.

7.4 Muons

Muons interact weakly with the matter and have long enough lifetime to pass through all of the detector material without decaying. These are identified as tracks in the muon drift chambers which point back at the interaction vertex and the reconstruction of muon tracks is similar to the reconstruction of tracks in the central detector. Similar to the central detector reconstruction, muon reconstruction involves three steps : hit sorting, track finding and global fitting. The first two steps make use of the information from the muon system only whereas the last step uses the information from the full DØ detector. They are reconstructed and identified using the hits and timing information from the muon spectrometers. Since a muon deposits a little of its energy in the calorimeter as it passes through, the resulting minimum ionizing trace can also be used for muon identification. The momentum of the muon is measured from the bend in the track produced by the magnetic field of the muon spectrometer.

7.4.1 Reconstruction

The muon reconstruction is similar to that of CDC track reconstruction except the differences in algorithm which take account of the geometry of the muon system. DØRECO uses timing information to determine the position of the hits in all the planes (A, B and C) of the muon system. For the B and C chambers, hits in four out of six possible planes are required and for the chamber A, this requirement is two out of four. The hits from the planes A, B and C chambers are then used to

form tracks. Because the B and C chambers are outside the magnetic toroid and the A chamber is inside, the tracking is done separately before and after the magnet. The segments are then matched, and a measurement of the momentum is made by measuring how much the track bends. Lastly, a global fit is performed using the tracks in the muon chamber, the interaction vertex, the energy profile in the calorimeter, and the track from the CDC/FDC. Additional corrections are made for the effects of multiple scattering in the calorimeter and the iron toroid and for the expected energy loss in the calorimeter.

7.4.2 Identification

The two major backgrounds to muon are from cosmic rays and leakage out of the backs of hadronic showers. To reduce these backgrounds, several variables are used to identify good muons which are as :

1. **Muon Track Quality (IFW4)**
   IFW4 represents the quality of a track fit. Track with perfect fits have IFW4 of 0 and those with one failure have IFW4 of 1. The IFW4 cut is a very powerful tool to reduce the cosmic rays and the fake track backgrounds constructed from random hits.

2. **Isolation ($\triangle R$ cut)**
   The analysis requires that the distance in R between the muon and the nearest jet be $\triangle R(\mu, jet) > 0.5$ and for muon and nearest electron/photon to be $\triangle R(\mu, e/\gamma) > 0.25$.

3. **Muon Track in the Calorimeter (MTC)**
   As muon passes through the calorimeter, it deposits energy through ionization, and these energy traces are used in the track fit. The fraction of all possible hadronic calorimeter layers which had energy deposits large enough to be included in the fit is recorded (MTC), along with the fraction of energy deposited in the outermost possible layer. Both of these quantities are useful in rejecting muon tracks formed from random noise in the muon system.

4. **Impact Parameters (IP)**
   Two impact parameter cuts are used to require that the muon tracks point towards the interaction vertex, and thus reject cosmic ray backgrounds.

   The *non-bend impact parameter* is defined by projecting the muon track into the xy plane (it does not get bent in this plane), extrapolating the track formed by the B and C layers towards the center of the detector, and calculating the impact parameter between this extrapolated track and the interaction vertex. The impact parameter is required to be less than 40 cm.

   The *bend-view impact parameter* is calculated by projecting the track into the plane in which the muon bends and calculating the impact parameter of this projection. This parameter is required to be less than 25 cm.

7.5 Jets

Quarks other than top and gluons which are produced in the $p\bar{p}$ collisions hadronize into colorless particles. When a quark or gluon leaves the site of a hard scattering, it can not remain free but instead *hadronizes* or *fragments* into a collection of colorless hadronic particles. This collection will typically lie in a cone around the direction of motion of the original parton and will show up in a calorimeter as a cluster of energy. This is called a *jet*.

7.5.1 Reconstruction

There are several algorithms which could be used for jet reconstruction. The most common algorithm used in the $p\bar{p}$ environment is the "cone algorithm" in which a jet is considered as the energy inside of a cone with a fixed size in $(\eta - \phi)$ space. This definition was used by UA1 [48, 49], and CDF and is also used by most DØ analyses. A jet is required to satisfy some minimum E_T threshold before it could be considered in analyses so as one of the event's objects. This threshold is 8 GeV and is needed in order to suppress random noise fluctuation which can produce small energy clusters. The main steps in the reconstruction process are :
Pre Clustering: The transverse energy is calculated for all of the calorimeter towers which are then sorted in order of decreasing E_T to form a "seed" cluster. Beginning with the highest E_T tower, clusters are formed by adding the towers within a radius R of the highest energy tower. The process is repeated for the remaining calorimeter towers.
Cone Clustering: The centroid of each cluster is calculated by performing an E_T weighted sum of the tower (η, ϕ) positions. Then the whole process is iterated using the jet centers as cluster seeds until the position of the cluster converges.
Merging and Splitting: Once the cone clustering is completed, some cells may have been assigned to more than one jet. If two jets share cells, the fraction of the total energy which is shared between them is examined. If the fraction is greater then 50%, the two jets are merged together and the jet axis is recalculated from the centroid of the cells in the merged jet. Otherwise the jets are split and the shared cell is assigned to the closest jet. At this stage all jets with transverse energy $E_T \geq 8$ GeV are retained for further analysis.

7.5.2 Identification

In order to remove any fake jets produced by calorimeter or MR noise, DØ has developed a set of quality cuts based on the jet characteristics. These are cuts on the jet ElectroMagnetic Fraction (EMF) which is used to distinguish between electrons/photons and jets, the Hot Cell Energy Fraction (HCF) which helps reduce calorimeter noise and Coarse Hadronic Energy Fraction (CHF) which helps to remove activity caused by the MR.

The various kinematic quantities defining a jet are :

$$E_T = \sqrt{E_x^2 + E_y^2} \tag{7.6}$$

where E_x, E_y are the sums of the components of the individual cell energies :

$$E_x = \sum_i E_x^i \tag{7.7}$$

$$E_y = \sum_i E_y^i \tag{7.8}$$

$$\phi = \tan^{-1}\left(\frac{E_y}{E_x}\right) \tag{7.9}$$

and

$$\theta = \cos^{-1}\left(\frac{E_z}{\sqrt{E_x^2 + E_y^2 + E_z^2}}\right) \tag{7.10}$$

7.6 Missing Transverse Energy

According to conservation of transverse momenta and the fact that the colliding proton and antiproton have nearly opposite momenta, it follows that the sum of the transverse momenta of the particles produced by $p\bar{p}$ collisions should be zero. Neutrinos do not interact in the detector and if the total transverse momentum is significantly different from zero, the difference is attributed to neutrinos. And this imbalance in the transverse energy is known as "missing E_T" and is denoted as $\not\!\!E_T$.

In order to calculate the transverse energy of the neutrinos, a vector $\vec{E}_T$ is assigned to each calorimeter cell, including the Intercryostat Detector (ICD), whose magnitude is the measured energy in the cell and it points from the interaction vertex to the center of the cell. The calorimeter missing energy is defined as :

$$\vec{\not\!\!E}_T^{\,cal} = -\sum_i \vec{E}_T^i \tag{7.11}$$

and its magnitude is given as :

$$\not\!\!E_T^{\,cal} = \sqrt{(\not\!\!E_T^{\,cal})_x^2 + (\not\!\!E_T^{\,cal})_y^2} \tag{7.12}$$

The muons deposit small portion of their energy in the calorimeter, so the transverse momenta of all good muon tracks should be subtracted from $\not\!\!E_T^{\,cal}$ to get the total transverse missing energy. Therefore,

$$(\not\!\!E_T)_x = (\not\!\!E_T^{\,cal})_x - \sum_i p_x^{\mu_i} \tag{7.13}$$

$$(\not\!\!E_T)_y = (\not\!\!E_T{}^{cal})_y - \sum_i p_y^{\mu_i} \tag{7.14}$$

$$\not\!\!E_T = \sqrt{(\not\!\!E_T)_x^2 + (\not\!\!E_T)_y^2} \tag{7.15}$$

Since all the objects in the calorimeter contribute to $\not\!\!E_T{}^{cal}$, any mismeasurement in the energy of these objects would cause a mismeasurement in $\not\!\!E_T{}^{cal}$. Therefore whenever corrections are applied to the calorimeter objects like electron and jets, the corresponding correction must be applied to $\not\!\!E_T{}^{cal}$ [50].

Chapter 8

Data Handling and Analysis Techniques

In this chapter, we discuss the steps involved in getting all the input efficiency numbers and the raw acceptances for both signal and backgrounds. From these, the expected number of signal ($t\bar{t} \to e\mu$) and background events have been estimated. We also discuss the analysis techniques : method of neural networks and the method of four vectors for the determination of the top quark mass.

8.1 Preliminary Data Reduction

The experimental signatures of the $t\bar{t} \to e\mu$ dilepton events consist of a high transverse energy electron and muon, two or more jets and a significant amount of missing transverse energy. The L1 and L2 triggers used for the data collection for $t\bar{t} \to e\mu$ channel are direct reflection of this and is summarized below in Table 8.1 for each separate run.

Run	Triggers
Run Ia	mu-ele OR ele-jet-high OR mu-jet-high
Run Ib	mu-ele OR ele-jet-high OR mu-jet-high OR mu-jet-cent
Run Ic	mu-ele-high OR ele-jet-high OR mu-jet-cencal OR mu-jet-cent

Table 8.1: Triggers for Run I of DØ detector for $e\mu$ events.

The definitions of trigger terms used above are given in Table 6.1 (Sec. 6.1). In addition to these, events collected during MRBS-LOSS and MICRO-BLANK gates were rejected in the subsequent off-line analysis.

The initial offline selection utilized the complete set of Run I μdsts. After selection demanding the above triggers, the data were filtered by requiring at least one PELC/PPHO candidate with $E_T^{em} \geq 10$ GeV, $|\eta_{em}| \leq 3.3$ and at least one PMUO

candidate with $p_T^{\mu} \geq 7$ GeV/c, $|\eta_{\mu}| \leq 2.5$. PMUO/PELC/PPHO[1] are the DØ object identification bank names. In addition, the PELC/PPHO candidates were required to have $\chi^2 \leq 300$ and $f_{isol} \leq 0.3$. The resulting files were then processed through the top_dilep package [51] where CAFIX 5.0 was used to apply the final data calibrations [52]. The corrected data were then written to disk in the form of column wise PAW [53] ntuples files. During this stage any events from runs with known detector problems were removed using the standard Run I bad run list [29].

8.2 Particle Selection and Detection Efficiencies

Besides knowing the types of the backgrounds involved with the $t\bar{t}$ signal in the $e\mu$ channel, it is necessary to estimate how much each of such a background would contribute to give a number of background events as well as the number of signal events expected from the total integrated luminosity. For this, one needs to understand all the efficiencies associated with the detector.

The input efficiencies tell us how well the detector can identify the decay objects *i.e.* electron and muon coming from the $t\bar{t}$ system. All the estimates for the top signal and the backgrounds are based on the electron identification (id) efficiency, electron tracking efficiency, muon id efficiency and triggering efficiency. The basic criteria to get all these efficiencies is to apply object quality cuts on a known sample of events *i.e.* a sample with known distributions and calibrated to some fixed reference.

8.2.1 Electron Selection and Identification Efficiency

For electrons, the detector efficiencies vary with cryostats (CC and EC) and depend on the choice of electron id. The electrons for this analysis were selected by using the cuts :
$E_T^e \geq 15$ GeV with $|\eta^e| \leq 2.5$
$f_{isol} \leq 0.1$
$L_5 \leq 0.5$
Electrons from $Z \rightarrow ee$ decay have similar kinematics to those in $t\bar{t}$ decays and were chosen as representative for efficiency calculation. The procedure was based on a sample of data with two reconstructed electromagnetic clusters with $E_T \geq 20$ GeV. One of the electron candidates, denoted as the 'tag', was required to satisfy tight identification cuts ($\chi^2 \leq 100, f_{isol} \leq 0.15$). If the second electromagnetic cluster, denoted as the 'probe' satisfied $f_{isol} \leq 0.1$, then the invariant mass of the pair, m (tag, probe) was recorded. This was done separately for probes in the central (CC, $|\eta^e| \leq 1.1$) and end cap (EC, $|\eta^e| \geq 1.1$ and $|\eta^e| \leq 2.5$) regions of the calorimeters. The number of entries in the Z mass window $80 <$ m (tag, probe) < 100 GeV were counted and corrected for the residual background.

[1]PMUO, PELC and PPHO are the definitions of muon, electron and photon respectively in DØ.

The electron tracking efficiency (ϵ_{trk}) which is just the probability to find a track in the road (to reconstruct a PELC) was determined from the above selected $Z \to ee$ data and is defined as

$$\epsilon_{trk} = \frac{\text{number of probes with a matching track}}{\text{total number of probes}} \tag{8.1}$$

The results vary with the number of reconstructed vertices per event. Typical values are $82.7 \pm 1.1\%$ for the CC and $85.2 \pm 1.0\%$ in the EC.

The second component of the identification efficiency is the electron cluster identification efficiency (effect of $L_5 \leq 0.5$ cut). This is given as

$$\epsilon_{clus} = \frac{\text{number of probes with a matching track passing } \mathrm{L}_5 \leq 0.5}{\text{total number of probes with a matching track}} \tag{8.2}$$

This gives results of $88.0 \pm 1.6\%$ in the CC and $63.8 \pm 2.3\%$ in the EC regions. For $t\bar{t}$ MC simulations there is an implicit tracking inefficiency built in. To avoid double counting when using the values of ϵ_{trk}, the results must be corrected (normalized) using the MC efficiencies (ϵ_{trk}^{MC}). These are $94.8 \pm 0.6\%$ for CC and $90.7 \pm 1.6\%$ in the EC. The total electron identification efficiency is then given by

$$\epsilon^{eid} = \epsilon_{clus} \times \frac{\epsilon_{trk}}{\epsilon_{trk}^{MC}} \tag{8.3}$$

and the results are shown below in Table 8.2.

ϵ_{CC}^{eid}	ϵ_{EC}^{eid}
0.768 ± 0.018	0.599 ± 0.025

Table 8.2: Electron identification efficiencies for Run I.

8.2.2 Muon Selection and Detection Efficiency

Muon tracks are reconstructed using the muon system PDTs. The muon selection criteria is different for Runs Ia, Ib and Ic because of the physical changes made to the WAMUS chambers and the trigger logic. Three sets of selection cuts are used, corresponding to the WAMUS configurations for Run Ia (1992-93), the first half of Run Ib (1994) and the second half of Run Ib and Ic (1994-95, 1996). Run Ia is treated separately because of the changes made in the L2 trigger logic to enable the use of the offline MTC package. The quality of a muon candidate depends on various factors. To separate out good muon a set of selection cuts are applied on the reconstructed muon tracks in the MC sample. During the first part of the 1994 data taking, it was found that the efficiencies of some of the WAMUS chambers in the central (CF, quad $\leq 4 \approx |\eta^{\mu}| \leq 1.0$) spectrometer close to MR beam pipe and the

forward (EF, quad > 4 and quad $\leq 12 \approx |\eta^{\mu}| > 1.0$ and $|\eta^{\mu}| \leq 1.7$) spectrometers showed serious deterioration. During the break in 1994 data taking the affected chambers were removed and cleaned to restore their efficiencies. Because of the efficiency problem the data taken in the precleaning period is restricted to the CF region and is referred to as the 'prezap' data. The post cleaning data uses both the CF and EF spectrometers and is referred to as the 'postzap' data. The cuts used for these three configurations are summarized in Table 8.3.

	Ia	Ib prezap	Ib+Ic postzap
	CF	CF	CF EF
$p_T^{\mu} \geq$	15	15	15
IFW4 $\leq$	1	1	1 0
calmip	yes	no	no
MTC	no	yes	yes
$\triangle R(\mu, jet) \geq$	0.5	0.5	0.5
$\triangle R(\mu, e/\gamma) \geq$	0.25	0.25	0.25

Table 8.3: Muon selection criteria.

Run	$\epsilon_{CF}^{\mu id}$	$\epsilon_{EF}^{\mu id}$
Run Ia	0.86 ± 0.073	-
Run Ib and Ic	0.89 ± 0.062	0.50 ± 0.059

Table 8.4: Muon identification efficiencies for Run Ia, Ib and Ic.

The total muon finding efficiency, $\epsilon^{\mu id}$ was determined from a combination of inclusive muon data and MC simulations and cross checked using $Z \rightarrow \mu\mu$ data. The value of $\epsilon^{\mu id}$ is given by the product :

$$\epsilon^{\mu id} = \epsilon_{trk} \times \epsilon_{\phi} \times \epsilon_{PMO} \tag{8.4}$$

where
ϵ_{trk} is the track finding efficiency in the WAMUS chambers.
ϵ_{ϕ} is a ϕ-dependent correction which is used to correct the monte carlo CF tracking efficiency in the region of the MR beam pipe.
ϵ_{PMO} is the efficiency for finding a muon using loose identification cuts.
The values of ϵ_{PMO} and ϵ_{ϕ} were determined from inclusive samples of high p_T muons and ϵ_{trk} was determined using the combination of cosmic ray data and MC calculations. Table 8.4 summarizes the total muon identification efficiencies which have been weighted according to luminosity fraction for the prezap and postzap parts of Run Ib.

8.2.3 Trigger Efficiencies

The number of $t\bar{t} \to e\mu$ events in the data is expected to be very small, therefore the only practical way to estimate the trigger efficiency is by using simulations. Trigger efficiencies are based on the TRIGSIM studies. TRIGSIM package comprises of two separate packages L1SIM and L2SIM. These simulate the L1 and L2 trigger logic and use the configuration files which were used during the actual data taking. The data were divided into four different classes according to the detector region into which the e and μ fell. These were chosen to enable an efficient simulation of the detector and trigger response which is strongly correlated to the location of the e and μ. The four classes are CCCF, CCEF, ECCF and ECEF where CCCF means that the electron is in CC and μ in CF; CCEF means that the electron is in CC and μ in EF; ECCF means that the electron is in EC and μ in CF; ECEF means that the electron is in EC and μ in EF. As the reference set, the files with a large number of runs have been used to calculate the trigger efficiency. The results are shown below in Table 8.5.

ϵ^{trig}_{CCCF}	ϵ^{trig}_{CCEF}	ϵ^{trig}_{ECCF}	ϵ^{trig}_{ECEF}
0.95 ± 0.05	0.93 ± 0.05	0.90 ± 0.04	0.93 ± 0.05

Table 8.5: Trigger efficiencies for Run I.

8.2.4 Combined Efficiencies

The trigger and particle identification efficiencies are combined to give four (trigger $\times$ id) efficiencies corresponding to the four e and μ classes. These are given as

$$\epsilon_{CCCF} = \epsilon^{trig}_{CCCF} \times \epsilon^{eid}_{CC} \times \epsilon^{\mu id}_{CF} \tag{8.5}$$
$$\epsilon_{CCEF} = \epsilon^{trig}_{CCEF} \times \epsilon^{eid}_{CC} \times \epsilon^{\mu id}_{EF} \tag{8.6}$$
$$\epsilon_{ECCF} = \epsilon^{trig}_{ECCF} \times \epsilon^{eid}_{EC} \times \epsilon^{\mu id}_{CF} \tag{8.7}$$
$$\epsilon_{ECEF} = \epsilon^{trig}_{ECEF} \times \epsilon^{eid}_{EC} \times \epsilon^{\mu id}_{EF} \tag{8.8}$$

Table 8.6 shows the resulting values.

Run	ϵ_{CCCF}	ϵ_{CCEF}	ϵ_{ECCF}	ϵ_{ECEF}
Run Ia	0.63 ± 0.08	-	0.47 ± 0.06	-
Run Ib + Ic	0.65 ± 0.06	0.36 ± 0.05	0.48 ± 0.05	0.28 ± 0.04

Table 8.6: Combined (Trigger $\times$ identification) efficiencies.

8.3 Selection Cuts

The selection cuts are applied to reduce the backgrounds and at the same time to enhance the top signal detection efficiency. We apply kinematical cuts to both the MC samples, signal as well as backgrounds, to get the raw acceptances. Keeping it in sight, we try to optimize the kinematical cuts so as to have a good signal to background ratio. This is achieved by calculating the expected event yield for both the signal and the background. Finally, these fine tuned cuts are applied to the detector data to look for the top quark signal. The selection cuts for the event selection criteria are listed in Table 8.7 and these cuts reduce the backgrounds as explained below.

Cut Number	Cut Definition
1	$E_T^e > 15$ GeV, $p_T^\mu > 15$ GeV/c + $\|\eta\|$ cuts
2	Require Isolated muons : $\triangle R_{\mu,jet} \geq 0.5$
3	$\not\!\!E_T{}^{cal} > 20$ GeV (Calorimeter/ICD/MG)
4	$\not\!\!E_T > 10$ GeV (muon corrected)
5	$\triangle R_{e\mu} \geq 0.25$
6	Require 2 jets, $E_T^{jet} > 15$ GeV
7	$H_T(E_T^e + \sum E_T^{jet}) > 120$ GeV
8	2 jets, $E_T^{jet} > 20$ GeV

Table 8.7: $e\mu$ selection cuts.

- **Cut 1 and Cut 2 :** The cuts on transverse energy of the leading electron (E_T^e) and transverse momentum of the leading muon (p_T^μ) are made to reduce the backgrounds coming from b and c quark decays (from QCD multijet events, $Z \rightarrow b\bar{b}$, $c\bar{c} \rightarrow e\mu$). These background processes do produce relatively high p_T muons which are not isolated as compared to the well isolated muons from W decay (in the standard $t\bar{t}$ decay scheme). The muon isolation requirements *i.e.* Cut 2 made for muon identification criteria reject these backgrounds. Cut 2 requires that the muon and jet be well separated because a typical non-isolated muon is very close to a jet. The MTC confirmation cut looks deeper in the hadronic layers of the calorimeter for the energy deposited by a muon.

- **Cut 3 :** The third cut requires the calorimeter missing E_T or $\not\!\!E_T{}^{cal}$ to be more than 20 GeV. Since neither muon nor the neutrino is seen by the calorimeter, a measurement of the E_T or $\not\!\!E_T{}^{cal}$ is equivalent to the measurement of the p_T of the W. A cut of 20 GeV on this quantity reduces the major instrumental background of W + jets $\rightarrow \mu$ + jets, where one of the jets is misidentified as

an electron. Whereas this cut has a little effect on the $t\bar{t}$ acceptance since for $t\bar{t} \to e\mu$ events, the $\not\!\!E_T^{cal}$ is derived from the high E_T electron and b jets.

- **Cut 4 :** The muon corrected $\not\!\!E_T$ is due to the two high p_T neutrinos present in the $t\bar{t} \to e\mu$ events. One of the major backgrounds to produce so much $\not\!\!E_T$ is $Z \to \tau\tau \to e\mu$. A cut off at $\not\!\!E_T > 10$ GeV reduces the cross-section of this background significantly.

- **Cut 5 :** A high p_T muon will occasionally be accompanied by initial state bremsstrahlung and the majority of these photons will be very close to the parent muon (in $\eta - \phi$ space). In such a situation the photon will be matched to the muon track in the central tracking system and will be labeled as an electron by DØRECO and thus creating an $e\mu$ event. Cut 5 effectively removes such events while having no effect on the $t\bar{t}$ acceptances.

- **Cut 6 :** The sixth cut requires the presence of two jets with $E_T > 15$ GeV. This cut reduces the $WW \to e\mu$, $Z \to \tau\tau \to e\mu$ and W + jets backgrounds.

- **Cut 7 :** At this stage most of the backgrounds are reduced significantly by the above selection cuts but the most pronounced of all the backgrounds; $Z \to \tau\tau$ and WW are still prevalent. The final cut of $H_T > 120$ GeV, where H_T is just the scalar sum of E_T^e and $\sum E_T^{jet}$ efficiently cuts down these backgrounds. Since the top quark is heavy, and hence top events are more spherical than background events and are produced more centrally in the detector. This cut does not affect the top signal much.

- **Cut 8 :** Finally, the jets E_T cut is tightened to 20 GeV. This cut, drastically, cuts down all the WW pairs, $Z \to \tau\tau$ and W + jets $\to \mu$ + jets backgrounds whereas having very little effect on the signal.

8.4 Acceptances for $t\bar{t} \to e\mu$

After getting the selection cuts optimized as explained in Sec. 8.3, we have applied these cuts on different MC samples for both signal and background. The samples of different top masses from (165 - 190 GeV) have been used. The ratio of the events left after these cuts to the total number of input events gives the selection cut efficiency. Using this acceptance we have calculated the overall top detection efficiency (ϵ) which is the product of all the efficiencies (including selection cuts efficiency).

The total acceptance $\mathcal{E}$ for a given process is given by :

$$\mathcal{E} = \epsilon \times \mathrm{BR} = \mathrm{BR} \times \frac{N_{\mathrm{cut}}^{\mathrm{tot}}}{N_{\mathrm{input}}} \tag{8.9}$$

where $N_{\rm cut}^{\rm tot}$ is the number of events surviving after the cuts have been applied and is given as :

$$\begin{aligned} N_{\rm cut}^{\rm tot} &= N_{\rm CCCF} \times \epsilon_{\rm CCCF} \\ &+ N_{\rm CCEF} \times \epsilon_{\rm CCEF} \\ &+ N_{\rm ECCF} \times \epsilon_{\rm ECCF} \\ &+ N_{\rm ECEF} \times \epsilon_{\rm ECEF} \end{aligned} \tag{8.10}$$

where $N_{\rm CCCF}$, $N_{\rm CCEF}$, $N_{\rm ECCF}$, $N_{\rm ECEF}$ are the number of events remaining in CCCF, CCEF, ECCF and ECEF class respectively, $\epsilon_{\rm CCCF}$, $\epsilon_{\rm CCEF}$, $\epsilon_{\rm ECCF}$ and $\epsilon_{\rm ECEF}$ are the corresponding selection efficiencies and $N_{\rm input}$ is the starting number of events. BR is the branching fraction of $t\bar{t} \rightarrow$ dileptons (e, μ only). After including for the τ decay modes ($\tau \rightarrow e\mu$) it takes the value of 0.0685.

The expected number of events for a given process is then given by :

$$N^{\rm expected} = \sigma_{\rm input} \times \mathcal{E} \times \int \mathcal{L} dt \tag{8.11}$$

where $\sigma_{\rm input}$ is the input cross-section and the $\int \mathcal{L} dt$ is the total integrated luminosity.

We have studied two major physics backgrounds : $Z \rightarrow \tau\tau \rightarrow e\mu$ and $WW \rightarrow e\mu$. To calculate the event yields for these backgrounds, we have used MC event samples with cross-section taken from either experimental measurements or NLO QCD calculations. For $Z \rightarrow \tau\tau \rightarrow e\mu$ process, the experimental measurement of cross-section has been taken. Whereas, for $WW \rightarrow e\mu$ NLO QCD cross-section has been taken (see Sec. 2.6.2).

The event yields for $t\bar{t} \rightarrow e\mu$X processes have been calculated using MC event samples. For these MC samples, the cross-section was normalized to the resumed NLO QCD result of Laenen *et al.* [8]. The events were processed through the full DØGEANT and DØRECO and used to calculate results for the selection efficiency as a function of the number of interactions.

The cross-section for the $t\bar{t} \rightarrow e\mu$X process, $\sigma_{t\bar{t}}(m_t)$ is given as :

$$\sigma_{t\bar{t}}(m_t) = \frac{N_{\rm obs} - < B >}{\mathcal{E} \times \int \mathcal{L} dt} \tag{8.12}$$

where $N_{\rm obs}$ is the number of events observed in the data, $< B >$ is the expected background, $\mathcal{E}$ is the total acceptance for the $t\bar{t}$ process. The number of expected events for signal and background have been determined using Eqn. 8.12.

The number of top events expected from 108.3 ± 5.7 pb^{-1} of integrated luminosity and $\sigma_{t\bar{t}}$ (central value) from Laenen *et al.* for various top masses are tabulated in Table 8.8. Tables 8.9 summarizes number of expected events for the background processes.

Finally, we use the same optimized selection cuts on data to get top signal. The data used here in our analysis were accumulated by DØ during Run I (1992-

96) at Tevatron, Fermilab USA. Following the same procedures as explained in previous chapters to get signal, finally we are left with 3 top $e\mu$ candidates in Run I DØ detector data. The final results are summarized in Table 8.10. The errors on the expected number of events and the total number of background events include both statistical and systematic errors.

Therefore, for the present analysis, using conventional methods, the number of observed events are 3 and number of estimated background events is 0.09 ± 0.03. Three top $e\mu$ candidates left are with event numbers 417, 12814 and 26920.

$\int \mathcal{L}dt = 108.3 \pm 5.7$ pb^{-1} Branching Ratio (BR) for ($t\bar{t} \rightarrow$ dileptons (e, μ or $\tau \rightarrow$ e or μ)) = 6.85%			
Top Quark Mass (GeV)	Cross-Section (σ_{input}) (pb^{-1})	($\epsilon \times$ BR)%	N^{expected}
165	6.89 ± 0.17	0.303 ± 0.054	2.26 ± 0.42
170	5.83 ± 0.14	0.321 ± 0.057	2.03 ± 0.38
175	4.94 ± 0.12	0.334 ± 0.060	1.79 ± 0.34
180	4.21 ± 0.01	0.353 ± 0.063	1.61 ± 0.30
185	3.59 ± 0.09	0.365 ± 0.066	1.42 ± 0.27
190	3.06 ± 0.08	0.377 ± 0.068	1.25 ± 0.24

Table 8.8: Event yields for the MC signal Run I.

$\int \mathcal{L}dt = 108.3 \pm 5.7$ pb^{-1}	
Background Process	N^{expected}
$Z \rightarrow \tau\tau \rightarrow e\mu$	0.02 ± 0.01
$WW \rightarrow e\mu$	0.07 ± 0.02

Table 8.9: Event yields for the MC background Run I.

$\int \mathcal{L}dt = 108.3 \pm 5.7$ pb^{-1}	
Sample	Number of Events
Signal MC (170 GeV)	2.03 ± 0.38
Total Background	0.09 ± 0.03
Data	3

Table 8.10: $e\mu$ final summary for Run I.

The errors quoted in the above tables include both the statistical as well as systematical errors (added in quadrature).

8.5 Analysis Techniques

The top quark mass is an important parameter in the Standard Model (SM), as together with the mass of W boson (m_W) it constraints on the mass of the SM Higgs boson. Therefore, it is very important to get any improvement in the precision of the top quark mass measurements. The Higgs boson, the W boson and the top quark contribute via radiative corrections to observables already measured at LEP and SLC so that the measured observables together with the measured values of the W and the top mass restrict the allowed mass range of the Higgs boson. Recent experimental constraints on the Higgs boson mass are consistent with the SM [2]. In the future, when the W boson mass should be measured to an accuracy of 40 MeV, a precision of about 1 GeV in the top mass would yield a prediction in the Higgs boson mass of $\delta m_H/m_H \leq 40\%$. We have been motivated to use alternate methods to determine the top quark mass, which are relatively simple. The methods which we have used/developed for our analyses are Neural Networks method and method of four vectors. We have also tried to determine the top quark mass by using $e\mu$ invariant mass.

8.5.1 Neural Networks

Neural Networks are extraordinarily powerful data analysis tools and are now very widely used in several fields *e.g.* in medicine for image analysis or help to diagnosis in industry for automatic process control, for quality checks by image processing or for optimization of resources allocation and in meteorology for weather forecast. In Particle Physics, these are commonly used, mainly for offline classification tasks such as particle identification, event classification and search for new physics. These are also used for track reconstruction or for online triggering. Neural Network (NN) models are algorithms for cognitive tasks such as learning and optimization, which are in a loose sense based on the concepts derived from research into the nature of the brain. We have studied NN techniques to explore its use in the determination of the top quark mass.

Biological Neural Networks

Artificial Neural Network (ANN) is inspired from the structure of biological neural networks and their way of encoding and solving the problem. ANN is a mathematical model which exhibits features and functionality of the Vertebrate Central Nervous System (CNS).

The basic unit of signal processing in the brain is a *neuron*. The human brain contains approximately 10^{11} interconnected neurons. The most general structure of neuron is shown in Figure 8.1. This general neuron structure is implemented in many different sizes and forms with different functionalities. Cell bodies have diameters in the range 5-80 μm and dendrite "trees" extend from 10 μm upto 2-3

mm. Axons can be upto 1 m in length. Primary sensory neurons connect muscles or receptors to neurons, secondary sensory neurons and interneurons connect neurons with neurons, while motor neurons connect neurons with muscle fibres. The interior of the cell body is negatively charged against a surrounding extracellular fluid. The cell body or soma receives electric input signals to the dendrites by the means of ions. The signals are electrical pulses caused by bio-chemical changes. Signals arriving at the dendrites depolarise the resting potential, enabling Na^+ ions to enter the cell through the membrane, resulting in an electric discharge from the neuron. The signals arriving at the neuron are summed and if this sum is greater than a threshold, the neuron is "fired". The fired neuron in turn sends a signal to the connected neurons which may result in the firing of other neurons in the network. The accumulated effect of several simultaneous signals arriving at the dendrites is approximately linearly additive whereas the resulting output is a strongly non-linear all-or-none type process. The discharge propagates along the axon to a synaptic junction whereas neurotransmitters travel across a synaptic cleft and reach the dendrites of the postsynaptic neuron. A synapse which repeatedly triggers the activation of a postsynaptic neuron will grow in strength, others will gradually weaken. This plasticity, which is known as "Hebb Rule", plays a key part in learning.

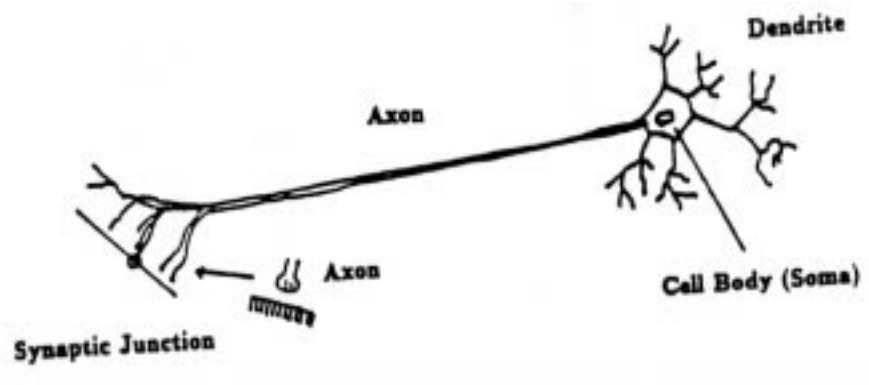

Figure 8.1: Schematic structure of a neuron.

Artificial Neural Networks

Artificial Neural Network (ANN) is a computational paradigm that differs substantially from those based on the "standard" von Neumann architecture. ANNs generally learn from "experience" rather than being explicitly "programmed" with rules like in conventional artificial intelligence. These are often used as a way of optimizing a classification (or pattern recognition) procedure and have been applied to many pattern recognition problems in physics [54] - [58]. The philosophy of the ANN approach is to abstract some key ingredients from biology and out of those

construct simple mathematical models. ANN consists of building block called *node* (also called unit). A node is an abstraction of the biological neuron.

In mathematical terms, a NN model is defined as a directed graph with the following properties :

1. A state variable ν_i, associated with each node i.
2. A real-valued weight ω_{ij}, associated with each link between two nodes i and j.
3. A real-valued bias θ_i, associated with each node i.
4. A transfer function $g(x)$, defined for each node i which determines the state of the node as a function of its bias, of the weights of its incoming links and of the states of the nodes connected to it by these links.

In the standard terminology, the nodes are called neurons, the links are called synapses and the bias is known as the activation threshold. Mathematically, each node can be considered as a variable whose value is a non-linear function of the superposition of the values of the other nodes and it can be shown as :

$$\nu_i = g(\sum_j \omega_{ij}\nu_j + \theta_i) \tag{8.13}$$

where ν_j are neurons which are feeding neuron ν_i through weights (synapses) ω_{ij}.

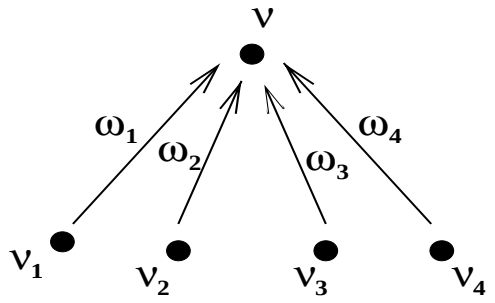

Figure 8.2: Nodes ν_j feeding the node ν.

These weights can have both positive (excitatory) and negative (inhibitory) values. The θ_i is called the threshold, corresponding to the membrane potential in a biological neuron. The threshold and weights may be collectively symbolized as weights $\omega = \{\omega_i, \theta\}$. One can say that the nodes, ν_j feed ν_i as shown in Figure 8.2.

The simple "thresholding neuron" mimics the main features of real biological neuron in terms of linear additivity for the inputs and strong non-linearity for the resulting output. If the integrated input signal is larger than a certain threshold θ_i, the neuron will be fired.

The non-linear transfer function (activation function) $g(x)$, is typically a sigmoid function as shown in Figure 8.3 and is given as :

$$g(x) = (1 + e^{-2x}) - 1 \tag{8.14}$$

A linear combination of sigmoids is useful because of the two theorems

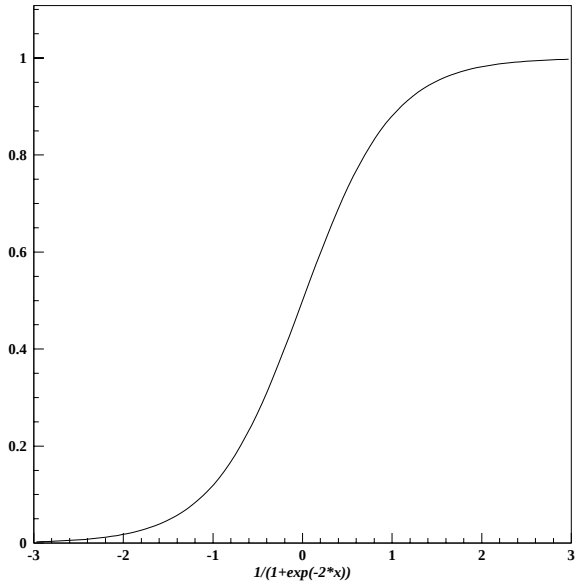

Figure 8.3: A sigmoid function.

- a linear function of sigmoids can approximate any continuous function of one or more variables. This is useful to obtain a continuous function fitting a finite set of points when no underlying model is available.
- trained with a desired answer equal to 1 for signal and 0 for background, the approximate function is the probability of signal knowing the input values. This second theorem is the basic ground for all classification applications.

By connecting nodes one can design any arbitrary architecture for a NN. There are two different kinds of architectures in NN modeling : Feed Forward Neural Network and Feed Backward Neural Network.

8.5.2 Feed Forward Neural Networks

In Feed Forward Neural Networks (FFNNs), signals are processed from a set of input units in the bottom to output units in the top, layer by layer. In feed

backward networks, the activation is bidirectional and it continues until a fixed point has been reached. In HEP, the feed forward (FF) architectures are used for pattern reorganization and function mapping problems in a wide area of applications and these have become increasingly popular.

We have restricted ourselves to FF networks with three layers of nodes - an input layer, an output layer and an intermediate layer known as *hidden layer* as shown in Figure 8.4. The mathematical expression for a general FF network with one hidden

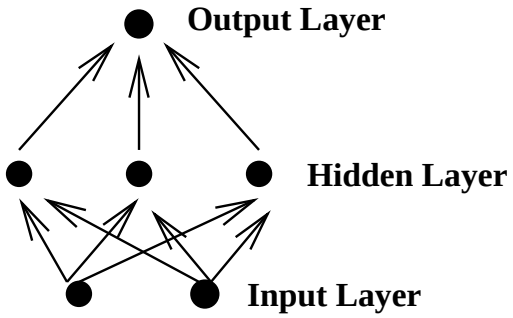

Figure 8.4: A feed forward neural network.

layer and one output is

$$y = g(\frac{1}{T}\sum_{j}^{N_h}\omega_j g(\frac{1}{T}\sum_{i}^{N_j}\omega_{ji}x_i + \theta_j) + \theta) \tag{8.15}$$

where N_j is the number of input nodes, N_h is the number of hidden nodes, ω_{ji}'s are the weights connecting the input nodes x_i's to hidden nodes j and the ω_j connects the hidden nodes to the output node y, θ_j and θ are the thresholds of the hidden and output nodes respectively.

Therefore, FFNN can be considered as a non-linear function of $\vec{x}$ with several parameters ω,

$$y = F(\vec{x}, \omega) \tag{8.16}$$

$F(\vec{x}, \omega)$ is a function which is to be modeled, to arbitrarily high accuracy, a given probability density.

8.5.3 NN Training

NNs have to be trained with the sufficient number of training patterns to get optimal discrimination. In the training process, the $\omega's$ are fitted using the gradient descent method on a suitable error function. In this process, the training patterns (events in the MC sample) are presented over and over again with successive updating of the weights. As soon as this iterative process reaches an acceptable level of low error, the training process is stopped and the weights are frozen. We then

feed the network by patterns that the network has never seen before to classify the events in our data used *e.g.* signal and background. One can say that the training is done to minimize the error between the desired response and the network's actual response. A commonly used error function is the Mean-Square-Error (MSE), averaged over the training sample and is defined as :

$$E(\omega) = \frac{1}{2N_p} \sum_{i=1}^{N_p} (y_i(\omega) - d_i)^2 \tag{8.17}$$

where N_p is the number of patterns used for updating the weights, y is the output of the NN as given in Eqn. 8.15 and d is the desired output and ω denotes the set of parameters that are to be adjusted so as to minimize the error function given in Eqn. 8.17.

In supervised training, training samples are labeled, so the desired outputs are

$$d_i = \delta_{ij} \tag{8.18}$$

e.g. the case in which we have two classes - signal and background, we have :

$$d = \begin{cases} 1, & \text{for signal} \\ 0, & \text{for background} \end{cases}$$

We force the network output to be close to the desired output by minimizing the error function $E(\omega)$. Several algorithms are available for error minimization. Gradient-Descent is the most widely used method in HEP. This is also known as the back propagation learning algorithm. In the Gradient-Descent algorithm the ω's are randomly chosen initially. The weights are updated using

$$\omega(t+1) = \omega(t) + \triangle\omega(t) \tag{8.19}$$

N_p patterns from the training patterns are picked and then the ω's are changed in the direction along which E decreases fastest *i.e.*

$$\triangle\omega(t) \propto -\frac{\partial E}{\partial \omega} \tag{8.20}$$

so,

$$\triangle\omega(t) = -\eta \frac{\partial E}{\partial \omega} = -\eta \nabla E \tag{8.21}$$

where ω is a vector of weights and thresholds used in the network, t refers to the iteration index, η is the multiplicative factor known as *learning rate* which is identical in all the directions of ω space.

This procedure is convergent mathematically [59]. This means that after a sufficient number of iterations, E reaches a minimum and the ω's are fixed. In order to avoid oscillations around the minimum and reach the minimum error faster, an

extra term known as the *momentum term* is usually added to Eqn. 8.21

$$\triangle\omega(t+1) = -\eta\frac{\partial E}{\partial\omega} + \alpha\triangle\omega(t) \tag{8.22}$$

A critical property of a trained network is the generalization or the ability to accurately predict results from previously unencountered input data. Good generalization is a goal of NN training and is one of the strength of back-propagation.

8.5.4 Bayesian Interpretation of the FFNN

In a typical high energy physics analysis, the feature vectors characterize events and an important goal is to try to assign an event of known identity to its proper class *i.e.* a basic task is to separate data into two classes called signal and background. Having isolated the signal, the next task is usually to estimate the value of a parameter (or set of parameters) which characterizes the signal. Both tasks can be solved optimally provided that one has at hand an adequate approximation to probability distribution of the experimental quantities which describe the signal+background. The best way to do this is, in that it minimizes the probability of making mistakes, to use the *Bayes decision rule i.e.* to compute the (Bayesian posterior) probability $P(k|\vec{x})$ of $\vec{x}$ belonging to class k with the highest probability, where in our case the classes of data are K=(top,WW,$Z\tau\tau$). Under proper assumptions the output of a FFNN can be interpreted as Bayesian probability [60].

Typically in an experiment one measures n-variables $(x_1, ..., x_n)$, many times. Each set of n-variables can be thought of as a vector x $\equiv \vec{x} = (x_1, ..., x_n)$ of mass-dependent variables in an n-dimensional space.

We can prove that the output of NNs are approximately equal to functions of certain probabilities [60] *i.e.* we show that if the number of events is sufficiently large and if the NN is flexible enough then the output of the NN is,

$$F(\vec{x}, \omega) = P(S|\vec{x}) \tag{8.23}$$

where $P(S|\vec{x})$ is the probability that the feature vector, $\vec{x} = (x_1, ..., x_n)$ belongs to the signal class S. This is precisely the probability we need to solve the classification problem.

Suppose, $P(\vec{x}|S) \rightarrow$ Probability density function of the $\vec{x}$ for the signal
$P(\vec{x}|B) \rightarrow$ Probability density function of the $\vec{x}$ for the background
$P(S) \rightarrow$ Prior probability of an event being a signal
$P(B) \rightarrow$ Prior probability of an event being a background

We assume that the signal events S and the background events B to be mutually exclusive *i.e.* their union is equal to the complete sample space *i.e.*

$$P(S) + P(B) = 1 \tag{8.24}$$

According to Bayes theorem on conditional probability

$$P(S|\vec{x}) = \frac{P(\vec{x}|S)P(S)}{P(\vec{x})} \tag{8.25}$$

$$P(B|\vec{x}) = \frac{P(\vec{x}|B)P(B)}{P(\vec{x})} \tag{8.26}$$

where

$$P(\vec{x}) = P(\vec{x}|S)P(S) + P(\vec{x}|B)P(B) \tag{8.27}$$

Then, the optimal way to partition the feature space is cut on the ratio of these probabilities,

$$R(\vec{x}) = \frac{P(S|\vec{x})}{P(B|\vec{x})} = \frac{P(\vec{x}|S)P(S)}{P(\vec{x}|B)P(B)} \tag{8.28}$$

where R is the Bayes discriminant function. $P(S|\vec{x}), P(B|\vec{x})$ are also known as Bayesian probabilities. Ratio $P(S)/P(B)$ is typically equal to the ratio of signal to background cross-section. A cut of R is the optimal way to classify events. If $R > 1$, event is called a signal event. If $P(S) = P(B)$, R reduces to likelihood ratio. For the classification problem, we normally choose $S = 1$ and $B = 0$ in which case $F \equiv F(\vec{x}, \omega)$. *i.e.* the neural network output is an approximation to the probability that a feature vector $\vec{x}$ belongs to the class S.

8.5.5 Neural Network Package

We have used Multi Layer Perceptron (MLP) package, MLPfit, for our analysis. The MLP is the most widely used type of NN. It is both simple and based on solid mathematical grounds. Input quantities are processed through successive layers of neurons. There is always an input layer with a number of neurons equal to the number of variables of the problem, and an output layer where the perceptron response is made available, with a number of neurons equal to the desired number of quantities computed from the inputs. The layers in between are called hidden layers. With no hidden layer, the perceptron can only perform linear tasks. Each neuron of a layer other than the input layer computes first a linear combination of the outputs of the neurons of the previous layer, plus a bias. The coefficients of the linear combination plus the biases are called the weights. These are usually determined from examples, to minimize, on the set of examples. Neurons in the hidden layer then compute a non-linear function of their inputs.

MLPfit is a modular tool for designing and using Multi Layer Perceptron. It implements powerful learning methods. The code is simple to use and has been designed for an easy implementation of additional features and for an easy interfacing to additional packages. The MLPfit routines are interfaced to the PAW [53] analysis package. The Multi Layer Perceptron interface in PAW :

- can be used for both approximation and classification tasks.

- provides preformant minimization methods to determine the weights.
- allows to interactively define, train and use the NN.

So, by using a few commands with a syntax close to the usual PAW commands, it is possible to

- define the network structure.
- modify the default learning parameters.
- read/write weight files. define examples from ASCII files, histograms or ntuples. When examples are defined from Ntuples, selection criteria may be added.
- train the network and follow the learning curve while training.
- write out the function for use in any other code or for direct use in PAW.

MLPs are implemented in PAW through an interface to the MLPfit package (version 1.40).

8.5.6 Method of Four Vectors

For the top quark mass determination, we describe a relatively simple and new method which is based upon the four vectors. Any set of four quantities which transform like $(t, \vec{x})$ under Lorentz transformation is called a four vector. The most familiar four vectors are :

$$x^{\mu} = (t, \vec{x})$$
$$p^{\mu} = (E, \vec{p})$$

where

$$\begin{aligned} \vec{x} &= (x, y, z), \\ \vec{p} &= (p_x, p_y, p_z) \end{aligned}$$

The decay

$$p\bar{p} \rightarrow t\bar{t} \rightarrow bW^{+}\ \bar{b}W^{-} \rightarrow e\nu_e\mu\nu_{\mu} + jets$$

has been studied in which one top quark yields a b quark and an electron (e) and the other a b quark and a muon (μ). As mentioned in Sec. 2.6, the branching ratio for the $e\mu$ channel is 2.4% to be compared with 15% for a single lepton channel. The main disadvantage of the $t\bar{t}$ dilepton channels is their small branching ratio. However, the dilepton channels have smaller backgrounds, which is especially true in the $e\mu$ channel whose principal backgrounds are from $Z \rightarrow \tau\tau \rightarrow e\mu$ and $WW \rightarrow e\mu$.

Methodology

We have observed that any quantity that depends upon the top quark mass can be used to measure it. In particular, it is not necessary that these quantities be the result of kinematic fits. We have included the mass dependent quantities, provided that the quantities are sufficiently uncorrelated, to improve the precision of the top quark mass. This strategy was successfully exploited by CDF in their top quark mass measurement in the dilepton channel [61]. DØ [62] used a variation of the Kondo [63], Dalitz-Goldstein [64] method.

Our method is based on the following mass dependent quantities :

$$x_1 = \sqrt{(2j_1 \cdot j_2)} \tag{8.29}$$

$$x_2 = \sqrt{(2e \cdot j_1 + m_W^2)} \tag{8.30}$$

$$x_3 = \sqrt{(2e \cdot j_2 + m_W^2)} \tag{8.31}$$

$$x_4 = H_T(E_T^e + \sum_{\text{all jets}} E_T^{jet}), \tag{8.32}$$

where e, j_1 and j_2 are, respectively, the four vectors of the electron and two highest transverse momentum jets and m_W is the mass of the W boson.

The quantities x_2 and x_3 are inspired by the arguments presented in [65]. The use of quantities x_2 and x_3 presupposes that the b-jet can be associated with the corresponding lepton with high efficiency and we should keep only one of the two variables : the one in which the lepton and the jet arise from the same top quark and the distribution of that variable is bounded between m_W and m_t. The effective algorithm to do this job of associating b-jet with the corresponding lepton has not been yet devised [65]. Therefore, at present, we are unable to choose the right pairing with sufficiently high probability and we keep both the variables. The development for such an algorithm is being viewed as a high priority.

Since there are two leptons in the $e\mu$ event, we can form two more variables (x_2', x_3') like x_2 and x_3 by using the muon four vectors which can be given as :

$$x_2' = \sqrt{(2\mu \cdot j_1 + m_W^2)} \tag{8.33}$$

$$x_3' = \sqrt{(2\mu \cdot j_2 + m_W^2)} \tag{8.34}$$

However, we have chosen not to use the muon information because of its relatively modest precision. In Run II, we anticipate a significant improvement in the muon momentum measurement, because of the introduction of a central magnetic field. It should then be possible to use the muon four vectors and thus augment the aforementioned variables (x_1, x_2, x_3, x_4) with two more *i.e.* (x_2', x_3').

The dependence of the mean values of the variables $x1, ..., x4$ on the top quark mass is studied for the MC samples. From a sample of $e\mu$ candidates, the mean values of $x1, ..., x4$ are computed and corresponding to each quantity, top quark

mass m_i $(i = 1, ..., 4)$ is determined. As the final estimate of the top quark mass, we take the weighted average

$$\hat{m}_t = \sum_{i=1}^{4} w_i m_i, \tag{8.35}$$

where w_i are the weights derived from the standard deviation of the distributions m_i and are given as :

$$w_i = \frac{1}{Var[m_i] \sum_i 1/Var[m_i]} \tag{8.36}$$

$Var[m_i]$ is the variance of the distribution of the mass estimate m_i. These weights minimize the variance of the distribution of $\hat{m}_t$ when the m_i are uncorrelated. There is, however, some correlation between these variables. For this reason we can estimate the error on $\hat{m}_t$ directly from the $\hat{m}_t$ distribution.

Chapter 9

Top Quark Mass Analyses

The DØ detector is upgraded to center-of-mass energy $\sqrt{s} = 2.0$ TeV in Run II. As a result, the Run II data would be quite large; about 100 times the Run I data. To exploit the full use of high statistics, the main task is to reduce systematic errors so that we can benefit from the reduced statistical errors. We need to explore different methods to cross-check the results and also use different methods which may yield smaller systematic errors by using as many decay modes as possible. The present study is a step towards this goal by studying one of the channel via which top quark can decay. The decay $p\bar{p} \rightarrow t\bar{t} \rightarrow bW^+ \, \bar{b}W^- \rightarrow e\nu_e\mu\nu_\mu + jets$ has been studied for our analyses. In this chapter, we present the results based on different methods which we have used to determine the top quark mass.

9.1 NN Method

NNs are extraordinarily powerful data analysis tools and are widely used in HEP. After the successful use of method of NNs for the top quark cross-section in [29], we have been motivated to explore the use of NNs in the determination of the top quark mass. High energy physicists hope to reduce the uncertainty substantially in our knowledge of the top quark mass [66] as the Tevatron will deliver about one hundred times more data in Run II than was collected during Run I. Keeping these two facts in account, we have used the method of neural networks on the existing data of DØ Run I and then checked it on simulated data for Run II to see this effect on the top quark mass.

9.1.1 Simulated Data Analysis using NN

To check whether our method really works good, we have carried out the simulations for the $p\bar{p}$ collision at $\sqrt{s} = 2.0$ TeV. We have restricted ourselves to the $e\mu$ channel *i.e.* $p\bar{p} \rightarrow t\bar{t} \rightarrow e\mu + X$ decay, in which one top quark yields a b quark and an electron (e) and the other a b quark and a muon (μ). The major backgrounds for this channel are from the reactions $p\bar{p} \rightarrow Z \rightarrow \tau\tau \rightarrow e\mu$ and $p\bar{p} \rightarrow WW \rightarrow e\mu$. For this part of study, MC sample for both signal and background *i.e.* $t\bar{t}$, Z and

WW events, have been simulated using **PYTHIA** event generator and the detector (DØ Run II) has been simulated using SUSY/Higgs Workshop (**SHW**) package. Refer to Sec. 6.3.3 (B) for the MC simulation for DØ Run II detector.

The preferred way to measure the mass of a particle created in a high energy event is to perform a complete kinematic reconstruction of the event. However, for the $e\mu$ channel, as is true of the other dilepton channels, there is insufficient information available to effect a complete kinematic reconstruction, although it is possible to perform a partial reconstruction [67]. An alternative strategy is to use mass dependent quantities that are not necessarily derived from kinematic fits [65, 68]. In this study we have used a variable $x(l, b)$ which is defined as :

$$x(l, b) = \sqrt{(2l.b + m_W^2)} \tag{9.1}$$

where m_W is the W boson mass, and l and b are lepton and b-jet four vectors. This variable has the virtue of being insensitive to jet systematic uncertainties [65] and has a distribution whose mean is an almost linear function of the top quark mass. Moreover, if the b-jet and the lepton l come from the same top quark, the distribution of x ends at the top quark mass, as shown in Figure 9.1. But to avail oneself of this useful feature requires an efficient algorithm for correctly pairing the leptons and the b-jets. We have considered the four pairings of two leptons and two b-jets. As shown in Figure 9.1 (b-e), the effect of the mispairing is to broaden the x distributions beyond the top quark mass. However, these variables are still mass dependent and can therefore be used to measure the top mass.

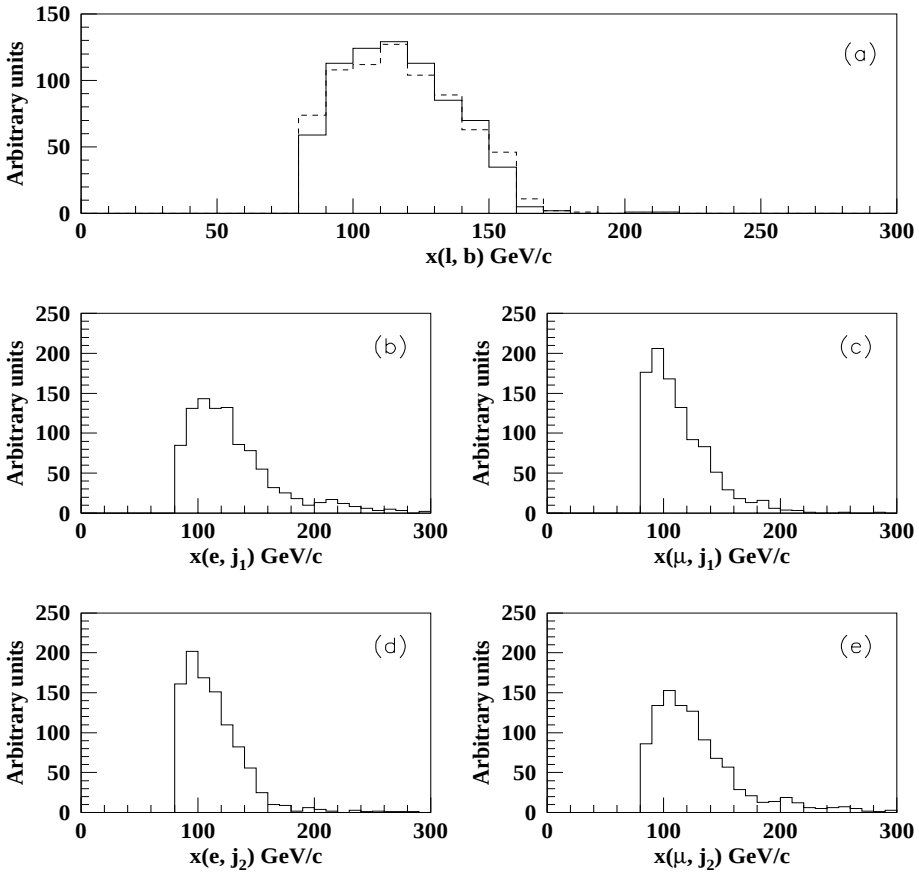

Figure 9.1: (a) The distribution of x after event reconstruction (solid line), for correctly paired lepton and b-jet, compared with the distribution at the parton level (dashed line). Figure 9.1 (b-e) The distribution of x after reconstruction for all pairings of leptons and jets. The distributions are for top quark mass of 170 GeV.

We have associated each class label k with a top quark mass m_k; $P(k|\vec{x})$ may then be interpreted as the probability that the top quark mass is m_k given the measured vector

$$\vec{x} = [x(e, j_1), x(\mu, j_2), x(\mu, j_1), x(e, j_2)] \tag{9.2}$$

If the output d as given in Eqn. 8.18 is set to the top quark mass m_k, then the Eqn. 8.23 becomes the mean of the posterior probability of the top quark mass, which, from a Bayesian viewpoint, is a natural estimate of that quantity and moreover is a quantity that can be directly estimated using a NN.

We have used (4,n,1) NN (with n, the number of hidden nodes typically equal to 5) to estimate the posterior mean. We have trained this NN by setting the target value equal to the top quark mass associated with the feature vector $\vec{x}$. As mentioned above, we have used PYTHIA event generator and SHW package for detector simulation. We have generated $p\bar{p} \to t\bar{t}WbWb \to (e/\mu)\nu\ (e/\mu)\nu$ samples for top quark masses ranging from 100 GeV to 240 GeV in the step of 5 GeV. For each mass, 1000 $e\mu$ events have been generated to test the NN method. To a large extent the method relies on the proper MC (PYTHIA) description of top production and decay. To reduce the backgrounds, different combinations of kinematical cuts have been tried. Finally, the events have been selected with the following cuts :

(i) Transverse energy of the leading electron, $E_T^e \geq 15$ GeV with $|\eta^e| \leq 2.5$

(ii) Transverse energy of the leading muon, $p_T^\mu \geq 15$ GeV with $|\eta^\mu| \leq 2.5$

(iii) Number of jets, $N_{jet} \geq 2$ with $E_T^{jet} \geq 15$ GeV and $|\eta^{jet}| \leq 2.5$

(iv) Requirement of isolated muons in a cone of radius, $\Delta R_{\mu,jet} \geq 0.5$ where $\Delta R = \sqrt{\Delta\eta^2 + \Delta\phi^2}$ in η-ϕ space.

For each top quark mass 300 feature vectors, $\vec{x}$ as given in Eqn. 9.1 have been used. The NN has been trained by taking this variable $x(l, b)$ as four input nodes. The NN training has been done using the MLPfit program. MLPfit's default algorithm has been used for minimizing error function $E(w)$. The NN has been trained for 100 cycles. To avoid overtraining the network was validated on an independent sample. As mentioned in Sec. 8.5.4, the NN output is an approximation to the probability that a feature vector $\vec{x}$ belongs to the signal class. To use this fact, we have determined the NN output and its distribution has been studied. The mean of this network output distribution (*i.e.* the mean of the distribution of posterior mean) as a function of the top quark mass has been studied. It has been observed that the mean of the network output distribution depends linearly on the top quark mass. This linear relationship over the top quark mass range 100 to 240 GeV is shown in Figure 9.2. The points define a curve that is linear within the range 140 to 190 GeV and non-linear outside *i.e.* it is having a sigmoidal shape which is due to the fact that at the lower end, the truncation at 100 GeV forces the posterior mean to be on average somewhat greater than 100 GeV. Likewise, at the upper end the posterior mean will on average be somewhat less than 240 GeV.

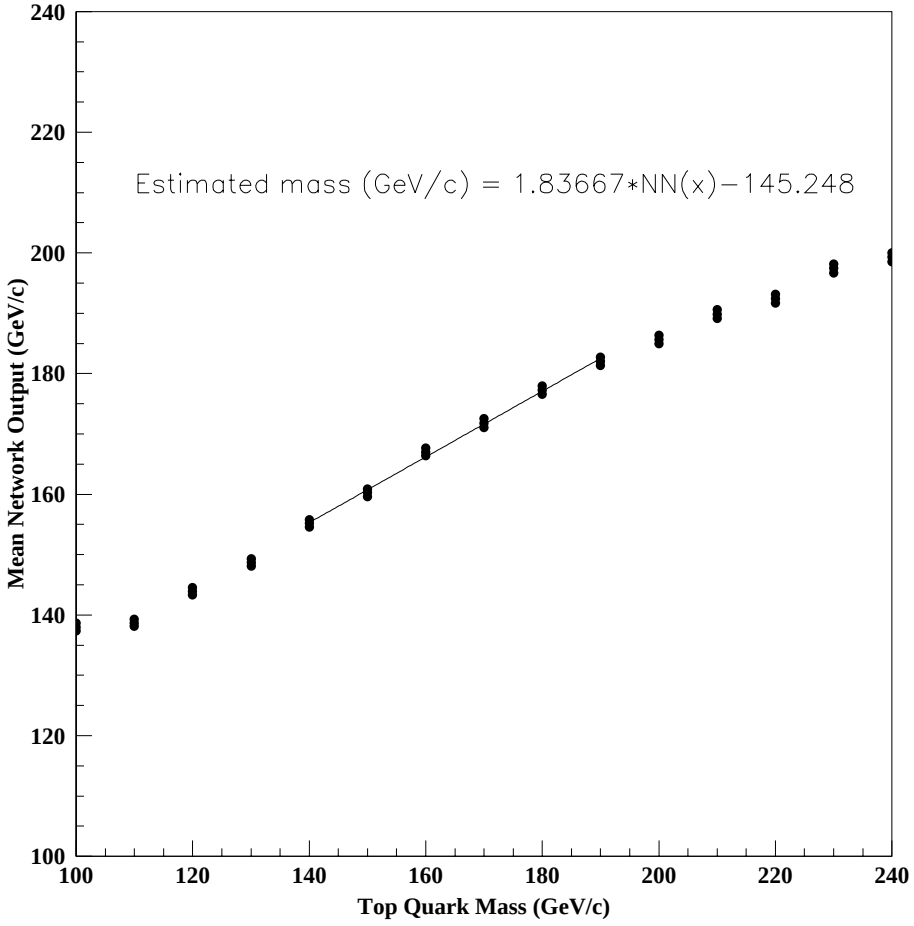

Figure 9.2: The mean of the distribution of network output as a function of the top quark mass. The expression shown is the linear correction function derived from the fit.

For a single measurement the method seems to be biased. However, the relevant issue is not the bias for a sample of size one but rather the magnitude of the root mean square (RMS) difference between the true mass and the measured mass for a sample whose size is likely to be much greater than one, and perhaps as large as 100 which will be the case in DØ Run II. However, we have assumed that a lack of bias for a single measurement is desirable. The simplest way to achieve this is to apply a linear correction, shown in Figure 9.2, to the network output (*i.e.* the posterior mean). After applying such a correction, we obtained the distributions shown in Figure 9.3. It shows the distributions of the estimated top quark mass for total background ($Z\tau\tau$ and WW) and MC samples for different top quark mass. RMS on each distribution corresponds to the uncertainty for each MC sample. These measurements are based on a single $e\mu$ event. The results are published in [57] and [58].

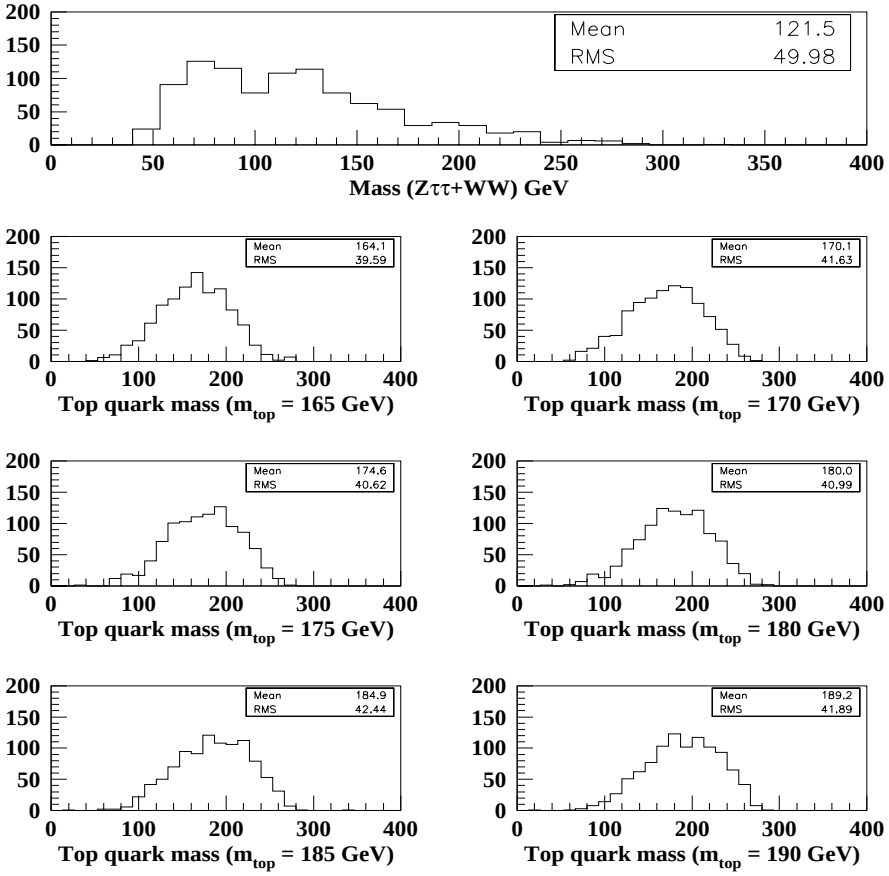

Figure 9.3: Distributions of estimated top quark mass for total background ($Z\tau\tau$ and WW) and MC samples for different top quark mass. RMS on each distribution is the estimated uncertainty for a single unbiased measurement *i.e.* for a mass measurement based on a single $e\mu$ event.

9.1.2 Run I Data Analysis using NN

We have used DØ Run I data for total integrated luminosity of 108.3 ± 5.7 pb^{-1}. We have trained NNs on samples of signal and background events and then these networks are tested using independent data sets *i.e.* events which have not been used in training.

NN Training

We have studied the distributions of signal and background events for different variables, the effect of using different training schedules and finally selecting a set of training schedules that give us the better results to separate the signal from background. We prepared large samples of Monte Carlo ($t\bar{t}$, WW and Z) events using some loose cuts[1] so as not to bias the results. The simulation of MC samples is given in Sec. 6.3.3 (A). From this set of MC events, a small sub-sample of 3000 events were selected at random to provide the training sample for the $e\mu$ analysis in NN techniques. To make priori probability same for signal and background, we take 3000 pattern vectors (events) for the MC sample with a top quark mass of 170 GeV as signal and 3000 pattern vectors from background, which consists of 1500 pattern vectors from $Z \to \tau\tau \to e\mu$ and 1500 pattern vectors from $WW \to e\mu$. The network was then tested with an independent set of 5000 signal and background events. The relative significance $(S|B)$ was calculated for the signal and background events surviving the neural network.

The number of nodes and the input parameters for NN were selected to give the best discrimination between the signal and background. We have used six input nodes, seven hidden nodes and one output node for the NN. We have used only one hidden layer because it is sufficient for most classification problems [59]. To ensure convergence and stability, the total number of training patterns must be significantly larger ($\approx 20 - 40$ times) than the number of independent parameters of the NN. The input parameters used for the NN are :

- Azimuthal separation of the leading electron and muon, $\triangle\phi_{e\mu}$.
- Electron muon invariant mass, $M_{e\mu}$.
- Four vectors (x_1, x_2, x_3, x_4) defined as below

$$\begin{aligned} x_1 &= \sqrt{(2j_1 \cdot j_2)} \\ x_2 &= \sqrt{(2e \cdot j_1 + m_W^2)} \\ x_3 &= \sqrt{(2e \cdot j_2 + m_W^2)} \\ x_4 &= H_T(E_T^e + \sum_{\text{all jets}} E_T^{jet}), \end{aligned}$$

[1]Particle id cuts, $E_T^e \geq 10$ GeV, $P_T^\mu \geq 10$ GeV and $N_{jets} \geq 1$ with $E_T^{jet} \geq 10$ GeV.

Figure 9.4 shows the comparisons of the variables for MC sample of $t\bar{t} \to e\mu$ with top quark mass of 170 GeV and backgrounds : both WW and $Z \to \tau\tau$ backgrounds. The network is trained for 2000 training cycles. We varied number of training cycles from 50 to 3000 to investigate the effect of training on network performance. At 2000 training cycles, the network performance was found to be stable. Training started with a set of random weights and thresholds. The learning rate η is a factor in updating the weights and for our analysis we have chosen it to be 0.02. A momentum term α which typically varies between 0 ans 1, can be used to stabilize learning and speed up convergence. We have chosen a value of 0.5 for momentum term.

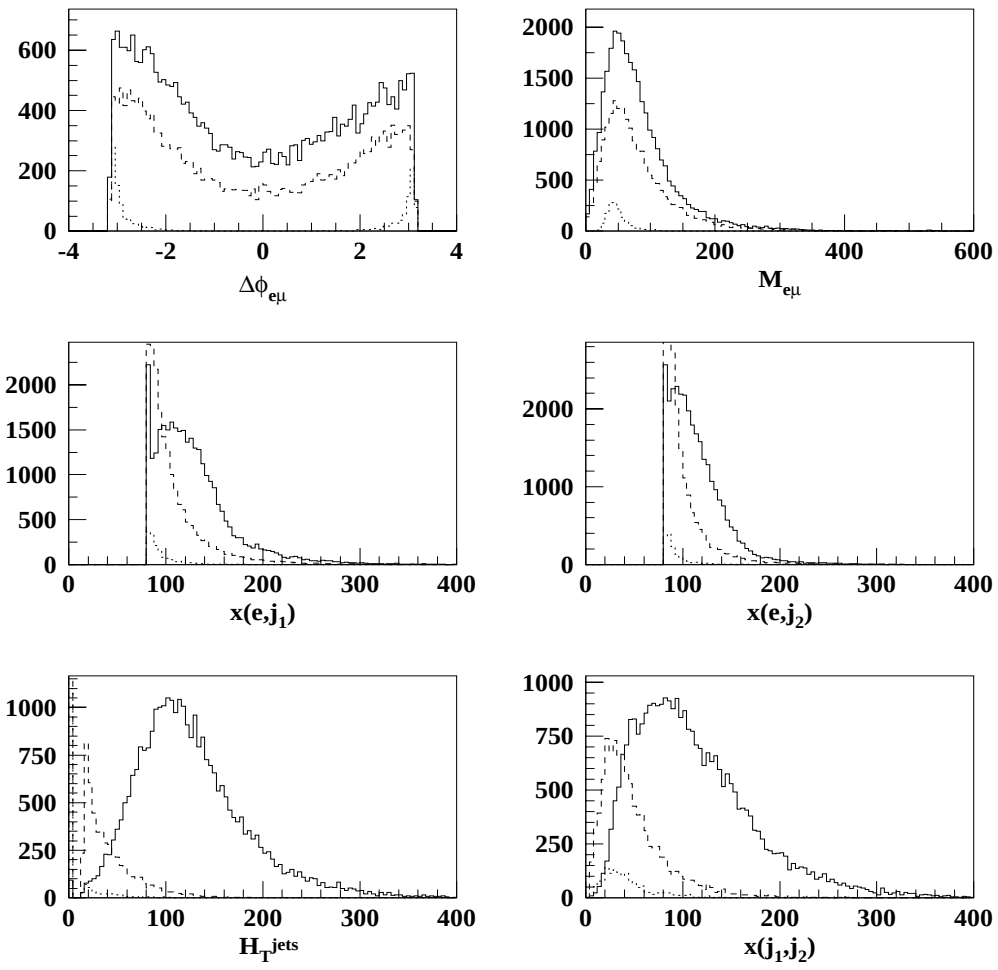

Figure 9.4: Distributions of the variables used for $t\bar{t}$ signal (solid) and ($Z\tau\tau$ -dotted and WW -dashed) backgrounds in NN.

NN Testing

To test the trained network, we have passed independent events through the network *i.e.* the events which were not used in training. An output was provided for each event which can be considered as the probability of that event being either signal or background. If the training has been done correctly, the probability for an event being signal is high and the output is close to 1 and for the event being a background, the output is close to 0.

Besides electron id and muon id cuts used for Run I, which are same as that of conventional cuts, the summary of cuts applied is :

- $E_T^e \geq 15$ GeV, $p_T^\mu \geq 15$ GeV
- $\triangle R_{\mu,e} \geq 0.25$, $\triangle R_{\mu,jets} \geq 0.5$
- $\not\!\!E_T{}^{cal} > 15$ GeV
- $N_{jets} \geq 2$ with $E_T^{jets} \geq 15$ GeV and $|\eta^{jet}| \leq 2.5$
- Neural Network cut NN≥ 0.90

The network was trained to the top quark mass of 170 GeV. To test the sensitivity, we have used the network trained on 170 GeV events on different MC samples for top quark mass. The results are as shown in Figures 9.6 and 9.7. From these figures it is clear that our NN is correctly trained. The NN cut has been chosen for the maximum S/B ratio at a given efficiency (times branching fraction). After all the cuts, only *four* events remain.

As mentioned in Sec. 8.4, we are left with 3 top $e\mu$ events by using "conventional analysis". In NN analysis, as clear from the Figure 9.9, we are left with 4 top events which are the 3 $e\mu$ candidates selected from the data by conventional analysis and an additional event (event numbered 5566) which survives only in NN analysis. This was rejected in the conventional analysis because it failed the H_T^e cut. It satisfies all the selection criteria and kinematically lies in the part H_T^e and $\not\!\!E_T{}^{\rm cal}$ plane which is recovered by the NN analysis [29].

9.1.3 Analysis and Results

Therefore, we see that only 4 top $e\mu$ events in Run I data of total integrated luminosity of 108.3 ± 5.7 pb^{-1} are left. To determine the top quark mass using these final events left, the method adopted is same as for simulated data as mentioned in Sec. 9.1.1. To measure the top quark mass, we have used mass dependent quantities that are not derived from kinematic fits. The feature vector $\vec{x}$ used in our analysis is as :

$$\vec{x} = [x(e, j_1), x(e, j_2), x(j_1, j_2), H_T^{jets}, \triangle\phi_{e\mu}, M_{e\mu}] \tag{9.3}$$

Each class labeled as k is associated with a top quark mass m_k, and then the $P(k|\vec{x})$ has been interpreted as the probability that the top quark mass is m_k. The

posterior mean is estimated using a (6,7,1) NN. During training, the target value is set equal to the top quark mass m_k, ($m_1 = 165, m_2 = 170, m_3 = 175, m_4 = 180, m_5 = 185, m_6 = 190$ GeV) associated with the feature vector $\vec{x}$. Three thousands (3000) feature vectors have been used for each top quark mass and for training of the NN we have used MLPfit program.

The mean of the network output distributions (*i.e.* the mean of the distribution of the posterior mean) is determined. As mentioned in Sec. 9.1.1, the curve is non-linear out side the range of $140 - 190$ GeV as shown in Figure 9.2 and a linear correction is applied to the network output (*i.e.* the posterior mean). After applying the correction we obtain the distribution shown in Figures 9.8 and 9.9. The RMS on each distribution shows the uncertainty on that particular MC sample of top quark mass. The uncertainties are in the range 56 - 59 GeV. These results are for the single unbiased measurement and for the case, *i.e.* DØ Run II, the top events would be 10 times more and these uncertainties would reduced by the factor of $\sqrt{30}$.

The systematic uncertainty in our measurement of the top quark mass comes out to be 2.17 GeV. The procedure adopted to determine this systematic uncertainty is outlined in Sec. 9.3.

The Figure 9.5 shows comparison of the discriminant distribution for the signal and total background ($WW + Z\tau\tau$) test samples.

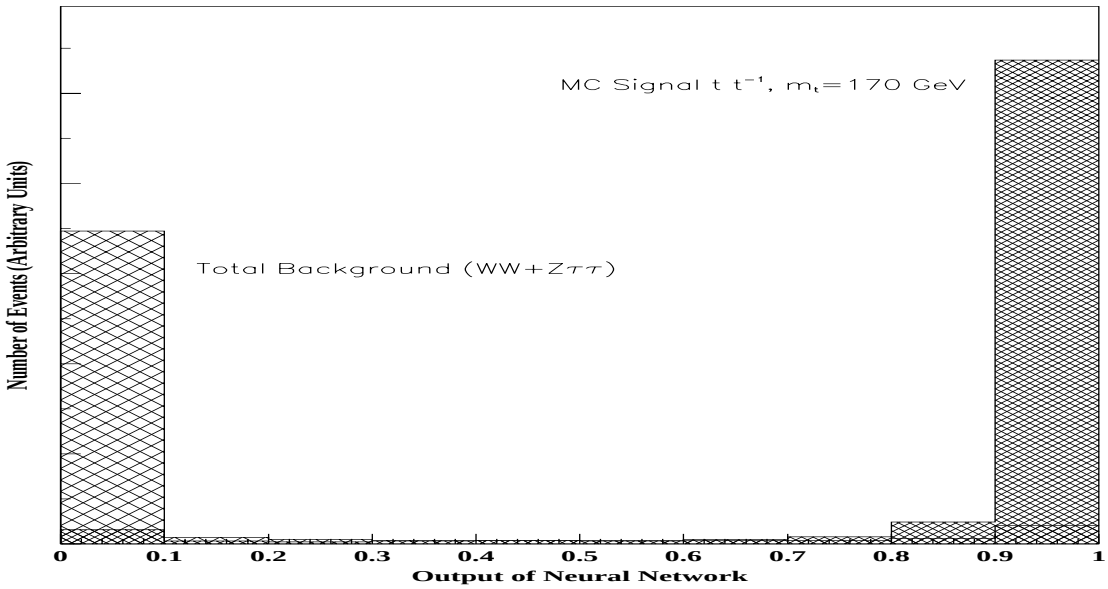

Figure 9.5: The distribution of total background and signal as a function of neural network output.

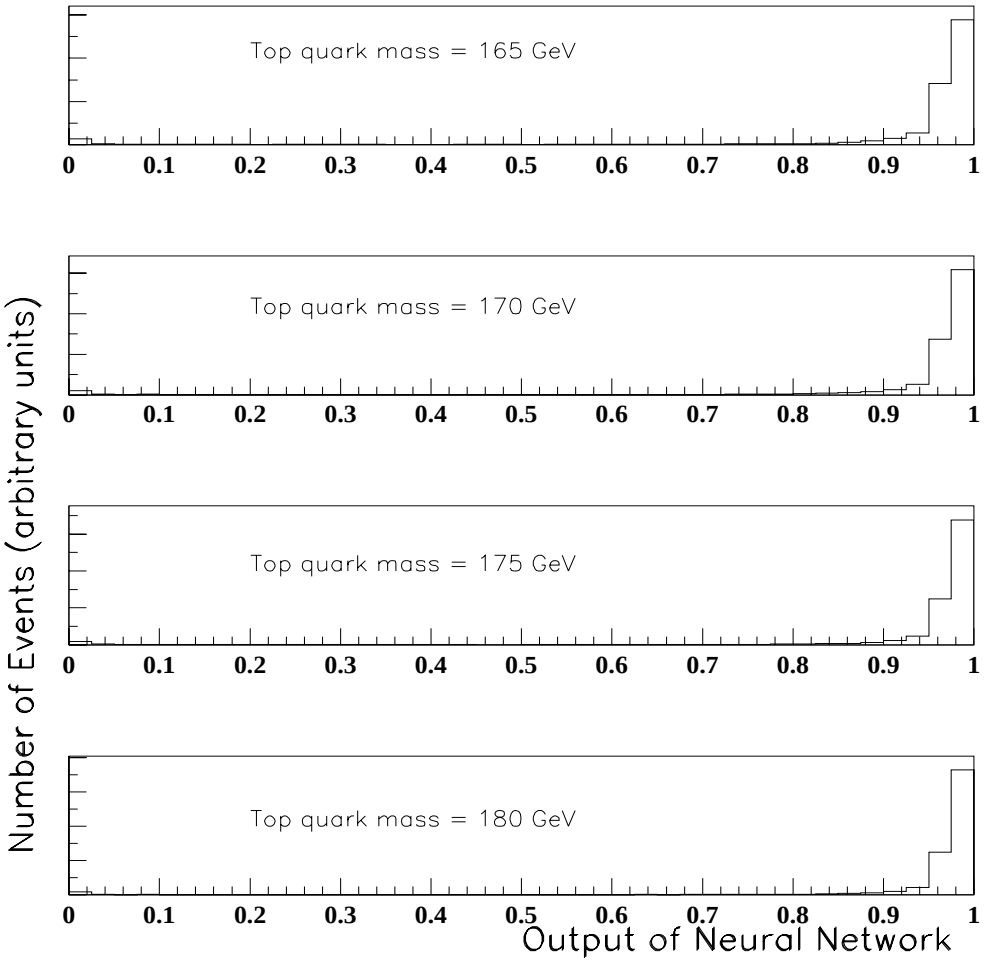

Figure 9.6: The distributions of signal (m_t = 165, 170, 175 and 180 GeV) as a function of neural network output.

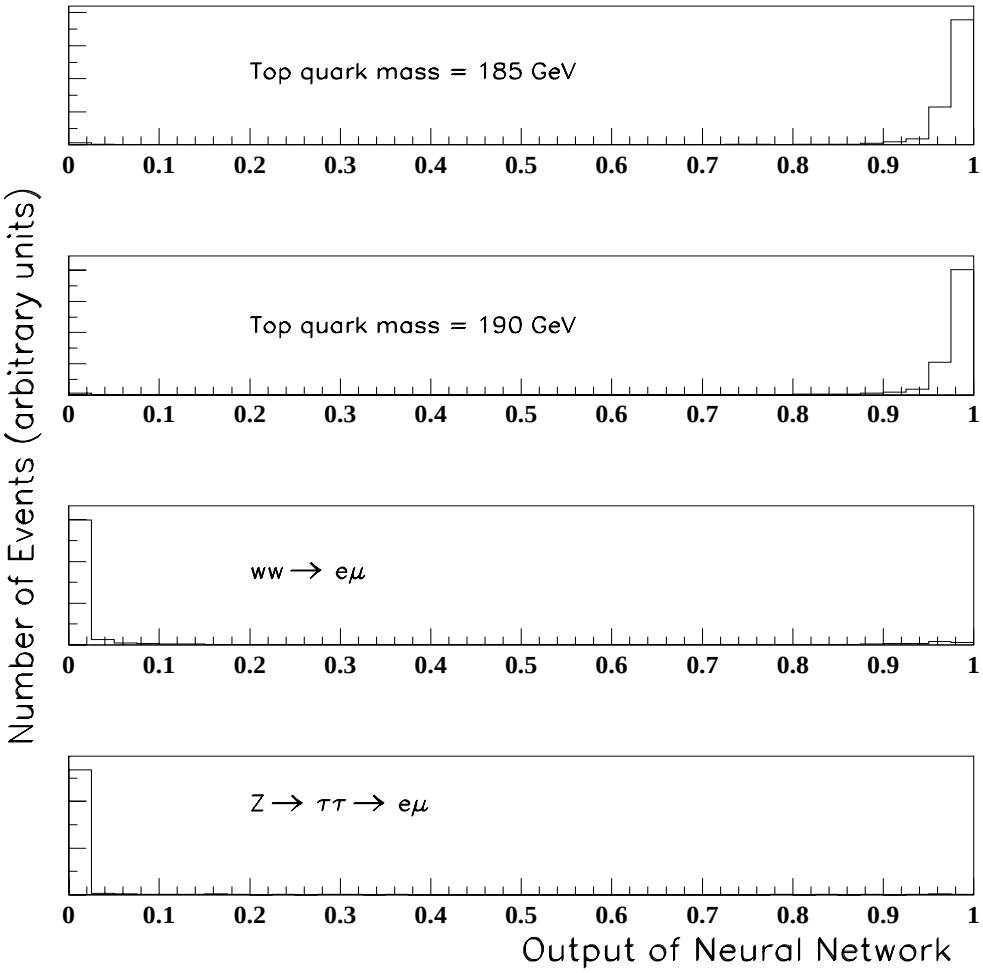

Figure 9.7: The distributions of signal (m_t = 185, 190 GeV) and background (WW and $Z\tau\tau$) as a function of neural network output.

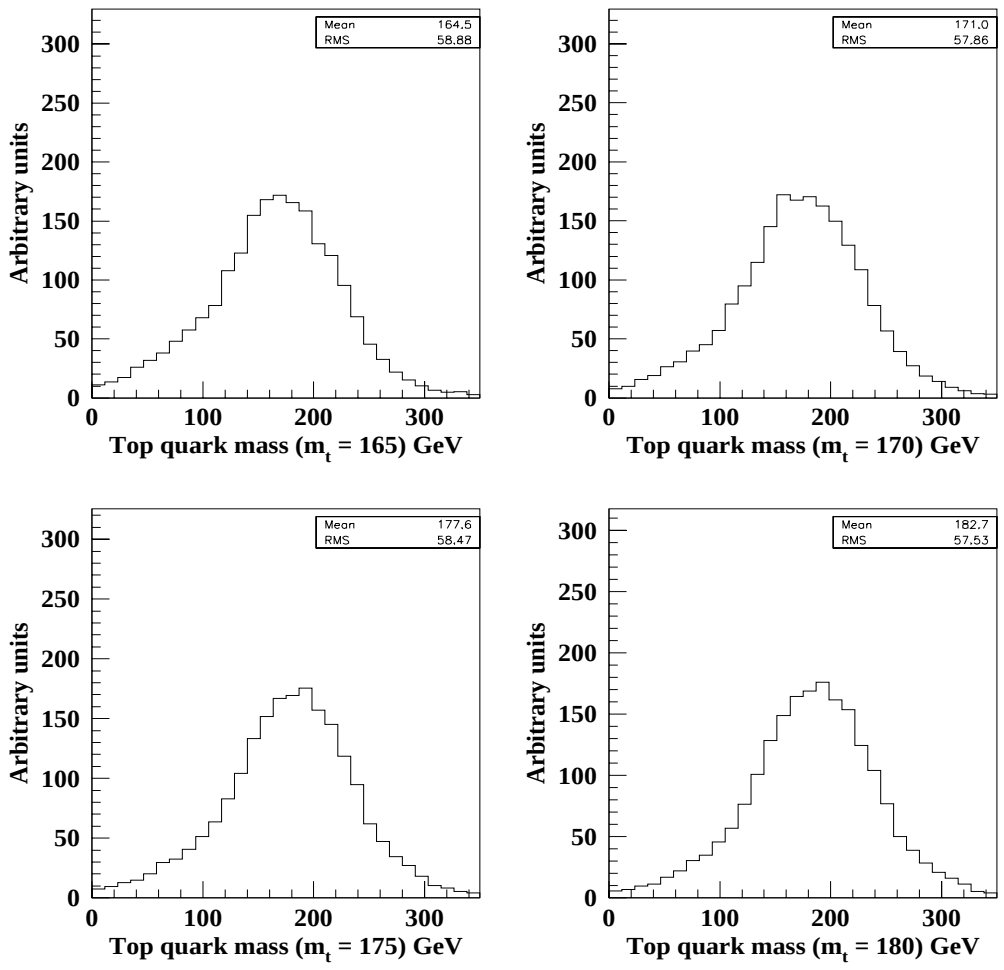

Figure 9.8: Distributions of the estimated top quark mass for MC sample of mass 165, 170, 175 and 180 GeV for a single unbiased measurement.

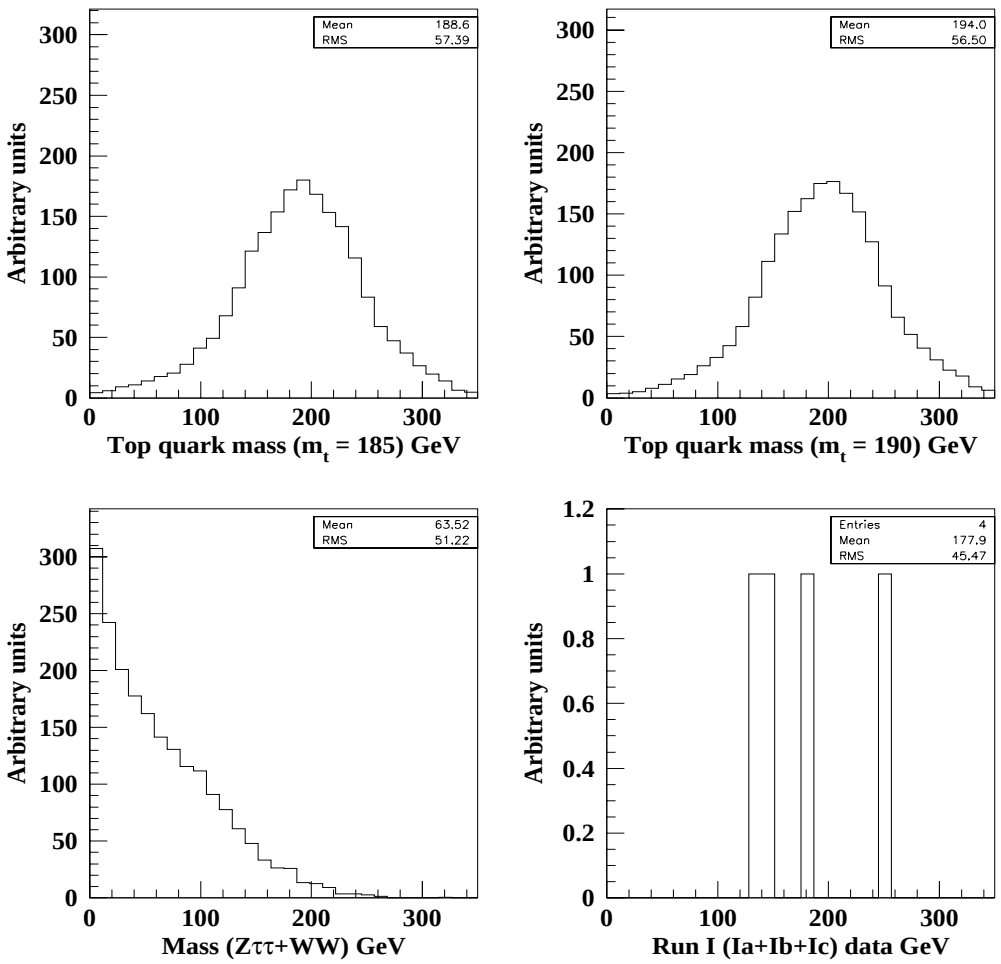

Figure 9.9: Distributions of the estimated top quark mass for MC sample of mass 185, 190 GeV, total background and total Run I data.

9.2 Method of Four Vectors

As explained in Sec. 8.5.6, the method of four vectors is based on the mass dependent quantities (x_1, x_2, x_3, x_4) defined in Eqns. 8.29 - 8.32 which are the four vectors of the electron and two highest transverse momentum jets.

The dependence of the mean values of variables $x1, ..., x4$ on the top quark mass is studied for the MC samples. For the final estimate of the top quark mass of the $e\mu$ candidates in Run I data, the weighted average of the mass estimates from these four vectors is taken.

9.2.1 Data Sets

Signal Monte Carlo

The event samples ($t\bar{t} \to e\mu$) for six different top quark masses (165, 170, 175, 180, 185 and 190 GeV) have been used in the analysis of four vectors. The initial number of events (N_{events}) in these six MC samples are given in Table 9.1 below :

MC Sample (GeV)	N_{events}
165	102434
170	101339
175	103124
180	103047
185	103078
190	103036

Table 9.1: The initial number of events in signal MC samples.

Background Monte Carlo

We have studied the two major backgrounds in the $e\mu$ channel : $Z \to \tau\tau \to e\mu$ and $WW \to e\mu$. The initial number of events for the backgrounds $Z\tau\tau$ and WW are 71393 and 101792 respectively.

The signal ($t\bar{t} \to e\mu$) and background modeling has already been explained in Sec. 6.3.

$e\mu$ Data Set

We have used Run I DØ data for total integrated luminosity of 108.3 ± 5.7 pb^{-1}. Besides applying the trigger cuts as explained in Sec. 6.1, we have optimized the kinematical (selection) cuts to reduce the backgrounds while maximizing the top

signal detection efficiency (to have a good signal to background ratio). The event selection criteria finally applied is :

(i) Require Isolated muons, $\Delta R_{\mu,jet} \geq 0.5$

(ii) $\not\!\!E_T > 10$ GeV (muon corrected)

(iii) $\not\!\!E_T{}^{cal} > 20$ GeV (calorimeter)

(iv) $\Delta R_{e\mu} > 0.25$

(v) Require 2 jets, $E_T^{jet} > 15$ GeV

(vi) H_T $(E_T^e + \sum_{alljets} E_T^{jet}) > 120$ GeV

After applying all the cuts (trigger+selection cuts), we are left with 3 $e\mu$ candidate events. The event yields for MC (signal and background) and data are given in Sec. 8.4.

The same cuts except the object identification (ID) and trigger cuts are applied to the MC samples.

Data vs Monte Carlo Models

In order to assess how well our Monte Carlo model agrees with the data, we fitted a weighted sum of signal and background distributions to the corresponding distribution for data using a Bayesian method [69]. The results from the fits agree with what we expect from the assumed cross sections for Z and WW. One such fit is shown in Figure 9.10, which shows reasonable agreement between the Monte Carlo background model and the data. As expected, actual data is comprised of signal and background (in which most of it is background), and this is clear from the Figure 9.10 also.

Final Sample

The Bayesian fit to data gives :

$$n_{Z\tau\tau} = 30.3^{+9.2}_{-8.4} \text{ events}$$

and

$$n_{WW} = 83.7^{+10.7}_{-10.0} \text{ events},$$

which yields estimates of the number of background events in 108.3 ± 5.7 pb^{-1}, for $WW \to e\mu$ and $Z \to \tau\tau \to e\mu$, of 0.20 and 0.001 events, respectively, to be compared with the 3 data events that survive the cuts.

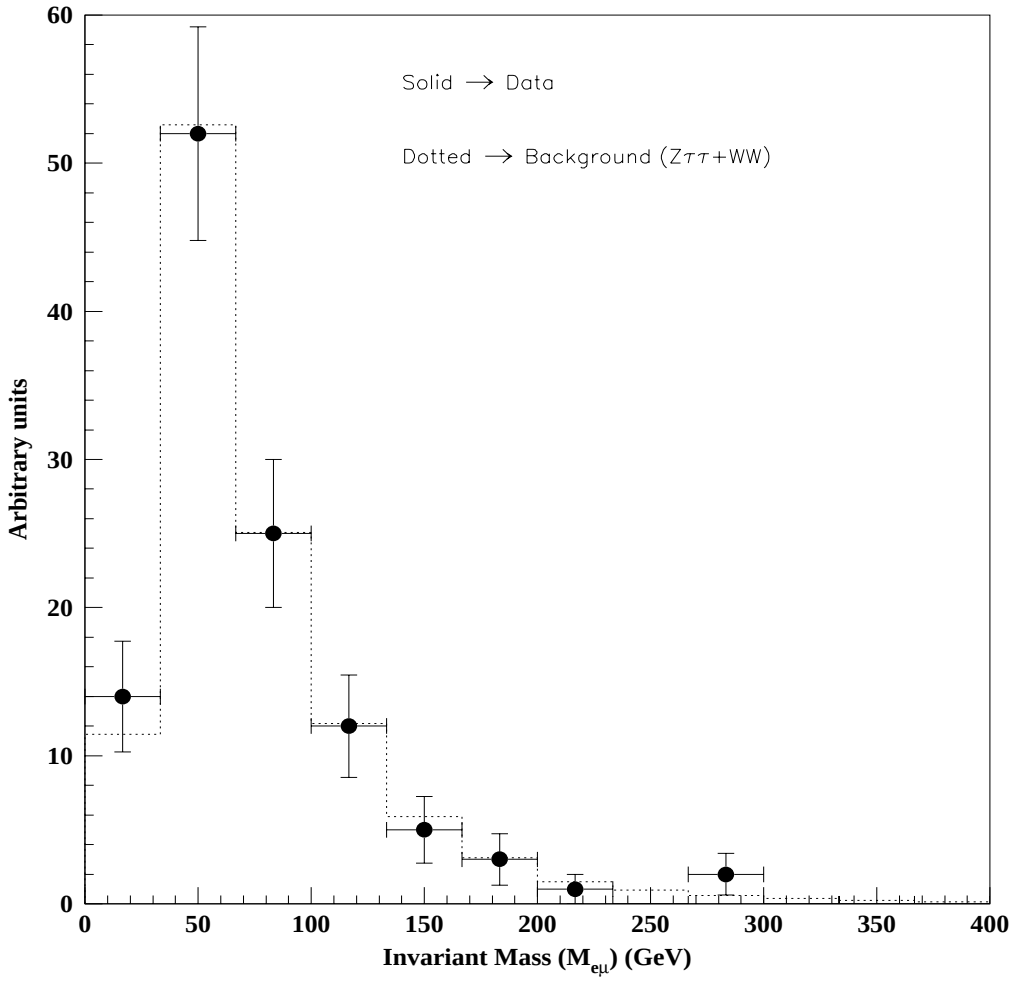

Figure 9.10: Bayesian fit of signal + background.

9.2.2 Analysis

Monte Carlo

We have used six MC samples of different top quark masses. The distributions of some of the variables which have been used in our analysis for MC sample of top quark mass 180 GeV are shown in Figure 9.11.

The variables are E_T and ϕ for the leading electron and leading muon (E_T^e, p_T^μ, ϕ_e and ϕ_μ), the number of jets (N_{jets}), the invariant mass ($M_{e\mu}$) of the $e\mu$ pair and the azimuthal separation between the leptons, $\triangle\phi_{e\mu}$. Using these mass dependent quantities, four vector in our case, *i.e.* $x1, ..., x4$ have been determined according to Eqns. 8.29 - 8.32. It has been observed that the mean values of these variables depend linearly on the top quark mass as shown in Figure 9.12. Therefore, we can write four equations of the form

$$m_i = s_i \bar{x}_i + c_i \tag{9.4}$$

where m_i is the mass estimate, s_i is the slope, c_i is the intercept and $\bar{x}_i$ is the mean of observable x_i. These linear functions have been deduced from the Monte Carlo (MC) calculations. The distributions of four vectors for MC sample of mass 180 GeV are shown in Figure 9.13.

Data

After applying the final selection cuts to Run I data, in conventional $e\mu$ analysis we are left with 3 top events. From a sample of these 3 $e\mu$ candidates again the four vector $x1, ..., x4$ have been determined for each event separately. We have then, computed the mean values of $x1, ..., x4$ and inferred from each quantity a top quark mass using Eqn. 9.4. Hence, we have four estimates, $m_1, ..., m_4$, for a top quark mass. The values of $x1, \cdots, x4$ obtained thus for these 3 $e\mu$ events are given in Table 9.2 and the corresponding distributions are shown in Figure 9.14.

Observable	Event1 (GeV)	Event2 (GeV)	Event 3 (GeV)
$x1$	53.88	44.70	104.34
$x2$	118.02	151.13	162.03
$x3$	94.17	169.81	118.12
$x4$	148.74	123.58	231.22

Table 9.2: The values of the four vectors $x1, ..., x4$ for the 3 $e\mu$ events left in Run I Data.

As our final estimate of top quark mass, we have taken the weighted average of these four mass estimates according to Eqn. 8.35. Our overall weighted top quark mass estimate using the 3 $e\mu$ events comes out to be 137.7 GeV. The number of background events in 108.3 ± 5.7 pb^{-1} for $WW \rightarrow e\mu$ and $Z \rightarrow \tau\tau \rightarrow e\mu$ comes out to be 0.20 and 0.001 respectively. Since background as already mentioned is negligible, so no correction is needed for it. However, in case where background is considerable one needs to correct x_i.

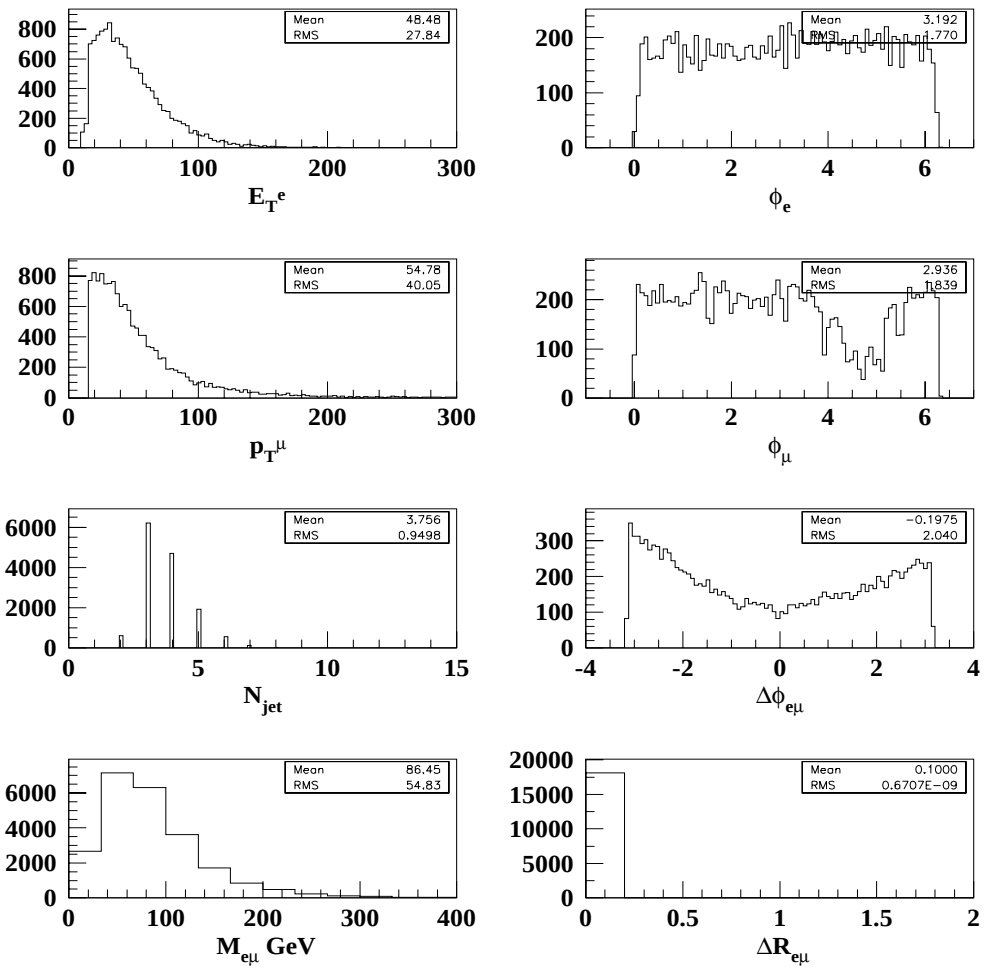

Figure 9.11: Distributions of some of the variables for MC sample for mass 180 GeV.

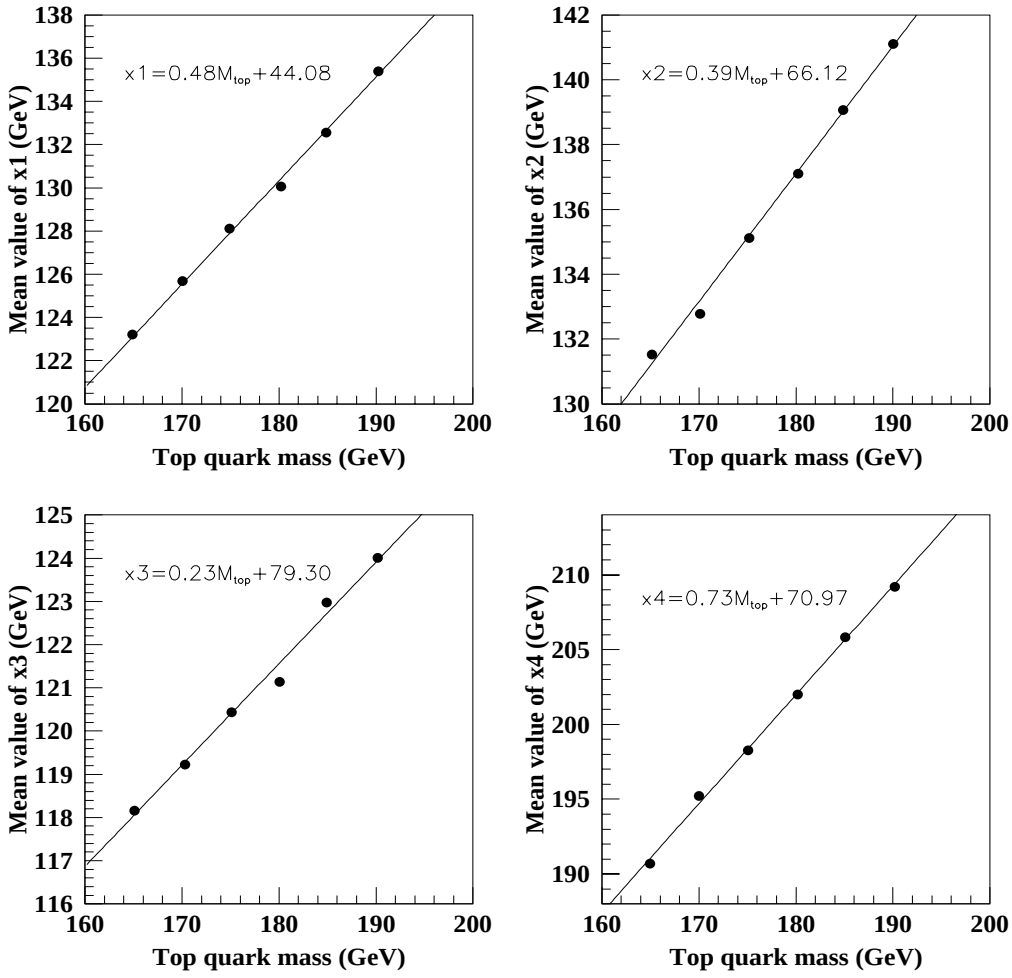

Figure 9.12: Dependence of the mean value of the four vectors on the top quark mass.

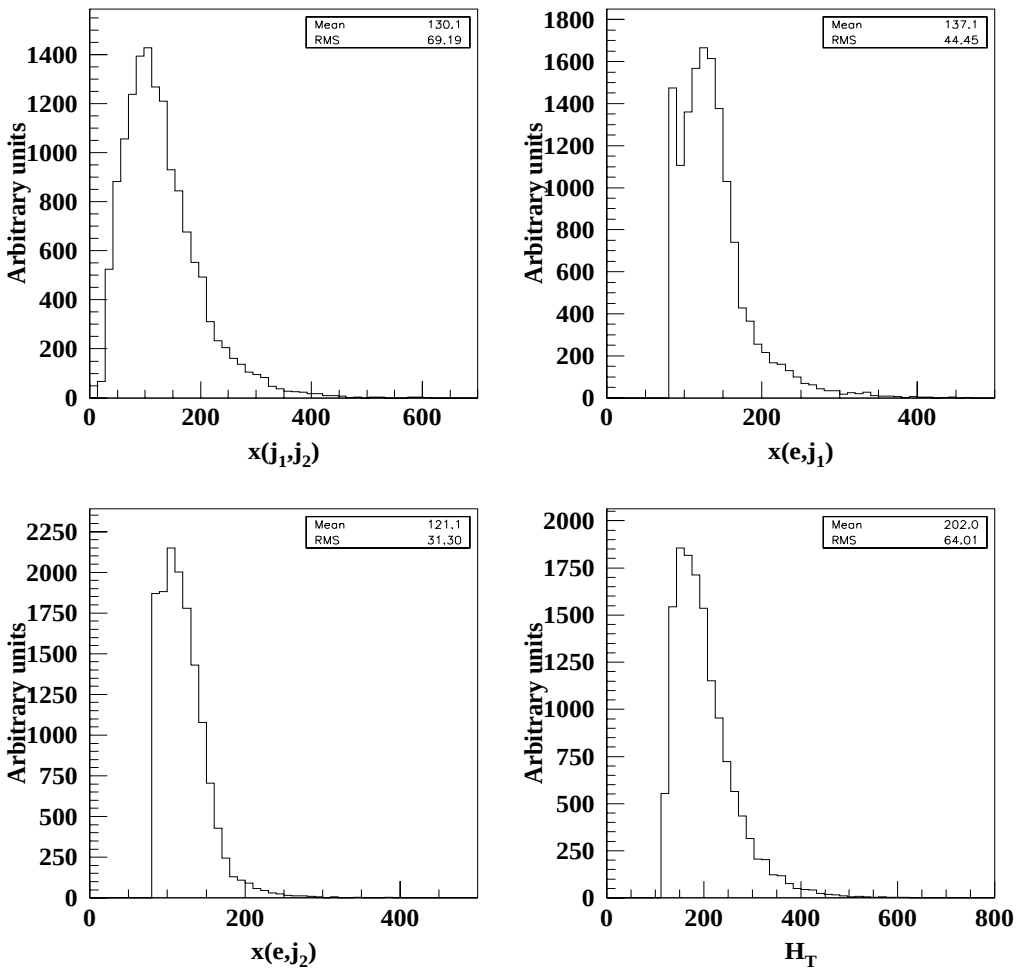

Figure 9.13: Four vector distributions for the MC sample for mass 180 GeV.

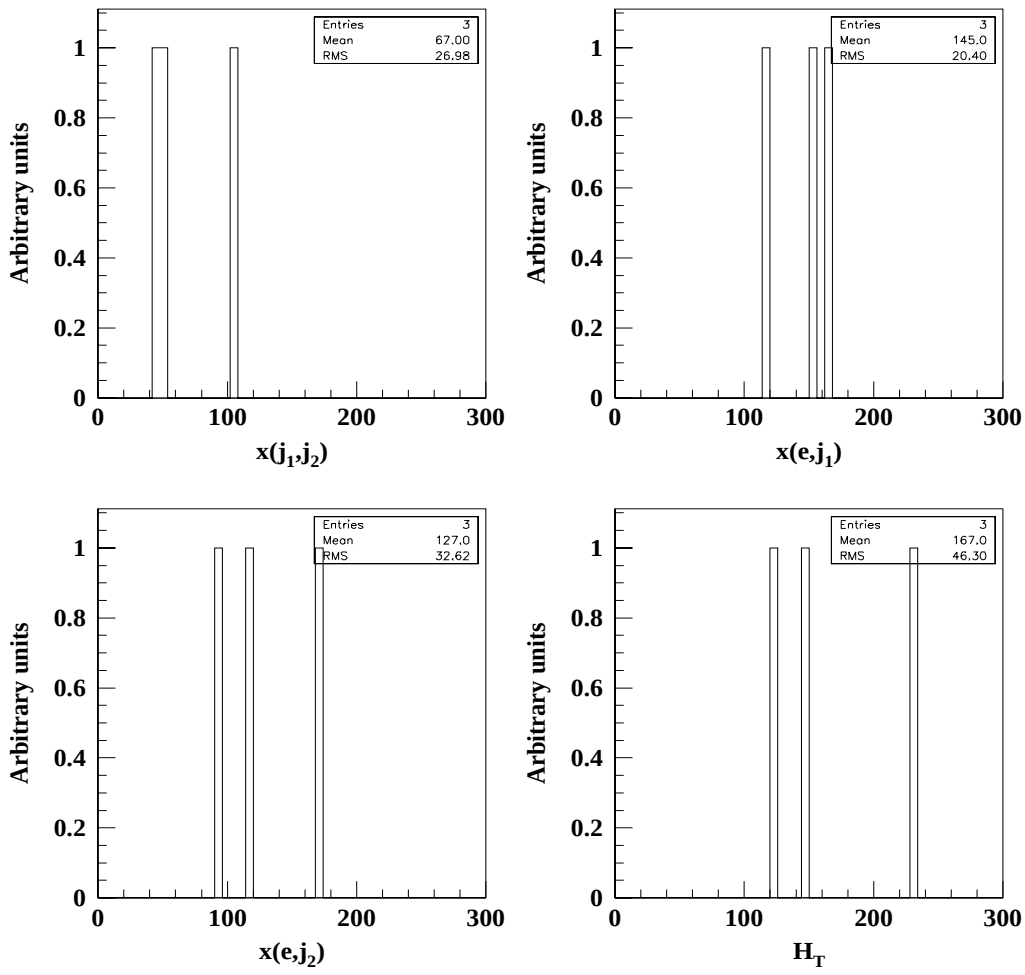

Figure 9.14: Four vector distributions for the $e\mu$ events finally left.

9.3 Systematic Uncertainty

We have studied the systematic uncertainty in the measurement of our weighted top quark mass. Various sources of systematic errors can be found in [29].

The most effective systematic uncertainty in the top quark mass measurement arises from uncertainty in our knowledge of the MC Jet Energy Scale which arises from our imprecise knowledge of the energy scale of jets in MC events. To be very precise, we have studied this systematics for method of four vectors here.

The jet energy scale in DØ was established using γ+jets events as follows :

- The hadronic scale was set using the well-calibrated energy scale of the DØ electromagnetic calorimeter by balancing the transverse momenta of the photon and the jet over an ensemble of such events.

- The MC hadronic scale was set by comparing γ+jets MC events with corresponding collider events and adjusting the scale of the former until it matches that of the later. The jet energy scale uncertainty is the uncertainty in how well the two scales match.

This procedure yielded an uncertainty of $\delta(E_T) = 0.025E_T + 0.5$ GeV [70]. In order to propagate this uncertainty to the measured top quark mass, one generates MC samples with the jet energies moved up and down by δ *i.e.* by $\pm\delta$ to rescale the E_T of MC jets and then the variation in the measured mass is assessed. However, in the absence of a sound principle, we can not assess these variations completely. We have adopted a Bayesian theory to extract a systematic uncertainty, given three estimates of the top quark mass $\hat{m}(+\delta)$, m and $\hat{m}(-\delta)$.

Using the procedure outlined below in Sec. 9.3.1, the systematic uncertainty in our measurement of the top quark mass usingmethod of four vectors comes out to be 1.52 GeV.

9.3.1 Bayesian Theory

Given data D, an analysis procedure yields an estimate $\hat{m}$ of the top quark mass m_t. The relationship between the data D and the true mass m_t is a probability, [71]

$$P(D|m_t) = f(D|m_t)dD \tag{9.5}$$

where $f(D|m_t)$ is the probability density function associated with the data D. The probability $P(D|m_t)$ is that of getting data D given the top quark mass m_t. We can write

$$L(m_t) \equiv f(D|m_t) \tag{9.6}$$

where, $L(m_t)$ is called the *likelihood*. It is the probability density function $f(X|m_t)$ evaluated at the observed data $X = D$. In our method of four vectors, D is the four vector $(x1, ..., x4)$.

From Bayes theorem, we have

$$\text{Post}(m_t|D) \propto L(m_t)\text{Prior}(m_t) \tag{9.7}$$

where $Post(m_t|D)$ is the *posterior probability i.e.* the probability of different hypotheses about the true value of the top quark mass m_t given an observed set of data D. The quantity $\text{Prior}(m_t)$ is the probability of different hypotheses about the top quark mass is the absence of the data D. We obtain a mass estimate $\hat{m}(D)$ from $\text{Post}(m_t|D)$, typically, by calculating its *mode* or its *mean*.

In the mass analysis, these probabilities depend on E_T of the jets in the MC events. If E_T denotes all the MC jet transverse momenta on which the probabilities depend, then we can write

$$\text{Post}(m_t, E_T|D) \propto L(m_t, E_T)\text{Prior}(m_t)\text{Prior}(E_T) \tag{9.8}$$

where we have assumed that the prior probabilities factorize into a term for m_t and one for the set of jet transverse energies E_T. The quantity $\text{Prior}(E_T)$ describes, as a probability distribution, the systematic uncertainty in the jet energy scale. To take account of the jet energy scale systematic uncertainty we merely *marginalize* (integrate) $\text{Post}(m_t, E_T|D)$ over the set of jet E_T,

$$\text{Post}(m_t|D) = \int_{E_T} \text{Post}(m_t, E_T|D), \tag{9.9}$$

i.e. over all possible hypotheses about the true value of the jet transverse momenta in MC events.

In practice, for computational simplicity, the transverse energy of jets in MC events is rescaled by $\pm\delta$. Therefore, the integral over MC jet E_T becomes a sum with only three terms : one with E_T scaled down by δ, one with the nominal E_T and the third with E_T scaled up by δ :

$$\text{Post}(m_t|D) = A\sum_{E_T} \text{Post}(m_t, E_T|D), \tag{9.10}$$

where the normalization factor A is chosen so that $\int_{m_t} \text{Post}(m_t|D) = 1$.

We computed the mean and standard deviation of posterior probability $\text{Post}(m_t|D)$. The standard deviation σ' of $\text{Post}(m_t|D)$ has been taken as a measure of the uncertainty in the mass estimate $\hat{m}$ in the presence in the jet energy scale. The measure of the systematic uncertainty in the measured top quark mass can be given as :

$$\sigma_{syst.} \equiv \sqrt{\sigma'^2 - \sigma^2} \tag{9.11}$$

where σ is the standard deviation using only the nominal jet energy scale.

9.4 Results

In this section, we describe simple MC experiments that have been used to estimate the uncertainties in the estimates. We have used all the six top quark MC samples generated for $t\bar{t} \to e\mu$ decay. Since in Run I $e\mu$ analysis we finally have 3 top events, so for each top quark MC samples, we have generated many sub-samples of events whose size is fixed at the observed sample size *i.e.* 3 in our case. Each sub-sample is analyzed in the same way as the observed sample as explained in Sec. 9.2.2.

For each sub-sample of size 3, we have calculated the mean corresponding to each four vectors $x1, ..., x4$. Using the linear functions from Eqn. 9.4, we have calculated $m_1, ..., m_4$. The distributions of the top quark masses $(m_1, ..., m_4)$ from each of the four variable $(x1, ..., x4)$ respectively for a sub-sample of 3 events for MC sample of 180 GeV are shown in Figure 9.15. So, again to get the estimate of the top quark mass the weighted average has been determined using Eqn. 8.35. The distributions of the weighted top quark mass have been obtained and the measure of the standard deviation (or RMS) of this distribution gives the uncertainty in the top quark mass. The distributions of the weighted top quark mass for a sub-samples, each of 3 events, are shown in Figure 9.16.

Figure 9.15 shows that for the MC sample of 180 GeV, the mean $\pm$ rms of m_4 is 180.7 ± 50.87 GeV. We need the best way to combine $m_1, ..., m_4$. Although the precision of the other three estimates, m_1, m_2 and m_3 is worse, yet if $m_1, ..., m_4$ are properly combined the RMS of the weighted average mass should indeed be better than 50.87 GeV. As shown in Figure 9.16, the RMS for MC sample 180 GeV is 49.15 GeV which comes out to be better than 50.87 GeV. This is because of the fact that the weights in Eqn. 8.35 minimize the variance of the distributions when m_i are uncorrelated and hence the better results. Therefore, the weighted average is useful.

Using this method on Run Ib data only, results have been earlier published [72].

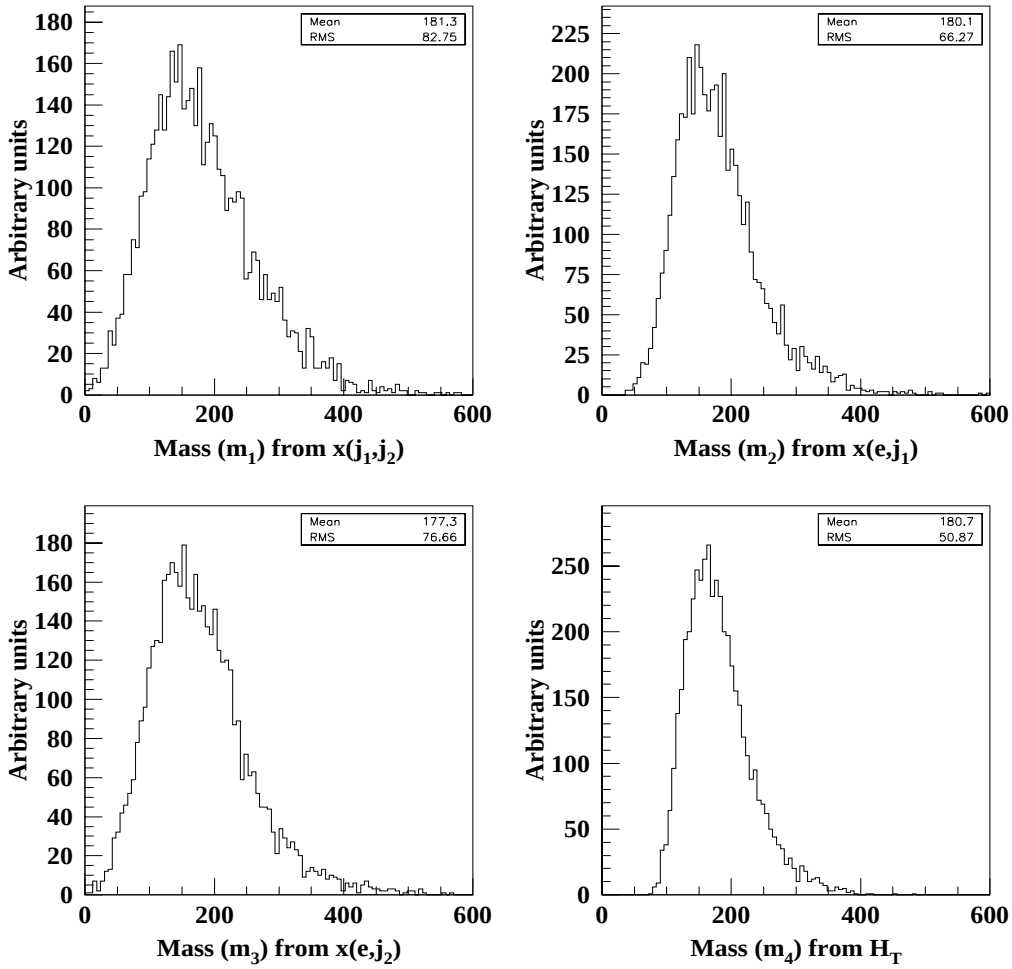

Figure 9.15: Distributions of the top quark mass from four variables for a sample of three events for $m_{top} = 180$ GeV.

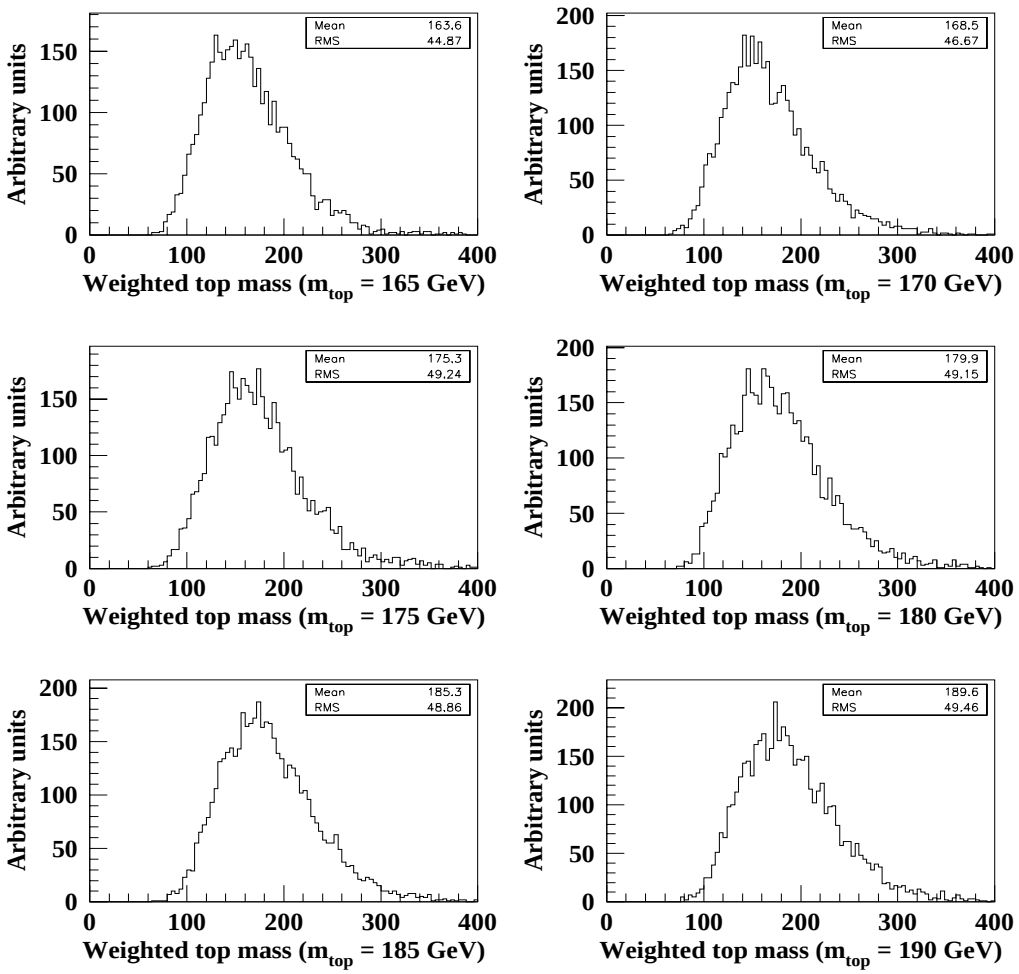

Figure 9.16: Distributions of the weighted top quark mass for a sample of three events for different MC samples.

The distributions in Figure 9.16 indicate the distributions of the weighted top quark mass for MC samples with a sub-sample of size 3. We see that we have devised a relatively simple method for the estimation of the top quark mass. Each distribution indicates the typical uncertainty in the mean of mass estimate. Estimated uncertainties ($\sim$ 45 - 49 GeV) as indicated are acceptable at this stage as we are devising a method which can be used with the larger data sets for DØ Run II or at LHC (CMS experiment) and also where the muon resolution will be equally good as electron resolution because of the central magnetic field. This method seems to be one of the simple/good methods which has a potential to be used for DØ Run II or at LHC (CMS experiment) where high statistics will be available.

To verify these facts, we have also tried to get the approximations for the uncertainties for Run II data. We have used the simulated events for $t\bar{t}$ signal and $Z\tau\tau$ and WW backgrounds for DØ detector for Run II at $\sqrt{s}$ =2 TeV as defined in Sec. 9.1.1. We have repeated the method of four vectors in three different cases as given below :

1. Using the same four vectors (x_1, x_2, x_3, x_4) for this simulated data (Sec. 6.3.3 (B)), the whole process was repeated. The distributions of the weighted top quark mass for a *single measurement* are shown in Figure 9.17. We see that our method works well and the uncertainties ($\sim$ 61 - 74 GeV) are in permissible range.

2. As already mentioned, the data has been simulated by considering that the muons have as good resolution as the electrons. Therefore, now we have taken the four vectors (x_1, x_2', x_3', x_4), the whole process was repeated and the corresponding distributions are shown in Figure 9.18. We see that RMS is considerably reduced.

3. We have compared the two methods, neural networks method and method of four vectors, by taking the similar four vectors *i.e.* $x(l, b)$ in both cases. So, in this case we have replaced the two vectors (x_2, x_3) by (x_2', x_3') which includes muon variables. The set of (x_1, x_2', x_3', x_4) is used in both methods. Neural network method gives the uncertainty in the range 40 - 42 GeV (Figure 9.3) and from method of four vectors, the uncertainty comes in the range 41 - 49 GeV (Figure 9.18). Comparison of Figures 9.3 and 9.18 show that the results are comparable and this method of four vectors also works well.

   In all the three cases, distributions correspond to *single measurement*. The uncertainties in them are acceptable at this stage which would reduce by a factor of $\sqrt{N}$ for actual Run II data where N would be quite large; about 100 times the Run I data. Therefore, the RMS will be reduced by a factor of $\sqrt{N}$ *i.e.* the uncertainty will be reduced in each case *e.g.* for the MC sample of 175 GeV the uncertainty will reduce to $\sim$ 4 GeV from the existing uncertainty of 39.15 GeV (see Figure 9.18).

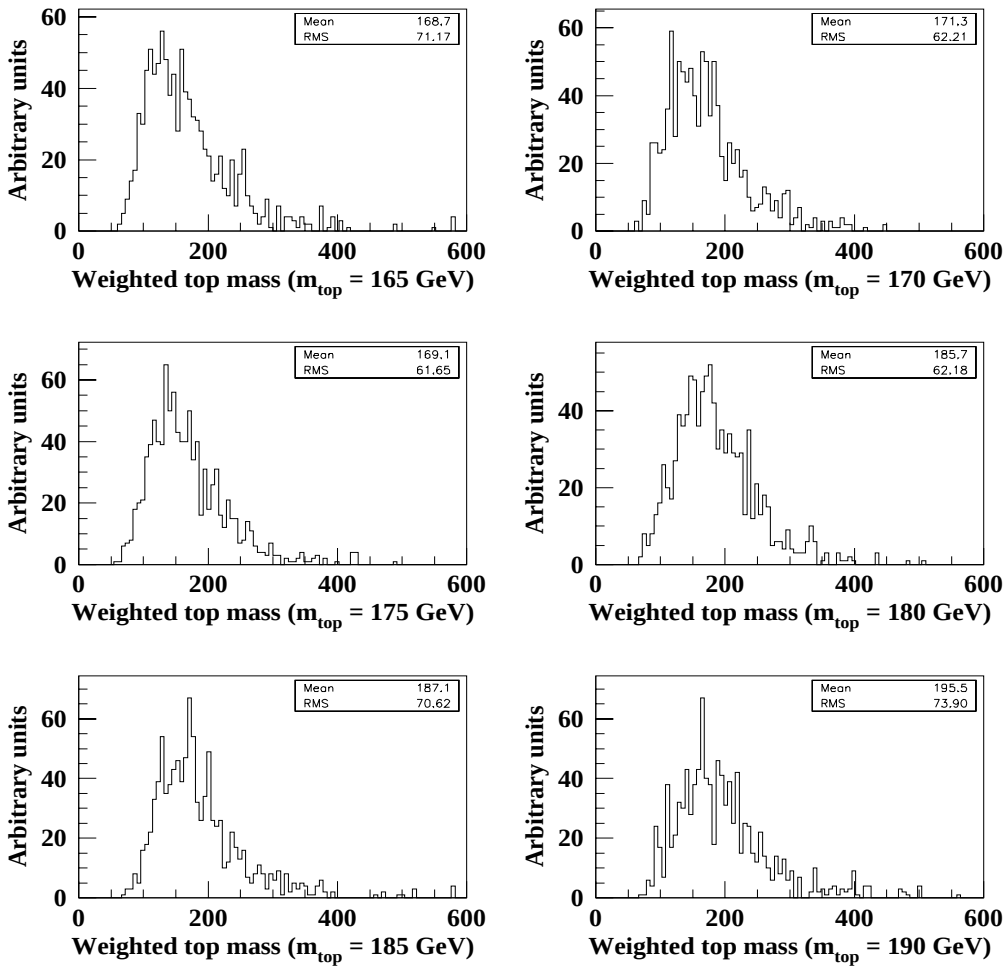

Figure 9.17: Distributions of the weighted top quark mass for a single measurement for different MC samples (Sec. 6.3.3 (B)) using $x_1, ..., x_4$.

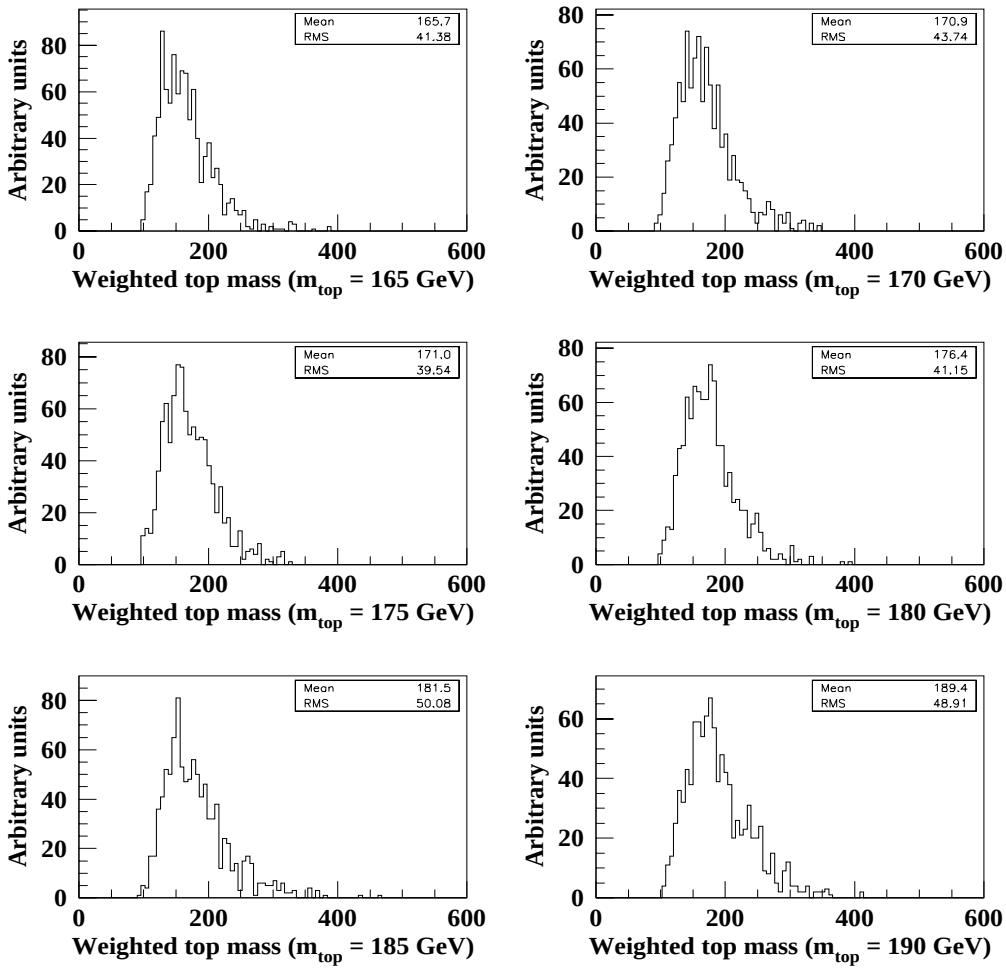

Figure 9.18: Distributions of the weighted top quark mass for a single measurement using variable $x(l, b)$ for different MC samples (Sec. 6.3.3 (B)).

9.5 Method of $e\mu$ Invariant Mass

As mentioned in the Sec. 9.1.1, our strategy to measure the top quark mass is to use mass dependent quantities which are not necessarily derived from kinematic fits. In this section, we discuss another approach for the estimation of top quark mass. In the study of $e\mu$ invariant mass, the top is partially reconstructed by taking the mass of an isolated $e\mu$ originating from W^+W^- decays and selecting the events with a minimum of two jets. $e\mu$ invariant mass, $\mathrm{M}_{e\mu}$, has been determined taking different MC samples of top quark mass. This is then correlated to the top quark mass as described below. Details of $t\bar{t}$ modeling have already been discussed in Sec. 6.3.3. This method relies on MC description of the top production and decay, however the model can be verified and tuned to the data.

The $\mathrm{M}_{e\mu}$ for different top quark masses (from MC samples) has been determined. The $\mathrm{M}_{e\mu}$ distribution for different top masses are shown in Figure 9.19 and it is observed that $\mathrm{M}_{e\mu}$ spectrum for each sample is consistent with a polynomial function of degree 6. The backgrounds $WW \to e\mu$ and $Z \to \tau\tau \to r\mu$ are also studied. It is observed that the backgrounds are almost negligible after applying the required kinematical cuts as mentioned in Sec. 8.3. The solid portion in the distributions in Figure 9.19 (a-c) corresponds to the total background.

To measure the top quark mass, the *central value*[2], for each of this distribution is determined. In our analysis we take the *median* of the distribution as the central value of the $\mathrm{M}_{e\mu}$ distribution and it is denoted as $\mathrm{M}_{e\mu}^{\mathrm{ave}}$. The measurement of the $\mathrm{M}_{e\mu}^{\mathrm{ave}}$ is then related to the top quark mass. The sensitivity of $e\mu$ invariant mass with the top quark mass has been studied. The correlation between $\mathrm{M}_{e\mu}^{\mathrm{ave}}$ and M_{top} is studied and the linear relation is observed between the two, as shown in Figure 9.19 (d) and is given as :

$$\mathrm{M}_{e\mu}^{\mathrm{ave}} = 0.203\mathrm{M}_{\mathrm{top}} + 43.17 \tag{9.12}$$

When determining the top quark mass, the statistical error in $\mathrm{M}_{e\mu}^{\mathrm{ave}}$ measurement would scale up as the inverse slope value of the fit which is 5 in our case. Table 9.3 shows the $\mathrm{M}_{e\mu}^{\mathrm{ave}}$ and statistical error on the mean value of each MC sample we have used. Hence, the statistical error on the top quark mass in our case would be ~ 2 GeV. The expected systematic error in the $\mathrm{M}_{e\mu}^{\mathrm{ave}}$ determination will translate by a factor of 5.

As already mentioned, we have used the DØ detector data (Run I) for total integrated luminosity 108.3 ± 5.7 pb^{-1}. The data is used after applying all the selection cuts as mentioned in Sec. 8.3. Finally, we are left with 3 $e\mu$ events. For this final set of 3 $e\mu$ events $\mathrm{M}_{e\mu}^{\mathrm{ave}} = 74.84$, which leads to the top quark mass $\mathrm{M}_{\mathrm{top}} = 158.35$ GeV.

[2]The *central value* describes the characteristics of the entire distribution which can be distribution's mean, median or mode.

Top Quark Mass M_{top} (GeV)	Central Value $M_{e\mu}^{ave}$ (GeV)	Stat. Error (GeV)
170	77.63	$\pm$ 0.42
175	78.84	$\pm$ 0.42
180	79.66	$\pm$ 0.41

Table 9.3: Statistical error corresponding to different top quark masses.

The same procedure has been applied by taking the subsamples of 3 events each for MC and it has been observed that the slope is again the same as given in Eqn. 9.12.

To see how this method will work at LHC energy (Large Hadron Collider) ($\sqrt{s}$ =14 TeV) for the top quark estimation, we have also studied the correlation between the $e\mu$ invariant mass and the generated top quark mass at the LHC energy for which we have generated $t\bar{t} \rightarrow WbWb \rightarrow (e/\mu)\ \nu\ \ (e/\mu)\ \nu$ samples for top quark masses ranging from 160 GeV to 180 GeV, in 0.4 GeV steps, for pp collisions at $\sqrt{s}$ = 14 TeV, using the PYTHIA (5.7) [36] event generator. 10K events at each mass were generated. To a large extent the method relies on the proper MC (PYTHIA) description of top production and decay. The $e\mu$ invariant mass $M_{e\mu}$has been determined taking different top masses from which their correlation w.r.t. each top quark mass has been studied. We observed that the mass measurement accuracy is dominated by the current understanding of theoretical uncertainties which results in a systematic error of $\lesssim$ 2 GeV [73]. The results based on the method of invariant mass for channels lJ/ψ and $l\mu$ in jet can be found in [74].

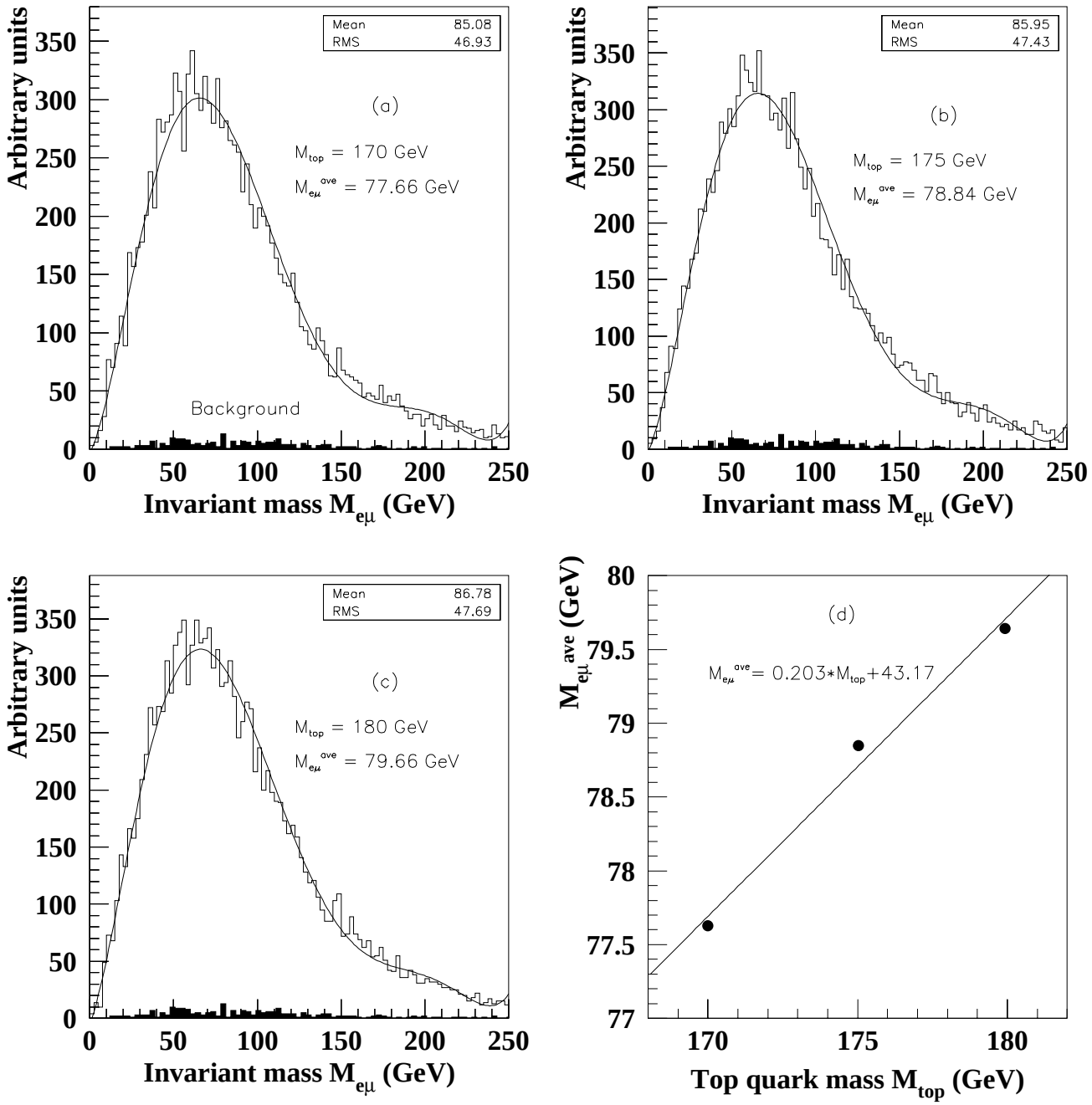

Figure 9.19: $e\mu$ Invariant mass spectra for different top masses.

Chapter 10

Conclusions

- We have carried out in a systematic way a study of the top quark mass using three different methods, namely, Neural Networks method, method of four vectors and the method of invariant mass, by using DØ data of Run I and attempt has been made to find the suitable method which can be used for Run II DØ data. So that one can make the optimum use of increase of statistics by reducing systematic errors also.

- In the case of NN analysis, the top quark mass comes out to be 177.9 GeV. The statistical uncertainty is $\sim$ 56 - 59 GeV (using Run I data) and the systematic error is 2.17 GeV. In case of four vectors method, the value of the top quark mass is 137.7 GeV. The statistical uncertainty for 3 $e\mu$ top events is $\sim$ 45 - 49 GeV which leads to a range of $\sim$ 77 - 85 GeV for a single unbaised measurement. Using the method of four vectors, the systematic error translates to 1.52 GeV. We see that this method gives us reasonable value of top quark mass within permissible range.

- When we simulate data in which events have been generated by assuming good muon *i.e.* muon is having as good resolution as that of electron and at the same center of mass energy, which will be the case for DØ Run II data.

  (i) For NN method, the statistical uncertainty is 40 - 42 GeV for the case of single measurement.

  (ii) For four vector method, statistical uncertainty comes out to be 41 - 49 GeV for a single measurement by using the same variables as used in NN nethod.

- We observe from the above a very interesting and important point that relatively a simple method of four vector analysis can be used for the top quark mass measurement for Run II data which gives comparable results with other methods by properly optimizing the different variables used.

- Using the third method of invariant mass, we have obtained the top quark mass to be 158.35 GeV with systematic error of $\sim$ 5 GeV in the measurement

of $e\mu$ invariant mass ($M_{e\mu}^{ave}$). The systematic uncertainty in the top quark mass would translate by the same amount.

- These methods will also be useful at LHC energy ($\sqrt{s} = 14$ TeV) where sufficient statistics will be available.

- R and D work was undertaken in the lab for the fabrication of Pixel Scintillation Counters. 5 counters were fabricated at Panjab University, Chandigarh and were tested with our DAQ system. The performance of counters was found to be extremely satisfactory.

Appendix A

Drawings

5 prototype Pixel Scintillation Counters were fabricated at Panjab University, Chandigarh. The total set of drawings was designed and developed in the department itself and got approved from Fermilab, USA before fabricating the counters. The mechanical fabrication work was done at the department as well as in the Central Tool Room, Ludhiana (CTRL).

Figures A.1 - A.14 show the drawings having the complete design of the fabricated counters.

Figure A.1: Design showing a pixel assembly counter.

Figure A.2: Drawing of a pixel scintillation counter showing special 8 grooves with dimensions (1mm wide $\times$ 6 mm wide).

Figure A.3: Bottom cover of pixel scintillation counter.

Figure A.4: Top cover of pixel scintillation counter.

Figure A.5: Design of aluminium channel used to provide support to pixel counters.

Figure A.6: Drawing of cookie cover.

Figure A.7: Design of cookie.

Figure A.8: Design of cookie embedded with 12 WLS fibers.

Figure A.9: Design of a coupling used for PMT.

Figure A.10: Design of a connector.

Figure A.11: Design of a clamp with diameter 42.0 mm.

Figure A.12: Design of a clamp with diameter 48.0 mm.

Figure A.13: Design of a rectangular spacer used to fix cookie cover on the top cover of pixel scintillation counter.

Figure A.14: Design of a cylindrical spacer.

Bibliography

[1] J. Ellis, Int. J. Mod. Phys. **A12**, 5531 (1997).
G. Altraelli, R. Barbieri and F. Caravaglios Int. J. Mod. Phys. **A13**, 1031 (1998).

[2] LEP Collaborations, *A Combination of Preliminary Electroweak Measurements and Constraints on the Standard Model, CERN-EP-2000-016, Geneva (2000).*

[3] DØ Collaboration, S. Abachi *et al.*, Phys. Rev. Lett. **74**, 2632 (1995).

[4] CDF Collaboration, F. Abe *et al.*, Phys. Rev. Lett. **74**, 2626 (1995).

[5] G. Kane, *Modern Elementary Particle Physics*, Addison Wesley Publishing Co., Reading, Massachusetts (1993).

[6] H. Arason *et al.*, Phys. Rev. **D46**, 3945 (1992).

[7] M. Sher, Phys. Lett. **B317**, 159 (1993).

[8] E. Laenen, J. Smith and W. van Neervan, Phys. Lett. B **321**, 254 (1994).

[9] G. Bordes and B. van Eijk, Nucl. Phys. **B435**, 23 (1995).

[10] P. Baringer and A. P. Heinsen, *Single Top Physics with a High Luminosity Tevatron*, DØ Note 2600.

[11] G. Kane, Top quark topics. In J. Hawthrone, editor, *Gauge Bosons and Heavy Quarks : Proceedings of the Eighteenth SLAC Summer Institute on Particle Physics, SLAC REPORT* **378**, 123 (1990).

[12] K. Tollefson, *Top Quark Production and Decay Measurements from CDF*, FERMILAB-CONF-98-389-E, Proceedings of the ICHEP 98, Vancouver (1998).

[13] K. Hagiwara *et al.*, Phys. Rev. D **66** (2002).

[14] J. H. Cochran, PhD thesis, *Search for the Truth in the $e\mu$ Channel*, SUNY at Stony Brook (1993).

[15] V. Bhatnagar, PhD thesis, *Search for the Top Quark in the $e\mu$ Channel*, Panjab University, Chandigarh (1998).

[16] J. Cochran, *eμ truth in Run 1*, DØ dilepton web page (1997), http://www-d0.fnal.gov/∼cochran/d0private/topemu.html

[17] L. Sonnenschein, *The $t\bar{t}$ Production in pp collisions at $\sqrt{s}$ =14 TeV*, PhD thesis, Physikelische Institute RWTH Aachen, Germany (2001).

[18] D. Bardin *et al.*, Z. Phys. **C44**, 493 (1989); Comp. Phys. Comm. **59**, 303 (1990); Nucl. Phys. **B351**, 1 (1991); Phys. Lett. **B255**, 290 (1991).

[19] F. Close, M. Martin and C. Sutton,*The Particle Explosion*, Oxford university Press, New york number 102 (1987) .

[20] R. Fernow, *Introduction to Experimental Particle Physics*, Cambridge University Press, Cambridge (1986).

[21] J. Thompson, *Introduction to Colliding Beams at Fermilab*, DØ Note 2367, FERMILAB-TM-1909, October (1994).

[22] L. M. Lederman, *The Tevatron*, Scientific American vol. 264, 53, March (1991).

[23] DØ Collaboration, S. Abachi *et al.*, Nucl. Inst. and Meth. in Phys Res., **A338**, 182 (1994).

[24] J. F. Detoeuf *et al.*, Nucl. Inst. and Meth. in Phys Res. **A265**, 157 (1988).

[25] C. Fabjan, Calorimetry in High Energy Physics, Thomas Ferbal, *Experimental Techniques in High Energy Physics.*

[26] C. Brown *et al.*, Nucl. Inst. and Meth. **A279**, 331 (1989).

[27] S. Abachi *et al.*, Nucl. Inst. and Meth. **A324**, 53 (1993).

[28] S. Snyder, *Measurement of the Top Quark Mass at DØ*, PhD thesis, State University of New York at Stony Brook, May (1995).

[29] Harpreet Singh, PhD thesis, *A Measurement of $t\bar{t}$ Production Cross Section in $p\bar{p}$ Collisions at $\sqrt{s} = 1.8TeV$ using Neural Networks*, University of California, Riverside (1999).

[30] V. Abramov *et al.*, *Technical Design Report for the DØ Forward Trigger Scintillation Counters*, DØ note 3237, November (1997).

[31] DØ Collaboration, *The DØ Upgrade*, Fermilab-FN-641, DØ note 2894, March (1996).

[32] B. S. Acharya, *Scintillation Counters for the DØ Muon Upgrade*, FERMILAB-PUB-97-226-E.

[33] W. R. Leo, *Techniques for Nuclear and Particle Physics Experiments*, 2nd Revised Edition, Springer-Verlog, New York.

[34] V. Bhatnagar *et al.*, *Fiber Studies for the Muon Scintillators*, DØ note 2421, October (1994).

[35] F. Paige and S. Protopopoescu, *Proceedings Summer Study on the Physics of SSC*, Snowmass Colorado (1986).

[36] PYTHIA v6.143, Sjöstrand, T. *Comp. Phys. Comm.* **82**, 74 (1994).

[37] G. Marchesini *et al.*, Comp. Phys. Comm. **67**, 465 (1992).

[38] R. Brun and F. Carminati, CERN program library long writeup, **W5013** (1993).

[39] T. Diehl and P. Quintas, *The MU-SMEAR package documentation*, (1994).

[40] DØ Collaboration, Phys. Rev. Lett. **75**, 1456 (1995).

[41] P. Bloom, PhD thesis, *Investigation of Trilinear Vector Boson Couplings through W boson Pair Production in Dilepton Decay Channels*, University of California, Davis (1998).

[42] SHW v2.0, J. Conway, available at http://www.physics.rutgers.edu/∼jconway/soft/shw/shw.html.

[43] PGS available at http://www.physics.rutgers.edu/∼jconway/soft/pgs/pgs.html.

[44] Saul Youssef, Comp. Phys. Comm. **45**, 423 (1987).

[45] Particle Data Group, Phys. Rev. **D50**, 1173 (1994). (URL:http://pdg.lbl.gov/)

[46] D. Chakraborty, *A search for* $t\bar{t} \to electron + \not\!\!E_T + jets$ *signature in* $p\bar{p}$ *collisions at* $\sqrt{s} = 1.8$ *TeV with the DØ Detector*, PhD thesis, State University of New York at Stony Brook, Stony Brook, New York (1994).

[47] DØ Collaboration, S. Abachi *et al.*, Phys. Rev. **D52**, 4877 (1995).

[48] G. Arnison *et al.* (UA1), Phys. Lett., **B123**, 115 (1983).

[49] G. Arnison *et al.* (UA1), Phys. Lett., **B132**, 214 (1983).

[50] R. Astur, *Correction of MET*, DØ note 2088 (1994).

[51] S. J. Wimpenny, *The TOP-LEPTONS* Analysis Package (version 6.01), DØ internal note 2144 (unpublished) (1994).

[52] R. Kehoe and R. Astur, DØ internal note 2052, 2908 (unpublished), (1994,96).

[53] Phsyics Analysis Workstation (PAW), *An Introductory Tutorial*, CERN Geneva, Switzerland.

[54] C. Peterson and T. Rognvaldsson, *An introduction to Artificial Neural Networks*, 1991 CERN school of computing (1991).

[55] Eunil Won, PhD thesis, *Top quark production in multijet final state*, University of Rochester (1996).

[56] Harpreet Singh *et al.*, *Top via $e\mu$ using neural nets (1992-93 data)*, DØ internal note 3071(unpublished) (1996).

[57] Suman B. Beri, Rajwant Kaur, Pushpalatha Bhat, Harrison B. Prosper, Top Quark Mass Measurements using Neural Networks, DØ note 3794 (2000).

[58] Suman B. Beri, Rajwant Kaur, Pushpalatha Bhat, Harrison B. Prosper, Top Quark Mass Measurements using Neural Networks, AIP Conference Proceedings, 583 (2001).

[59] J. Hertz, A. Krogh and R.G. Palmer, *Introduction to the Theory of Neural Computation*, Addison Wesley, Redword City, CA (1991).

[60] H. B. Prosper, *Some Mathematical Comments on Feed Forward Neural Networks*, DØ note 1606 (1993) (unpublished).

[61] CDF Collaboration, F. Abe *et al.*, Phys. Rev. Lett. **80**, 2779 (1998).

[62] DØ Collaboration, S. Abachi *et al.*, Phys. Rev. Lett. **80**, 2063 (1998).

[63] K. Kondo, J. Phys. Soc. Jpn. **57**, 4126 (1988).
ibid., J. Phys. Soc. Jpn. **60**, 836 (1991).
ibid., J. Phys. Soc. Jpn. **62**, 1177 (1993).

[64] R. H. Dalitz and G. R. Goldstein, Phys. Rev. D **45**, 1531 (1992).
ibid., Phys. Lett. B **287**, 225 (1992).

[65] H.B. Prosper, Phys. Lett. **B 335**, 515 (1994).

[66] CDF and DØ Collaborations, Demortier, L. *et al.*, "The Top Averaging Group", FERMILAB-TM-2084 (1999); P.C. Bhat, H. B. Prosper and S. S. Snyder, Int. J. Mod. Phys. A **13**, 5113 (1998).

[67] DØ Collaboration, S. Abachi, *et al.*, Phys. Rev. Lett. **80**, 2063 (1998); K. Kondo, J. Phys. Soc. Jpn. **60**, 836(1991); *ibid.,* J. Phys. Soc. Jpn. **62**, 1177 (1993); R. H. Dalitz, and G. R. Goldstein, Phys. Rev. D **45**, 1531(1992); *ibid.,* Phys. Lett. **B 287**, 225 (1992).

[68] CDF Collaboration, F. Abe, *et al.*, Phys. Rev. Lett. **80**, 2779 (1998).

[69] P. C. Bhat, H. B. Prosper and S. S. Snyder, Phys. Lett. B **407**, 73 (1997).

[70] E. W. Varnes, PhD thesis, *Measurement of the Top Quark Mass*, University of California, Berkeley (1997).

[71] P. C. Bhat *et al.*, *Bayesian Analysis of Multi-Source Data*, Phys. Lett. **B 407**, 73 (1997).

[72] Rajwant Kaur, Suman B Beri and J M Kohli, *Measuring the top quark mass in the $e\mu$ channel: A Study*, Pramana Journal of Physics, **57**, 4 (2001).

[73] Rajwant Kaur, Suman B. Beri and J. M. Kohli, *Top Mass Determination in the Dilepton ($t\bar{t} \to e\mu$) Channel at LHC: A Study*, CMS IN 018 (2001).

[74] A. Kharchilava, *Top Mass Determination in Leptonic Final States with* J/ψ, CMS NOTE 65 (1999).